

A Computational Study on the Aerobic Oxidation of Benzene to Phenol in Cu–Exchanged Y Zeolite

Von der Fakultät Chemie der Universität Stuttgart
zur Erlangung der Würde eines Doktors der
Naturwissenschaften (Dr. rer. nat.) genehmigte Abhandlung

Vorgelegt von
Shampa Santra
aus Hooghly, Indien

Hauptberichter : Prof. Dr. G. Rauhut, Universität Stuttgart
Mitberichter : Prof. Dr. H. Stoll, Universität Stuttgart

Tag der mündlichen Prüfung : 19. Februar 2010

Institut für Theoretische Chemie der Universität Stuttgart

2009

Mrs. Schrödinger to Mr. Schrödinger: "What the hell did you do to the cat? It looks half dead!"

- anonymous

Acknowledgements

I would like to express my gratitude to all those who gave me the possibility to complete this thesis. I want to thank the Institut für Theoretische Chemie, Universität Stuttgart for giving me permission to commence this thesis in the first instance, to do the necessary research work and to use departmental resources. I am deeply indebted to my supervisor Prof. Dr. G. Rauhut whose help, stimulating suggestions and encouragement helped me in all the time of research and writing of this thesis.

Besides my advisor, I would like to thank Prof. Dr. H. Stoll, Prof. Dr. E. Roduner for their encouragement, insightful comments, and hard questions.

I am particularly grateful to Prof. Dr. H.-J. Werner from whom I benefited considerably through various discussions and Prof. Dr. L. v. Szentpály for being so cheerful and providing a friendly and happy environment in the group.

I am thankful to Dr. R. Mata, an answering machine for any kind of technical questions. Special thanks are also due to Dr. M. Sierka for helping me to solve some technical problems.

I have furthermore to thank our secretary Mrs. I. Rosenkranz for being as nice as ever and for all kinds of help and Mrs. Ratna Ghosh for her help and support during my initial days in Stuttgart.

All of my colleagues present and former: Thomas, Aron, Sandra, Aygul, Sham, Yu, Xuebin, Gerald, Oliver, Werner, Detlev, Erich, Klaus, Christoph, Michael, Judith, Johannes, Stephan, Helena, Tanja, Augusta deserve hearty thanks for being helpful and friendly. I wish especially to thank my room mates present and former: Sandra and Thomas, Oliver for being nice to me, and also to those who helped me by proof-reading this thesis: Dr. J. Kästner and Prof. Dr. L. v. Szentpály.

Especially, I would like to give my warmest thanks to my husband Raghunathan and my parents whose love, support and encouragement enabled me to complete this work.

Abstract

In heterogeneous catalysis transition metal-containing zeolites, in particular copper-exchanged zeolites, have been studied experimentally [1, 2] as well as theoretically. Zeolites have large surface areas and different active sites (Brønsted acid sites and transition metal centers) which play a significant role in catalysis. In order to study the catalytic oxidation of benzene to phenol using dioxygen, the adsorption of dioxygen, benzene, and their co-adsorption to Cu-exchanged Y zeolite have been investigated by means of Fourier transform infrared (FTIR) spectroscopy [1, 2] and model calculations at the combined quantum mechanics and molecular mechanics (QM/MM) level using the QM-Pot program. The cost-effective QM/MM approach, which treats the active part of a system by QM methods, and the rest by a classical force field giving a reliable prediction of chemical properties has become an important tool for computational modeling of catalyzed reactions. In the QM/MM framework, the QM calculations have been performed using BP86 and B3LYP exchange-correlation functionals, employing triple-zeta quality basis sets and the MM calculations are done with a polarizable force field. High-level *ab initio* (CCSD(T), MRCISD+Q) [2] calculations have also been performed for a simple CuO_2^+ model system to give proofs that DFT correctly represents, and predicts the structural and electronic properties of CuO_2 moieties in the present study. The model Cu–Y zeolite structures have been determined with single Cu(I) centers. Adsorption complexes at two different sites (II and III) in Y zeolite with different Si/Al patterns have been studied.

On adsorption of O_2 to Cu-exchanged Y zeolite, end-on coordination to the Cu atom prevails at site II whereas site III shows side-on coordination. O_2 binds more strongly at site III than at site II and the triplet electronic states are the most low-lying energy states. But, small singlet-triplet splitting indicates that the impact of singlet states on the properties of adsorbed O_2 is an interesting aspect. The calculated harmonic frequency of dioxygen adsorbed at site III agrees well with the experimental IR result. In several adsorption complexes, the assignment of the O_2 stretching vibration was difficult due to its strong coupling with framework vibrations.

An η^2 -coordination of benzene to copper was observed for all adsorption complexes. Its interaction with Cu is stronger for site III than for site II, and the benzene–copper complexes show higher binding energies than those of dioxygen. A comparison between experimental IR results and theoretical harmonic vibrational frequencies is discussed for different benzene–copper adsorption complexes.

In case of the simultaneous adsorption of O₂ and C₆H₆, the main focus is at site III. Both O₂ and C₆H₆ are attached to the same Cu(I) center. O₂ changes its bonding pattern from side-on in single adsorption to end-on in co-adsorption processes, whereas C₆H₆ binds to Cu as η^2 as in the case of single adsorption.

A possible multistep reaction pathway is proposed for the aerobic oxidation of benzene to phenol in Cu–Y zeolite on the triplet, singlet and broken-symmetry singlet potential energy surfaces. The *oxygen-insertion* into the C–H bond of benzene occurs, and a σ -complex is formed. Simultaneous formation of the O–H bond and cleavage of the C–H bond result in a phenol-complex. Local electron correlation calculations were performed to deliver high-level estimates for the reaction barrier.

Contents

Acknowledgements	iv
Abstract	v
Citations to Published Work	xi
Abbreviations	xiii
Selected Symbols	xvii
1 Introduction	1
1.1 The Origins of Quantum Theory	1
1.2 Computational Chemistry	2
1.3 Motivation: The Oxidation of Benzene to Phenol	4
1.4 Overview of Thesis	6
2 Theoretical Background	9
2.1 Methods of Molecular Quantum Mechanics	9
2.1.1 The Born-Oppenheimer Approximation	9
2.1.2 Many-Electron Hamiltonian and Many-Electron Wave Function	11
2.1.3 The Hartree-Fock Approximation	12
2.1.4 Configuration Interaction	15
2.1.5 Møller-Plesset Perturbation Theory	17
2.1.6 The Coupled-Cluster Method	18
2.1.7 Multi-Configuration Self-Consistent Field (MCSCF)	19
2.1.8 Complete Active Space Self-Consistent Field (CASSCF)	20
2.1.9 Multi-Reference Configuration Interaction (MRCI)	20
2.1.10 Local Correlation Methods	21
2.1.11 Density Functional Theory	22
2.2 Classical Force Fields	25
2.2.1 Potential Form	26
2.2.2 GULP	26
2.3 Combined Quantum Mechanics and Molecular Mechanics Methods	28

2.3.1	QM-Pot	32
3	Zeolites	35
3.1	Structure and Functionality	35
3.1.1	Application	38
3.2	Catalysis	38
3.3	Faujasite Zeolite	39
3.3.1	Characterization Techniques for Zeolites	43
3.3.2	IR Spectroscopy of Y Zeolite	45
4	Benchmark Studies	49
4.1	Computational Details	49
4.2	Basis Set Effects	53
4.3	QM/MM Calculations vs. Molecular Fragment Calculations	54
4.4	Size of the Embedded Cluster	55
4.5	Verification of DFT Results by MRCI Calculations	59
5	Single Adsorption	63
5.1	Adsorption of Dioxygen	63
5.1.1	Local Structure of Bare Cu(I) Ion Sites	63
5.1.2	Cu(I) Binding Energies	65
5.1.3	Geometries	67
5.1.4	Charges	74
5.1.5	Energies	75
5.1.6	Comparison between Computed and Experimentally Obtained Vibrational Frequencies	78
5.1.6.1	Experimental Results	78
5.1.6.2	Theoretical Results	79
5.2	Adsorption of Benzene	83
5.2.1	Geometries	83
5.2.2	Charges	91
5.2.3	Energies	92
5.2.4	Frequencies	94
5.2.4.1	Computed Frequencies	95
5.2.4.2	Comparison with Related Systems	98
5.2.4.3	Splitting of Degenerate Modes	99
6	Simultaneous Adsorption of Dioxygen and Benzene	101
6.1	The Motivation	101
6.2	Geometries	102
6.2.1	Van der Waals Complexes at Sites II and III	102
6.2.2	Co-adsorption of O ₂ and C ₆ H ₆ at the Same Cu ⁺ Center	106
6.2.2.1	<i>Endo</i> -Complexes	107
6.2.2.2	<i>Exo</i> -Complexes	108
6.3	Energies	112

6.3.1	Energies of the <i>Endo</i> -Complexes	112
6.3.2	Energies of the <i>Exo</i> -Complexes	113
6.4	Frequencies	114
6.4.1	Frequencies of the <i>Endo</i> -Complexes	114
6.4.2	Frequencies of the <i>Exo</i> -Complexes	116
7	A Possible Mechanism for the Oxidation of Benzene to Phenol	119
7.1	QM/MM Partitioning	120
7.2	Optimization and Transition State Search	121
7.3	Reaction Mechanism	124
7.3.1	Reaction Intermediates and Transition States	125
7.3.2	Energetics of the Reaction Pathway	131
7.3.3	Single-Point <i>ab initio</i> Calculations	133
8	Summary	135
9	Zusammenfassung	139
A	Basis Set Studies on Various Model Complexes of Y Zeolites	143
B	QM-Pot Machinery	145
B.1	Convergence Criteria Used Throughout QM/MM Calculations	145
B.2	QM-Pot Optimizer	146
B.3	MM Parameters	147
C	Population Analyses	149
D	Cu(II)–Y Zeolite Modelling	155
	Bibliography	159

Citations to Published Work

Large portions of Chapter 4 and Chapter 5 have been published as

“Adsorption of dioxygen to copper in CuHY zeolite”,

S. Santra, T. Archipov, A. B. Ene, H. Komnik, H. Stoll, E. Roduner and G. Rauhut, *Phys. Chem. Chem. Phys.* **11**, 8855 (2009)

The second section of Chapter 5 is partly featured in

“Adsorption of benzene to copper in CuHY zeolite”,

T. Archipov, S. Santra, A. B. Ene, H. Stoll, G. Rauhut and E. Roduner, *J. Phys. Chem. C* **113**, 4107 (2009)

Large fractions of Chapter 6 and Chapter 7 will be published in the following papers:

“Simultaneous adsorption of benzene and dioxygen in CuHY zeolites as a precursor process to the aerobic oxidation of benzene to phenol”,

S. Santra, H. Stoll and G. Rauhut, *Phys. Chem. Chem. Phys.* *submitted*

“Towards the aerobic oxidation of benzene to phenol over Cu–exchanged Y zeolite: QM/MM study on the mechanistic pathway”,

S. Santra, H. Stoll and G. Rauhut, *manuscript in preparation*

Abbreviations

B3LYP	Becke 3 -Parameter (Exchange), Lee, Yang, Parr (Correlation)
BP 86	Becke 1988 exchange and Perdew 1986 correlation functionals
BS	Broken-Symmetry
CASSCF	Complete Active Space Self-Consistent Field
cc-pVDZ PP	correlation consistent polarized Valence Double Zeta Pseudopotential
cc-pVTZ PP	correlation consistent polarized Valence Triple Zeta Pseudopotential
CC	Coupled-Cluster
CCSD	Coupled-Cluster with Single and Double excitations
CCSD(T)	Coupled-Cluster with Single and Double and Perturbative Triple excitations
CI	Configuration Interaction
CIS	Configuration Interaction with Single excitation
CISD	Configuration Interaction with Single and Double excitations
CSF	Configuration State Function
DFT	Density Functional Theory
EPR	Electron Paramagnetic Resonance Spectroscopy
ECP	Effective Core Potential
EXAFS	Extended X-Ray Absorption Fine Structure
FTIR	Fourier Transform Infrared Spectroscopy
FCC	Fluid Catalytic Cracking
Fau	Faujasite
GGA	Generalized Gradient Approximation
GULP	General Utility Lattice Program
HF	Hartree-Fock
HOMO	Highest Occupied Molecular Orbital

IR-REMPD	I nfrared R esonance E nhanced M ulti- P hoton D issociation
IR	I nfrared Spectroscopy
IRC	I ntrinsic R eaction C oordinate calculation
IUPAC	I nternational U ion of P ure and A ppplied C hemistry
KS	K ohn- S ham
LCAO	L inear C ombination of A tomical O rbitals
LCCSD	L ocal C CS D
LDA	L ocal D ensity A pproximation
LJ	L ennard- J ones Potential
LMP2	L ocal M øller- P lesset perturbation theory of order 2
LUMO	L owest U noccupied M olecular O rbital
MCSCF	M ulti- C onfiguration S elf- C onsistent F ield
MM	M olecular M echanics
MO	M olecular O rbital
MP	M øller- P lesset
MRCI	M ulti R eference C onfiguration I nteraction
MRCISD+Q	M ulti- R eference C onfiguration I nteraction with S ingle, D ouble and D avidson estimate for Q uadruple excitations
NMR	N uclear M agnetic R esonance Spectroscopy
NNN	N ext N earest N eighbor
PP	P seudopotential
PES	P otential E nergy S urface
QM	Q uantum M echanics
QM/MM	Q uantum M echanics/ M olecular M echanics
QM-Pot	Q uantum M echanics interatomic P otential function
RHF	spin R estricted H artree- F ock
RKS	spin R estricted K ohn- S ham
SCF	S elf- C onsistent F ield
SD	S later D eterminant
SVP	S plit- V alence plus P olarization
S-T	S inglet- T riplet

TS	T ransition S tate
TZVP	T riple- Z eta V alence plus P olarization
UHF	spin U nrestricted H artree- F ock
UKS	spin U nrestricted K ohn- S ham
XAS	X - R ay A bsorption S pectroscopy
XRD	X - R ay D iffraction
XRPD	X - R ay P owder D iffraction
ZSM	Z eolite S ocony M obil

Selected Symbols

Φ	Exact many-electron wave function
Ψ	Approximate many-electron wave function
Ψ_0	Hartree-Fock ground state wave function
ψ	Spatial molecular orbitals
ϕ	Basis function
χ	Spin orbital
\hat{H}	Hamiltonian operator
$\hat{h}(1)$	One-electron Hamiltonian operator
C	MO coefficient
c	CI expansion coefficient
\hat{f}	Fock operator
E_b	Binding energy
E_{rel}	Relative energy
ν_{O-O}	Stretching vibration of O_2
ν_{13}	Stretching vibration of C–C ring in C_6H_6

Chapter 1

Introduction

1.1 The Origins of Quantum Theory

In the late seventeenth century, one of the first formulations of classical mechanics was postulated by Sir Isaac Newton:

$$\mathbf{F} = m\mathbf{a} \tag{1.1}$$

Toward the end of the 19th century, the concepts of “classical mechanics” - generally adopted by physicists were adequate to describe all physical phenomena known at that time, and classical mechanics was complemented by classical electrodynamics. As the knowledge of physical phenomena deepened on the microscopic scale¹ classical theory faced more and more difficulties and contradictions. It became apparent that the phenomena on the microscopic scale do not fit into the framework of classical mechanics and their explanations needed some sort of new principles. The fundamental underlying ideas of these new principles were uncovered in stages at the beginning of the 20th century.

The first step in this direction was to propose that certain physical variables assume only *quantized* or *discrete* values in contrast to the continuum values according to the axioms of classical physics. In order to explain the so-called “black-body² radiation”, in 1900,

¹ The “microscopic” scale is defined in the order of several *angstroms* ($1 \text{ \AA} = 10^{-8} \text{ cm}$) which is the length considered for atomic and subatomic particles. The “macroscopic” phenomena observable with naked eye or with ordinary microscope comes in the order of 1 micron (10^{-4} cm).

²A body which absorbs all the radiation it receives.

Max Planck postulated that the energy radiation does not take place in a continuous manner, rather it does in discrete amounts $h\nu, 2h\nu, 3h\nu, \dots$. Here, ν is the frequency of radiation, and h is the universal constant, known as *Planck's constant*. In 1905, Albert Einstein's hypothesis was a bold extension of Planck's theory of black-body radiation indicating that a light beam is a collection of "*photons*". In 1911, *Rutherford's model* of atom was solidly established: a central nucleus of small dimension (10^{-13} - 10^{-12} cm) is surrounded by a certain number of electrons Z . Almost all the mass of the atom is centered at the nucleus. The nucleus carries a positive electric charge Ze which is compensated by total $-Ze$ charges of electrons forming an electrically neutral entity, the atom. Shortly after that in 1913, *Bohr's circular-orbit model* stated that angular momenta of orbiting electrons around the nucleus are *discretized*. The second category of difficulties arose in applying the classical mechanics in the microscopic world concerning the distinction between *waves* and *particles*. In 1924 Louis-Victor de Broglie formulated the *wave-particle duality* of matter which was quite unacceptable in terms of purely classical concepts. By 1926, Heisenberg had developed *matrix mechanics* and Schrödinger's revolutionary postulate of *wave mechanics* governing the motion of nuclei and electrons in molecules started a new era of quantum mechanics.

1.2 Computational Chemistry

Molecules are made of atoms which in turn, consist of nuclei and electrons. Therefore if we want to understand fully the motions and behavior of molecules, we must be sure that we can quantitatively describe such properties of their constituents.

Computational chemistry is one of the expanding areas of current science. As the term says, it deals with computations that are used for understanding and predicting the behavior of chemical systems. It encompasses not only quantum mechanics, but also classical molecular mechanics, and involves simulations of molecular phenomena and prediction of new molecular properties. The methods of computational chemistry are useful to diverse fields of chemistry such as organic chemistry, inorganic chemistry, biochemistry, etc.. Improvements in computational techniques, both in hardware and software regime, various hierarchies of theories and models have made the availability of quite a number of user-friendly software packages thus keeping a large number of application-oriented research possible.

Although applications of computational chemistry have made their own mark in understanding the chemical processes at the atomic/molecular level, challenges still persist, when the size of the system increases. Nevertheless, equations and theories of quantum mechanics have been postulated and predicted to be consistent with the experimental findings, and on the other hand new theoretical approximations have been developed and tested by computational chemists. Sometimes theory can predict the measurement of new experimental data. If theory fails, it has to be refined, and thus this process continues unless a better theory has been developed. Theoretical chemists are dedicated to develop new theories and improve existing ones (new analytical equations, new computational tools, new mathematical models etc.). A theoretical chemist should also decide about the accuracy of the results needed for his/her purpose(s). Nevertheless, the accuracy that can be achieved in principle is limited by several fundamental approximations which are used in deriving the conventional quantum mechanical methodologies. Therefore, on one hand we see a hierarchy of quantum chemical methods (HF, MP2, CCSD, CCSD(T), CCSDT, . . . exact solution of the Schrödinger equation), and on the other hand we see an effort in the direction of linear scaling of computational cost with respect to the molecular size (see Fig. 1.1).

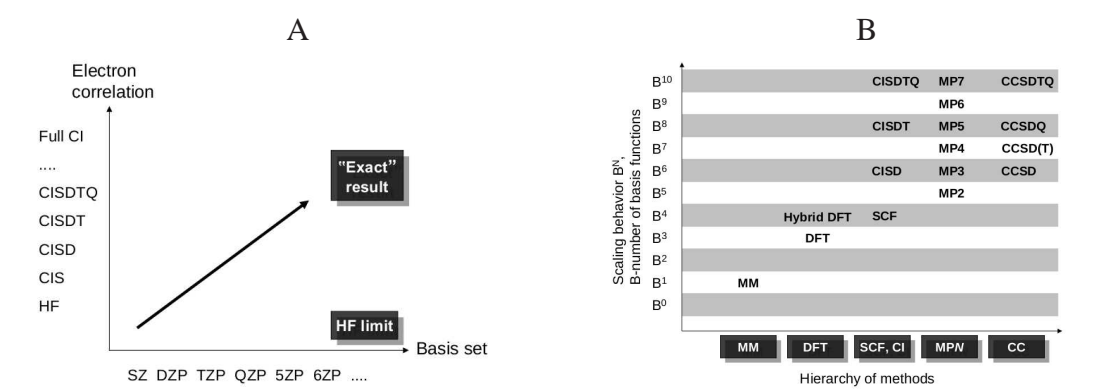


FIGURE 1.1: A. Convergence towards exact solution needs better description of both electron correlation (configuration interaction) and variational space (basis set), B. Computational cost of various theoretical methods [3].

We can only perform a calculation with chemical accuracy ($\pm 1 \text{ kcal mol}^{-1}$) of a system containing typically up to 10 atoms in the gas phase using the best theoretical method available. However, microporous materials such as zeolites, biological macromolecules (proteins, DNA, RNA) consist of several thousands of atoms. So, what can one do if one has to study such systems? One may think deeply, and one can find the scientifically possible/most probable solutions. (i) One has to make a compromise between accuracy

and computation time. One can use low-level theoretical methods and interpret the experimental results (if available). (ii) One can perform molecular mechanics calculations and preferably find out the most probable conformation and do as in (i).

The question arises whether one really needs to tackle the whole system to extract some molecular properties. Fortunately, several molecular properties are local in nature; such as adsorbate-adsorbent interactions, chemical reactions involving bond breaking and bond making. Therefore, to describe such properties, the whole system of interest can be divided into two parts: (i) the active part involving important chemical changes which can be treated at the high-level quantum mechanical (QM) methods, and (ii) the surrounding semi-rigid environment contributing negligible effects which can be treated at lower level molecular mechanical (MM) methods. This leads to a new concept, combined quantum mechanical/molecular mechanical (QM/MM) methods in theoretical computational chemistry. Thereby, reasonable accuracy is reached without increasing computational cost significantly.

1.3 Motivation: The Oxidation of Benzene to Phenol

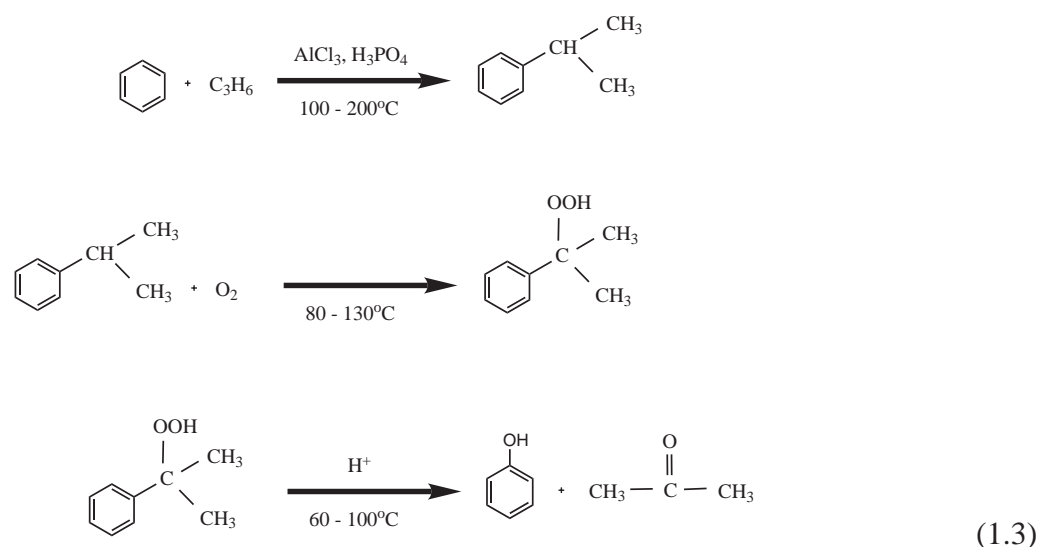
The aim of this thesis is to investigate the oxidation reaction of benzene with dioxygen as oxidant and Cu–Y zeolite as catalyst to form phenol as product.



Zeolites have often drawn extra attention in catalyzing various kinds of chemical reactions. Particularly Y zeolites have been studied significantly in that direction *e.g.* alkene isomerization [4], catalytic oxidation of CO, conversion of methanol to dimethyl carbonate [5–8], hydrocarbon cracking [9], etc..

Catalytic oxidation of benzene to phenol has been studied since the finding that this reaction can proceed in gas phase [10]. One of the most common processes for preparation of phenol at the industrial scale is the three-step cumene process: benzene alkylation to

cumene, cumene oxidation to cumene hydroperoxide, and decomposition of the latter to phenol and acetone:



Although, the cumene process was a great success for phenol production, it has certain disadvantages: an explosive intermediate, a multi-step character which makes it difficult to gain high selectivity. The most inevitable disadvantage is, the production of acetone as byproduct with 1:1 stoichiometry. At the industrial level the cumene process is financially less efficient because of the 1:1 yield of acetone which is of commercially low value. Therefore, during the past few decades, the search of new synthetic routes for phenol production is highly active. In this regard, one of the main concerns is to investigate the possibility of direct oxidation of benzene using oxygen donors. Hydrogen peroxide (H_2O_2) is one of the frequently used oxygen donors. H_2O_2 is known to be an excellent oxidant. By taking advantage of this property, promising work has been done using Ti-modified zeolites (TS-1) [11].

One of the major steps in the production of phenol from benzene is to couple a transition metal into the oxidation process. In 1983, Iwamoto and co-workers [10], proposed nitrous oxide (N_2O) as a better oxidant than dioxygen (O_2) which at the same time leads to the long awaited direct conversion of benzene to phenol. Since then, several groups of researchers have been working towards finding the best catalyst as well as oxidant for this reaction. Fe-ZSM-5 is found to be the most frequently used zeolite as a catalyst in combination with N_2O as oxidant. For a long time it has been a popular choice for the catalytic conversion of benzene to phenol. Panov [12] reported that N_2O is advantageous over O_2 for benzene oxidation in Fe-ZSM-5 zeolites, and N_2O is highly selective towards phenol production than O_2 . Iwamoto et al. [10] described that the

conversion of benzene to phenol takes place at 550°C using N₂O over vanadium oxide silica gel with 71% phenol selectivity. Panov et al. [13] proposed that presence of iron impurity plays an important role in the catalytic conversion of benzene to phenol forming an active species generated on Fe–ZSM-5 zeolite surface which is called α -oxygen. It is likely that this involves an iron-oxo species as a catalytic center. In order to furnish the structural information, and mechanistic pathways of the process, several spectroscopic studies [14, 15] as well as theoretical [16, 17] investigations have been performed.

Nevertheless, Tsuruya and co-workers reported gas-phase catalytic oxidation of benzene to phenol using molecular oxygen as oxidant in Cu–ZSM-5 zeolites [18–20]. In another study [21] this group had also reported about the liquid-phase catalytic oxidation of benzene over several Cu–zeolites (Cu/NaX, Cu/HX, Cu/NaY, Cu/HY, Cu/NaZSM-5, Cu/HZSM-5, Cu/NaMordenite, Cu/HMordenite, and Cu/Hbeta) using O₂ and ascorbic acid as oxidant and reducing agent, respectively. They demonstrated that among all the zeolite catalysts tested in their study, the Cu/HY zeolite showed the highest activity for phenol formation. Another group [22] has demonstrated that the Cu–ZSM-5 zeolites are promising catalysts for the oxidation of benzene to phenol using air even at moderate temperatures. The use of Cu to create the active phase in zeolite has significant advantages over alternative catalysts based on Fe. The latter needs the use of N₂O as an oxidant, which is toxic and one of the greenhouse gases causing global warming. For the safety and economic reasons, the use of O₂ is always provocative.

Therefore, the oxidation reaction of benzene using molecular oxygen in Cu–Y zeolite is explored in the present work. The results of this effort give an overview to understand the structures, and the energetics involved. The mechanism by which phenol is formed via the adsorption of both O₂ and C₆H₆ onto the Cu site in Y zeolite and the activated forms of the zeolite complexes (reactants, products, and transition states) are discussed.

1.4 Overview of Thesis

Theoretical methodologies used in applications of computational chemistry are discussed in Chapter 2. The first part of this chapter deals with the conventional wavefunction based *ab initio* quantum mechanical methods, then comes the density functional theory formalism, followed by classical mechanics. The main emphasis is on the combined quantum mechanical/molecular mechanical (QM/MM) methods.

Zeolites, the system of interest for the present thesis are reviewed in Chapter 3. The structural aspects, functionalities, the catalytic applicability, and the experimental techniques for their characterization are provided in detail.

Chapter 4 discusses the computational details which have been used in the present work. The system set-up, calibration calculations are presented here in a systematic way. All these prove the reliability of the chosen density functional that has been used.

The results of QM/MM calculations for zeolites are divided into three chapters 5, 6, & 7. Chapter 5 describes the “*lone*” adsorption of dioxygen, and benzene molecules in CuHY zeolite. Here, the theoretical results are supported by experimental FTIR (Fourier transform infrared spectroscopy) data. This chapter basically, establishes the adsorbate-adsorbent interaction which is the most important molecular aspect to be understood before moving into the chemical reaction between dioxygen and benzene in Cu-exchanged Y zeolite. The “*simultaneous*” adsorptions of both dioxygen and benzene in CuHY zeolite are presented in Chapter 6. Here, one type of adsorption complex is proposed to be the “*precursor complex*”. In Chapter 7, mechanistic pathways are suggested in the direction of phenol formation from aerobic oxidation of benzene in Cu–Y zeolite. Energy barriers are computed for the triplet, singlet and broken-symmetry singlet electronic states, and compared with the high-level *ab initio* local electron correlation calculations giving preliminary results.

Chapter 2

Theoretical Background

2.1 Methods of Molecular Quantum Mechanics

2.1.1 The Born-Oppenheimer Approximation

One of the central problems of quantum chemistry is to solve the nonrelativistic time-independent Schrödinger equation for molecular systems. In atomic units, the total Hamiltonian for a molecular system composed of M nuclei and N electrons is

$$\begin{aligned} \hat{H}_{\text{tot}} = & - \sum_{i=1}^N \frac{1}{2} \nabla_i^2 - \sum_{A=1}^M \frac{1}{2\tilde{M}_A} \nabla_A^2 - \sum_{i=1}^N \sum_{A=1}^M \frac{Z_A}{r_{iA}} \\ & + \sum_{i=1}^N \sum_{j>i}^N \frac{1}{r_{ij}} + \sum_{A=1}^M \sum_{B>A}^M \frac{Z_A Z_B}{R_{AB}} \end{aligned} \quad (2.1)$$

where \tilde{M}_A is the ratio of the mass of the nucleus A to the mass of an electron and Z_A is the atomic number of the nucleus A . The Schrödinger equation of the total system is given by

$$\hat{H}_{\text{tot}} \Psi_{\text{tot}}(\vec{r}, \vec{R}) = E_{\text{tot}} \Psi_{\text{tot}}(\vec{r}, \vec{R}). \quad (2.2)$$

The total wave function Ψ_{tot} depends on both electronic \vec{r} and nuclear \vec{R} coordinates. The whole molecular system is viewed as electrons interacting with the nuclei and with

each other via Coulomb's law to produce an effective field for the nuclei to move and the effective force between nuclei can be approximately described by Hooke's law. Thus, the two sets of particles, electrons and nuclei affect each other's motion. The first step towards uncoupling the electronic and nuclear motion is to consider Born and Oppenheimer's proof that if $1/\tilde{M}_A^{1/4} \ll 1$, the true molecular wave function can be adequately approximated as a product of the electronic wave function in the field of the fixed nuclei $\Psi_{\text{ele}}(\vec{r}; \{\vec{R}\})$ and nuclear wave function $\Psi_{\text{nuc}}(\vec{R})$:

$$\Psi_{\text{tot}}(\vec{r}, \vec{R}) \approx \Psi_{\text{ele}}(\vec{r}; \{\vec{R}\}) \Psi_{\text{nuc}}(\vec{R}). \quad (2.3)$$

The second step towards uncoupling the electronic and nuclear motion is to substitute Eq. 2.3 into Eq. 2.2. From the resulting equation, the terms involving the gradient of the electronic wave function w.r.t. the nuclear coordinates, *i.e.*, $\nabla_R \Psi_{\text{ele}}$ are neglected because the electronic wave function $\Psi_{\text{ele}}(\vec{r}; \{\vec{R}\})$ varies slowly w.r.t. the nuclear coordinates \vec{R} . The neglected term which couples the electronic and nuclear motion is written as the sum:

$$B = - \sum_{A=1}^M \frac{1}{2\tilde{M}_A} \left[\nabla_A^2 \Psi_{\text{ele}}(\vec{r}; \{\vec{R}\}) + \nabla_A \Psi_{\text{ele}}(\vec{r}; \{\vec{R}\}) \nabla_A \Psi_{\text{nuc}}(\vec{R}) \right]. \quad (2.4)$$

The term B in Eq. 2.4 constitutes a perturbation; if not negligible, it can cause transitions between the electronic levels [23, see p. 429].

Neglecting the coupling term completely, which is the most common approach to uncouple the electronic and nuclear motions, is called the Born-Oppenheimer approximation (separation). Eq. 2.2 can now be separated as two individual equations, the electronic and the nuclear Schrödinger equations. The rest of this chapter discusses the various levels of theoretical models used to solve the electronic Schrödinger equation,

$$\hat{H}_{\text{ele}} \Psi_{\text{ele}}(\vec{r}; \{\vec{R}\}) = E_{\text{ele}} \Psi_{\text{ele}}(\vec{r}; \{\vec{R}\}) \quad (2.5)$$

where the electronic Hamiltonian describes the motion of N electrons in the field of M point charges,

$$\hat{H}_{\text{ele}} = - \sum_{i=1}^N \frac{1}{2} \nabla_i^2 - \sum_{i=1}^N \sum_{A=1}^M \frac{Z_A}{r_{iA}} + \sum_{i=1}^N \sum_{j>i}^N \frac{1}{r_{ij}}. \quad (2.6)$$

The total energy for fixed nuclei must also include the constant nuclear-nuclear repulsion.

$$E_{\text{tot}} = E_{\text{ele}} + \sum_{A=1}^M \sum_{B>A}^M \frac{Z_A Z_B}{R_{AB}} \quad (2.7)$$

2.1.2 Many-Electron Hamiltonian and Many-Electron Wave Function

In the mean-field approximation, the total electronic Hamiltonian \hat{H}_{ele} is the sum of *effective* one-electron Hamiltonians $\hat{h}(i)$ which means that the total electronic wave function can be expressed as the product (Hartree product, Ψ_{HP}) of one-electron wave functions or spin orbitals $\chi_i(\vec{r}_i, \sigma_i) = \chi_i$ that are eigenfunctions of the one-electron Hamiltonians. The spin-orbitals can also be expressed as products of functions of spatial and spin coordinates $\chi_i(\vec{r}_i, \sigma_i) = \psi_i(\vec{r}_i)\omega(\sigma_i)$. In an LCAO framework where the spatial part of the spin orbitals are expanded as linear combination of K basis functions ϕ , one can form $2K$ spin orbitals

$$\hat{H}_{\text{ele}} = \sum_{i=1}^N \hat{h}(i) \quad \Rightarrow \quad \Psi_{\text{HP}} = \prod_{i=1}^N \chi_i. \quad (2.8)$$

Since the many-electron wave function should be anti-symmetric w.r.t. all the electrons, *i.e.*, it should change its sign under the simultaneous interchange of the spatial and spin coordinates of any pair of electrons, the product many-electron wave function (occupied orbitals) of, say, N electrons (Hartree product) should be antisymmetrized leading to a Slater determinant Ψ_{SD} :

$$\Psi_{\text{SD}} = \hat{A}\Psi_{\text{HP}} \Rightarrow \frac{1}{\sqrt{N!}} \begin{vmatrix} \chi_1(1) & \chi_2(1) & \chi_3(1) & \dots & \chi_N(1) \\ \chi_1(2) & \chi_2(2) & \chi_3(2) & \dots & \chi_N(2) \\ \vdots & \vdots & \vdots & & \vdots \\ \chi_1(N) & \chi_2(N) & \chi_3(N) & \dots & \chi_N(N) \end{vmatrix} = \hat{A} \prod_{i=1}^N \chi_i. \quad (2.9)$$

It should be noted that in the above equation only N occupied spin orbitals are involved. A more general many-electron wave function can be formed by taking a linear combination of Slater determinants

$$\Phi = \sum_i c_i \Psi_i. \quad (2.10)$$

When such a linear combination is made, a reference determinant is needed, usually the ground state Hartree-Fock (HF) wave function $|\Psi_0\rangle$ is considered as the reference determinant and the configuration represented by it is called the ground-state electronic configuration. Using $2K$ one-electron spin orbitals one can construct $\binom{2K}{N}$ different N -electron Slater determinants generated by exciting occupied MOs in the HF determinant to unoccupied MOs. Thus the set of possible determinants include a HF determinant $|\Psi_0\rangle$, and the singly excited determinants $|\Psi_i^a\rangle$, the doubly excited determinants $|\Psi_{ij}^{ab}\rangle$, etc. up to and including N -tuply excited determinants. With reference to the HF determinant, the others are referred to as *Singles (S)*, *Doubles (D)*, *Triples (T)*, *Quadruples (Q)*, etc..

The many electron Hamiltonian \hat{H}_{ele} typically has the form

$$\hat{H}_{\text{ele}} = \sum_i \hat{h}_i + \sum_i \sum_{j>i} \hat{v}_{ij} \quad (2.11)$$

where \hat{h}_i is an one-electron operator (core-Hamiltonian for electron i) involving coordinate and momentum operators of electron i and $\sum_{j>i} \hat{v}_{ij}$ is the two-electron operator involving coordinate operators of the electrons i and j . The proper expressions for the one and two-electron operators are the same as already given in Eq. 2.6 for a molecular system with N electrons and M nuclei:

$$\hat{h}_i = -\frac{1}{2} \nabla_i^2 - \sum_{A=1}^M \frac{Z_A}{r_{iA}} \quad \text{and} \quad \hat{v}_{ij} = \frac{1}{r_{ij}}. \quad (2.12)$$

2.1.3 The Hartree-Fock Approximation

In the Hartree-Fock (HF) approximation, the total electronic wave function is a Slater determinant (closed-shell case) Ψ_0 or a linear combination of few (open-shell and restricted open-shell cases) Slater determinants. The closed-shell energy of a molecular system of N electrons residing in $N/2$ different spatial orbitals is given by applying Slater-Condon rules [24, see p. 23-27]

$$E_0 = \langle \Psi_0 | \hat{H}_{\text{ele}} | \Psi_0 \rangle = \sum_i^{N/2} 2(i|\hat{h}|i) + \sum_{ij}^{N/2} [2(ii|jj) - (ij|ji)] \quad (2.13)$$

where one- and two-electron integrals are defined as

$$\langle i|\hat{h}|j\rangle = \int \psi_i^*(r_1)\hat{h}(r_1)\psi_j(r_1)dr_1 \quad (2.14)$$

$$\langle ij|kl\rangle = \int \psi_i^*(r_1)\psi_j(r_1)\frac{1}{r_{12}}\psi_k^*(r_2)\psi_l(r_2)dr_1dr_2. \quad (2.15)$$

To derive the Hartree-Fock eigenvalue equations one uses the general technique of functional variation, which says that the energy obtained using any test wave function will always be an upper bound to the exact energy of the system. The condition for an optimized HF wave function is to minimize E_0 w.r.t. orbital (*i.e.*, $\delta E_0 = 0$), subject to the orthonormality constraint. For this reason, one does not minimize the energy expression, instead the *Lagrangian function* \mathcal{L} is minimized

$$\mathcal{L} = \langle \Psi_0 | \hat{H}_{\text{ele}} | \Psi_0 \rangle - 2 \sum_{ij}^{N/2} \varepsilon_{ji} [\langle i|j \rangle - \delta_{ij}] \quad (2.16)$$

where ε_{ji} are the Lagrange multipliers and $\langle i|j \rangle$ is an overlap integral. The HF equations are obtained by setting the derivative of the Lagrangian w.r.t. each orbital to zero

$$\hat{f}|i \rangle = \sum_j^{N/2} \varepsilon_{ji}|j \rangle \quad (2.17)$$

where the *Fock operator* \hat{f} defined as

$$\hat{f}(i) = \hat{h}(i) + \sum_j \left[2\hat{J}_j(i) - \hat{K}_j(i) \right] = \hat{h}(i) + \hat{v}^{HF}(i). \quad (2.18)$$

The two operators $\hat{J}_j(i)$ and $\hat{K}_j(i)$, referred to as *Coulomb* and *exchange* operators, respectively, are defined by their effect while operating on a spatial orbital

$$\hat{J}_j(1)\psi_i(r_1) = \int \psi_j^*(r_2)\frac{1}{r_{12}}\psi_j(r_2)\psi_i(r_1)dr_2, \quad (2.19)$$

$$\hat{K}_j(1)\psi_i(r_1) = \int \psi_j^*(r_2)\frac{1}{r_{12}}\psi_i(r_2)\psi_j(r_1)dr_2. \quad (2.20)$$

In the HF approximation the electron-electron interaction operator r_{ij}^{-1} is replaced by a *average* field in the form of operator $\hat{v}^{HF}(i)$, seen by the i th electron due to the presence of other electrons.

Since the energy is invariant w.r.t. unitary transformations among the occupied orbitals, a simpler form for Eq. (2.17) is possible by using a basis where the Fock operator is diagonal, the canonical HF equations

$$\hat{f}|i\rangle = \varepsilon_i|i\rangle. \quad (2.21)$$

Such a basis is referred to as a canonical orbital basis. The diagonal elements of the Fock matrix are called, the orbital energies ε_i . Notice that the HF total energy is not equal to the sum of the occupied orbital energies. This would lead to double-counting of the electron-electron interaction.

So far the theory has been derived without knowing anything about the form of the spatial orbitals $\{\psi_i\}$. To calculate the electronic total energy variationally the most common technique employed is to expand the spatial orbitals as a linear combination of known (fixed) set of functions, usually a fixed linear combination of Gaussian-type functions $\{\phi_\mu\}$

$$\psi_i = \sum_{\mu=1}^K C_{\mu i} \phi_\mu. \quad (2.22)$$

Introducing Eq. 2.22 into Eq. 2.13 and deriving the expression for the total electronic energy is a standard exercise in basis transformation [25, See p.149-150] and in the atomic orbital representation Eq. 2.13 is written as

$$E_0 = \frac{1}{2} \sum_{\mu} \sum_{\nu} P_{\nu\mu} (H_{\mu\nu}^{\text{core}} + F_{\mu\nu}). \quad (2.23)$$

The terms $H_{\mu\nu}^{\text{core}}$ and $F_{\mu\nu}$ in the above equation are the matrix elements of the core Hamiltonian and Fock matrices respectively and the integrals involved in the expressions of these matrix elements are analytically derivable. The term $P_{\nu\mu}$ is the element of the so called density matrix or the charge-density bond-order matrix which for a closed-shell N electron system is defined as

$$P_{\nu\mu} = 2 \sum_{i=1}^{N/2} C_{\nu i} C_{\mu i}^*. \quad (2.24)$$

In the spin-restricted Hartree-Fock (RHF) approximation, the total electronic wave function is the Slater determinant defined for one particular electronic configuration and the total electronic energy is characteristic of that particular configuration alone. For an N -electron system, only the occupied $N/2$ spatial orbitals are explicitly involved in the total energy expression. The remaining $(K - N/2)$ spatial orbitals (virtual orbitals) are not important in the sense of total energy calculation but they are important in describing the MO energies. The Hartree-Fock approximation which is a simple many-body method acts as a starting point for further high-level schemes. In fact the correlation energy (E_{corr}), which is missing in the Hartree-Fock approximation, is defined as the difference between the exact non-relativistic total energy (\mathcal{E}_0) and the Hartree-Fock energy (E_0) in the limit that the basis set approaches completeness

$$E_{\text{corr}} = \mathcal{E}_0 - E_0. \quad (2.25)$$

2.1.4 Configuration Interaction

The Configuration Interaction (CI) method is a general many-body method where the electronic wave function is a linear combination of Slater determinants. The total electronic energy in such a scheme will not only involve weighted contributions due to different configurations but also the contributions due to interactions between various configurations.

$$\Phi_{\text{CI}} = c_0\Psi_0 + \sum_S c_S\Psi_S + \sum_D c_D\Psi_D + \sum_T c_T\Psi_T + \dots \quad (2.26)$$

The CI coefficients are determined by the *variational principle*. The electronic energy E , which is the variationally minimized quantity is calculated as the lowest eigenvalue of the CI *Hamiltonian matrix* H , whose elements are the following integrals:

$$H_{ij} = \langle \Psi_i | \hat{H} | \Psi_j \rangle \quad (2.27)$$

The linear variation problem can be expressed as a set of CI *secular equations*:

$$\begin{pmatrix} H_{00} - E & H_{01} & \dots & H_{0j} & \dots \\ H_{10} & H_{11} - E & \dots & H_{1j} & \dots \\ \vdots & \vdots & \ddots & \vdots & \dots \\ H_{j0} & \vdots & \dots & H_{jj} - E & \dots \\ \vdots & \vdots & \dots & \vdots & \dots \end{pmatrix} \begin{pmatrix} c_0 \\ c_1 \\ \vdots \\ c_j \\ \vdots \end{pmatrix} = \begin{pmatrix} 0 \\ 0 \\ \vdots \\ 0 \\ \vdots \end{pmatrix} \quad (2.28)$$

Some of the key features of the structure of the CI matrix are:

- Slater-Condon rule: Two Slater determinants will interact only if they differ by at most two occupied molecular orbitals, *e.g.* $S \leftrightarrow S$, $S \leftrightarrow D$, $S \leftrightarrow T$; otherwise

$$\langle \Psi_i | \hat{H} | \Psi_j \rangle = 0. \quad (2.29)$$

- Brillouin's theorem: The singly substituted determinant $|\Psi_S\rangle$ will not interact with the HF ground state determinant $|\Psi_0\rangle$.

$$\langle \Psi_0 | \hat{H} | \Psi_S \rangle = 0 \quad (2.30)$$

$$\begin{array}{l} \langle \Psi_0 | \\ \langle S | \\ \langle D | \\ \langle T | \\ \langle Q | \\ \vdots \end{array} \left[\begin{array}{cccccc} |\Psi_0\rangle & |S\rangle & |D\rangle & |T\rangle & |Q\rangle & \dots \\ \langle \Psi_0 | \hat{H} | \Psi_0 \rangle & 0 & \langle \Psi_0 | \hat{H} | D \rangle & 0 & 0 & \dots \\ & \langle S | \hat{H} | S \rangle & \langle S | \hat{H} | D \rangle & \langle S | \hat{H} | T \rangle & 0 & \dots \\ & & \langle D | \hat{H} | D \rangle & \langle D | \hat{H} | T \rangle & \langle D | \hat{H} | Q \rangle & \dots \\ & & & \langle T | \hat{H} | T \rangle & \langle T | \hat{H} | Q \rangle & \dots \\ & & & & \langle Q | \hat{H} | Q \rangle & \dots \\ & & & & & \dots \end{array} \right]$$

- Only blocks on the diagonal or up to two positions from the diagonal do not vanish.
- Usually, one limits the expansion to a certain order of substitution \Rightarrow truncated CI.
 - For the ground state, CIS (CI singles) is not meaningful because of Brillouin's theorem.
 - In a CISD calculation (CI singles and doubles), singles couple to the ground state indirectly via doubles.
- The size of the full CI matrix becomes extremely large if all possible excitations are included. Therefore, one has to truncate the excitation level. But then one ends up with the size-consistency problem.

2.1.5 Møller-Plesset Perturbation Theory

In Møller-Plesset (MP) perturbation theory, an energy correction due to electronic correlation, is introduced through a perturbation scheme. The Hartree-Fock ground state wave function Ψ_0 acts as the reference unperturbed wave function with the corresponding unperturbed Hamiltonian as the sum of Fock operators \hat{f}_i . The zero-order MP electronic energy is the sum of energies of occupied orbitals

$$E_0^{(0)} = \left\langle \Psi_0 \left| \sum_i \hat{f}_i \right| \Psi_0 \right\rangle = 2 \sum_{i=1}^{N/2} \langle \psi_i(1) | \hat{f}_i | \psi_i(1) \rangle. \quad (2.31)$$

The perturbation correction to the zero-order unperturbed Hamiltonian is the difference between the true molecular electronic Hamiltonian \hat{H}_{ele} (Eq. 2.6) and the zero-order Hamiltonian $\hat{H}_0 = \sum_i \hat{f}_i$

$$\hat{H}' = \hat{H}_{\text{ele}} - \hat{H}_0. \quad (2.32)$$

The first-order correction $E_0^{(1)}$ over the ground state wave function is given by

$$E_0^{(1)} = \left\langle \Psi_0 \left| \hat{H}' \right| \Psi_0 \right\rangle. \quad (2.33)$$

Thus the first-order MP electronic total energy is the Hartree-Fock electronic energy:

$$E_{\text{HF}} = E_0^{(0)} + E_0^{(1)}. \quad (2.34)$$

The Hartree-Fock energy is improved by a second-order energy correction $E_0^{(2)}$, for a closed-shell case it is given as

$$E_0^{(2)} = \sum_{i \neq 0} \frac{\left| \left\langle \Psi_i^a \left| \hat{H}' \right| \Psi_0 \right\rangle \right|^2}{E_0^{(0)} - E_i^{(0)}}. \quad (2.35)$$

In the above equation, the index i runs over all possible Slater determinants other than the one which corresponds to the ground state Hartree-Fock wave function. For a singly substituted Slater determinant Ψ_i^a , the integral $\left\langle \Psi_i^a \left| \hat{H}' \right| \Psi_0 \right\rangle$ vanishes according to Brillouin's theorem and the first-order correction to the ground state Hartree-Fock wave

function are doubly substituted determinants Ψ_{ij}^{ab} . The eigenvalue of the doubly substituted wave function differs from the ground state energy by replacing the orbital energies suitably. Thus the denominator in Eq. 2.35 will be $E_0^{(0)} - E_i^{(0)} = \varepsilon_i + \varepsilon_j - \varepsilon_a - \varepsilon_b$. The second-order energy correction $E_0^{(2)}$ can be analytically derived by substituting the expression for the correction Hamiltonian, Eq. 2.32 and by using Slater-Condon rules as

$$E_0^{(2)} = \sum_{a<b}^{\text{vir}} \sum_{i<j}^{\text{occ}} \frac{|\langle ab|ij\rangle - \langle ab|ji\rangle|^2}{\varepsilon_i + \varepsilon_j - \varepsilon_a - \varepsilon_b}. \quad (2.36)$$

The second-order MP electronic total energy can now be taken as:

$$E_{\text{ele}} = E_{\text{HF}} + E_0^{(2)}. \quad (2.37)$$

The Møller-Plesset perturbation theory of second-order (MP2) scheme is computationally efficient and provides an improvement over Hartree-Fock results for molecular properties and it is one of the commonly used methods for including correlation effects on molecular ground state equilibrium properties.

2.1.6 The Coupled-Cluster Method

The Coupled-Cluster (CC) method is one of the sophisticated *ab initio* methods. The ansatz for the CC wave function is

$$\Phi = e^{\hat{T}} \Psi_0. \quad (2.38)$$

The operator \hat{T} is the cluster operator which can be expanded as

$$\hat{T} = \sum_{i=1}^N \hat{T}_i \quad (2.39)$$

where \hat{T}_n is the n -particle excitation operator. The n -particle excitation operator is defined using the substituted Slater determinants as

$$\hat{T}_1 \Psi_0 = \sum_a \sum_i t_i^a \Psi_i^a, \quad \hat{T}_2 \Psi_0 = \sum_{a<b}^{\text{vir}} \sum_{i<j}^{\text{occ}} t_{ij}^{ab} \Psi_{ij}^{ab} \quad \text{etc.}, \quad (2.40)$$

where t_x^y are numerical coefficients, which in an actual calculation are obtained as the net result of solving a set of nonlinear equations with t_x^y as unknowns. The Schrödinger equation to be solved is

$$\hat{H}_{\text{ele}} e^{\hat{T}} \Psi_0 = E e^{\hat{T}} \Psi_0. \quad (2.41)$$

When $\hat{T} = 0$ the problem is simplified as an Hartree-Fock approximation and when only the first three terms are considered in Eq. 2.39, one arrives at the coupled-cluster singles, doubles and triples (CCSDT) method, $\hat{T} = \hat{T}_1 + \hat{T}_2 + \hat{T}_3$.

Thus the eigenvalue E in Eq. 2.41 can be expressed as sum of Hartree-Fock electronic energy E_{HF} and correction terms. An approximation to the CCSDT method is the CCSD(T) method where the energy contribution due to the triples \hat{T}_3 is calculated as a perturbative correction to the full CCSD energy. The CC methods converge relatively quickly in comparison to the full CI results due to the inclusion of the higher-order excitations. The CC methods are size-consistent but not variational. For properties such as dissociation and fragmentation energies, coupled-cluster theory used in conjunction with large basis sets is often expected to provide *chemical accuracy*, *i.e.*, ± 1 kcal/mol. The main drawback of the scheme is that it is computationally demanding. For example the limiting scaling of a CCSD(T) calculation is $O(N^7)$.

2.1.7 Multi-Configuration Self-Consistent Field (MCSCF)

“Single-reference” methods which include correlation through truncated CI or CC expansions often fail when faced with situations where two or more states approach degeneracy. Such problems occur in chemical systems, such as those containing transition metals, and in bond-breaking processes. *Static* or *Non-dynamic correlation* is connected to the existence of low-lying electronic states which is accounted for by the multi-configurational self-consistent field (MCSCF) method. The MCSCF wave function is a truncated CI expansion

$$\Phi_{\text{MCSCF}} = \sum_I c_I \Psi_I \quad (2.42)$$

where $\{\Psi_I\}$ is a set of orthonormal *Configurational State Functions* (CSFs). A CSF is a spin-symmetrized and space-symmetrized linear combination of Slater determinants.

In MCSCF method, both the CI-coefficients (c_I) and the coefficients of MOs are optimized. That is, the energy is minimized with respect to both c_I (as in the CI method), and orbital coefficients ($C_{\mu i}$). This orbital optimization is done iteratively in an analogous way to the SCF method, hence the name *multi-configuration self consistent field* (MCSCF) is given to this approach. For each set of CI-coefficients c_I , LCAO coefficients $C_{\mu i}$ are solved, then for this given set of $C_{\mu i}$ CI equations are solved for new c_I , and this iterative procedure is continued until self-consistency is achieved.

The MCSCF method should give a qualitatively correct description of the electronic structure provided all the necessary configurations are included in the set Ψ_I which is the major problem within MCSCF methods. One has to select configurations which are necessary for the property of interest, and those are included for the construction of the MCSCF wave function. Often size-consistency problems may arise in the selection of CSFs.

2.1.8 Complete Active Space Self-Consistent Field (CASSCF)

Here, the whole MO space is partitioned into *active* and *inactive* spaces. The active space is defined usually around the highest occupied molecular orbital (HOMO) and lowest unoccupied MO (LUMO) from an RHF calculation. The inactive space contains MOs which are either doubly occupied or empty. A full CI calculation is performed within the active space. Often the selection of an active space is rather difficult, and done manually by considering the problem of interest. If the chosen active space coincides with the true valence space, then CASSCF wave function can correctly describe all the dissociation pathways. The common notation [n,m]-CASSCF describes the distribution of n electrons in all possible ways into m orbitals. The factorial increase in the number of the CSFs limits the expansion of active space to 10-12 electrons/orbitals. CASSCF is size-consistent.

2.1.9 Multi-Reference Configuration Interaction (MRCI)

The CASSCF method focuses on a few active electrons in active orbitals chosen to give multiple configurations describing the required electronic state. For reliable energy differences between excited states, one must go beyond the CASSCF level and include *dynamic correlation* between the active and inactive electrons. There are three

approaches to include dynamic correlation based on the CASSCF method, similar to the single-reference methods based on the HF method: Multi-Reference (MR) Configuration Interaction (CI), coupled-cluster (CC) methods, and perturbation theory (PT). The most popular of the three above mentioned methods is the Multi-Reference Configuration Interaction (MRCI) method. In the MRCI scheme, an MCSCF wave function is used as the starting point. This method is very useful in constructing potential energy surfaces of small molecules.

2.1.10 Local Correlation Methods

Conventional electron correlation methods employ a basis of canonical molecular orbitals which are generally delocalized over the whole system. However local electron correlation methods can make use of the locality of the correlation hole. A localized description of the electron correlation has been used for a long time. The construction of the local molecular orbital basis and configuration spaces follows one of the most successful and convincing approaches proposed by Pulay and Saebø [26]. The procedure consists of the following details.

- Localized molecular orbitals (LMOs) are represented by linear combination of N basis functions ϕ_μ .

$$\begin{aligned} |\psi_i^{\text{LMO}}\rangle &= \sum_{\mu} |\phi_{\mu}\rangle L_{\mu i} \\ &= \sum_k |\psi_i^{\text{can}}\rangle U_{ki} \end{aligned} \quad (2.43)$$

LMOs are related to the canonical orbitals by means of an unitary transformation U . The transformation can be done using Pipek and Mezey localization algorithm [27] which minimizes the number of atoms at which the orbitals are located.

- The virtual orbitals are obtained by projecting out the occupied space from the AOs and are called projected atomic orbitals (PAOs) $\{\tilde{\phi}_r\}$

$$|\tilde{\phi}_r\rangle = \left(1 - \sum_i |\psi_i^{\text{LMO}}\rangle \langle \psi_i^{\text{LMO}}| \right) |\phi_r\rangle = \sum_{\mu} |\phi_{\mu}\rangle P_{\mu r}. \quad (2.44)$$

The projection matrix P is computed as

$$P = \mathbf{1} - LL^{\dagger}S. \quad (2.45)$$

- The occupied orbitals are orthogonal to each other.
- The PAOs are orthogonal to all occupied orbitals, but mutually non-orthogonal.

There are two sources of significant savings of CPU time in local correlation methods employing the following two approximations.

1. **Domain approximation:** To describe the electron correlation, the virtual space can be restricted for a given electron pair to a smaller subset (*domain*) of the atomic orbitals (AOs). The correlation space for a $|\psi_i^{\text{LMO}}\rangle$ should include the AOs located in the spatial vicinity of the MO.
2. **Pair approximation:** In the localized description, the pair correlation between the distant orbitals is very small. Therefore depending on the problem in hand, those *distant pairs* can be neglected or treated at the lower level of theory.

2.1.11 Density Functional Theory

Density Functional Theory (DFT) does not aim at calculating the electron ground state wave function, but to determine the three dimensional ground-state electron density $\rho(\vec{r})$. The theoretical foundation for this approach is the first Hohenberg-Kohn theorem which states that two N -electron systems with different external potentials can not have the same density $\rho(\vec{r})$. The electronic ground state density $\rho(\vec{r})$ yields the external potential up to a constant, and thus determines the entire Hamiltonian of the many-electron Schrödinger equation. DFT in principle provides an exact solution of the many-electron problem.

The total electronic energy of the system and all its contributions are functionals of the ground-state electron density $E[\rho(\vec{r})]$. Unfortunately, no explicit expression for the total electronic energy in the functional form is known and it can only be formulated by approximate analytic expressions. The second Hohenberg-Kohn theorem provides a variational principle w.r.t. the density. Variation of the total energy $E[\tilde{\rho}(\vec{r})]$ w.r.t. a positive definite trial density $\tilde{\rho}(\vec{r})$ that integrates to the correct total number of electrons yields the ground state density $\rho(\vec{r})$ at the energy minimum.

The implementation of DFT is almost exclusively done on the basis of the Kohn-Sham (KS) approach. In this scheme, the ground state of the non-interacting Hamiltonian

is introduced as a model system which is required to exhibit the same ground-state electron density as the true system. The model system is described by a wave function in the form of a Slater determinant. The density is expressed as the sum over the squares of the occupied one-electron orbitals, ψ_i

$$\rho(\vec{r}) = \sum_i^{\text{occ}} \psi_i^* \psi_i. \quad (2.46)$$

In the KS formulation, the DFT expression for the total energy is written as the sum of non-interacting electronic kinetic energy $E_{\text{KS,kin}}[\rho(\vec{r})]$, the potential energy $E_{\text{Ext}}[\rho(\vec{r})]$ of all the electrons in the external potential of the nuclei, the Coloumb interaction energy $E_{\text{Coul}}[\rho(\vec{r})]$ and the non-classical term, the exchange and correlation interaction energy $E_{\text{XC}}[\rho(\vec{r})]$:

$$E[\rho(\vec{r})] = E_{\text{KS,kin}}[\rho(\vec{r})] + E_{\text{Ext}}[\rho(\vec{r})] + E_{\text{Coul}}[\rho(\vec{r})] + E_{\text{XC}}[\rho(\vec{r})]. \quad (2.47)$$

While the first three terms on the r.h.s. of Eq. 2.47 are identical to the corresponding terms involved in the Hartree-Fock scheme, the exact form of the last term $E_{\text{XC}}[\rho(\vec{r})]$ is not known, and it can only be defined as the sum of all non-classical contributions to the electron-electron interaction and the difference between the true kinetic energy and the non-interacting kinetic energy:

$$E_{\text{XC}}[\rho(\vec{r})] \equiv E_{\text{ee}}[\rho(\vec{r})] - E_{\text{Coul}}[\rho(\vec{r})] + E_{\text{True,kin}}[\rho(\vec{r})] - E_{\text{KS,kin}}[\rho(\vec{r})]. \quad (2.48)$$

To solve the Schrödinger equation as a linear variational problem, one derives the single-particle KS equation:

$$\hat{h}_{\text{KS}}\psi_i = \varepsilon_i\psi_i \quad (2.49)$$

with the one-electron KS operator

$$\hat{h}_{\text{KS}} \equiv \hat{h}_{\text{Kin}} + \hat{h}_{\text{Ext}} + \hat{h}_{\text{Coul}} + \hat{h}_{\text{XC}} \quad (2.50)$$

In the above equation, the exchange-correlation contribution is obtained as the derivative of exchange-correlation energy functional w.r.t. $\rho(\vec{r})$. Different levels of approximations within the DFT framework differ solely in their approximations to the exchange-correlation term $E_{\text{XC}}[\rho(\vec{r})]$. Approximate expressions for the exchange-correlation

term which depends only on ρ are collectively called *Local Density Approximation* (LDA). The LDA exchange and correlation energy is defined as

$$E_{\text{XC}}^{\text{LDA}}[\rho(\vec{r})] \equiv \int d\vec{r} \rho(\vec{r}) \mu_{\text{XC}}[\rho(\vec{r})] \quad (2.51)$$

where $\mu_{\text{XC}}[\rho(\vec{r})]$ is the exchange-correlation energy per electron of the uniform electron gas. In more sophisticated approximations, formulated as Generalized Gradient Approximations (GGA), the exchange-correlation functional depends not only on the density ρ , but also on its gradient $\nabla\rho$, such functionals give a substantial improvement over LDA.

$$E_{\text{XC}}^{\text{GGA}}[\rho(\vec{r})] \equiv \int d\vec{r} f(\rho(\vec{r}), \nabla\rho(\vec{r})) \quad (2.52)$$

$E_{\text{XC}}^{\text{GGA}}$ is usually split into exchange and correlation parts, which are modeled separately:

$$E_{\text{XC}}^{\text{GGA}} = E_{\text{X}}^{\text{GGA}} + E_{\text{C}}^{\text{GGA}} \quad (2.53)$$

One of the commonly used gradient-corrected exchange-correlation energy functionals is BP86 [28–32] which includes B88 and P86 as the gradient-corrected exchange and correlation functionals, respectively.

$$E_{\text{XC}}^{\text{BP86}} = E_{\text{X}}^{\text{S}} + \Delta E_{\text{X}}^{\text{B88}} + E_{\text{C}}^{\text{VWN(V)}} + \Delta E_{\text{C}}^{\text{P86}} \quad (2.54)$$

Even better approximations exist in the hierarchy. One such group of functionals is called hybrid-XC functionals, where a fraction of exact exchange energy as derived in Hartree-Fock scheme is included. A popular and successful hybrid functional goes under the name B3LYP where the 3 indicates that the functional depends on three-parameters:

$$E_{\text{XC}}^{\text{B3LYP}} = (1-a_0)E_{\text{X}}^{\text{LSDA}} + a_0E_{\text{X}}^{\text{HF}} + a_{\text{X}}\Delta E_{\text{X}}^{\text{B88}} + a_{\text{C}}E_{\text{C}}^{\text{LYP}} + (1-a_{\text{C}})E_{\text{C}}^{\text{VWN}}. \quad (2.55)$$

In the above expression [33], the parameter values $a_0 = 0.20$, $a_{\text{X}} = 0.72$ and $a_{\text{C}} = 0.81$ were chosen to give good fits to experimental molecular atomization energies.

In Kohn-Sham DFT, the local exchange-correlation potential operator has a complicated analytic form and usually the integration of the matrix elements of this potential is performed by numerical integration based on grids. Evaluation of the exchange-correlation contribution to the total energy density functional is done by summing the contributions over grid points. The computational effort required for evaluation of the exchange-correlation contributions strongly depends on the selected grid size, *i.e.*, the number of integration points per atom.

A DFT method requires a suitable selection for the exchange and correlation energies. In the recent years, progress continues to devise new functionals which explain different molecular properties with satisfactory performance. In general, it is found that GGA methods often give geometries and vibrational frequencies for stable molecules of the same or better quality than MP2 at a computational cost similar to HF [3]. For systems with multi-reference character, where MP2 usually fails badly, DFT methods are often found to generate results of a quality comparable to that obtained with coupled-cluster methods [3].

2.2 Classical Force Fields

Quantum mechanical methods deal with calculating the electronic energy for a given nuclear configuration. In force field methods which are based on classical mechanics, the electronic motion is ignored and the electronic energy is parameterized to experimental or high-level computational data. Molecular mechanics (MM) is thus invariably used to study systems with large number of atoms. In some cases with proper parameterization, molecular mechanics can be as accurate as even the highest-level quantum mechanical calculation using a significantly lower CPU time. However, molecular mechanics cannot, of course, calculate properties which depend on the electron distribution in a molecule.

Nevertheless, molecular mechanics works at all because of some assumptions and their validity. Molecular mechanics is based upon rather simple model interactions within a system, and those contributions of processes such as stretching of bonds, the opening and closing of angles and rotation about single bonds. Simple functions (*Hooke's law*) are used to model such contributions. Transferability is a key attribute of a force field, a set of parameters which are developed and tested for a particular set of molecules, should be applicable to a wider range.

2.2.1 Potential Form

A force field is generally designed to predict certain properties and parameterized accordingly. There are several force field potential functions available. Energetics associated with the deviation of bond lengths and bond angles from their *reference* or *equilibrium* values can be described by a function that tells how the energy changes as bonds are rotated. Another function should describe the interaction between the non-bonded part of the system. One general functional form for such a force field consisting of short-distance bonding forces and long-distance non-bonded interactions is:

$$\begin{aligned}
 V(\mathbf{r}^N) = & \sum_{\text{bonds}} \frac{k_i}{2} (l_i - l_{i,0})^2 + \sum_{\text{angles}} \frac{k_i}{2} (\theta_i - \theta_{i,0})^2 + \sum_{\text{torsions}} \frac{V_n}{2} (1 + \cos(n\omega - \lambda)) \\
 & + \sum_{i=1}^N \sum_{j=i+1}^N \left(4\epsilon_{ij} \left[\left(\frac{\sigma_{ij}}{r_{ij}} \right)^{12} - \left(\frac{\sigma_{ij}}{r_{ij}} \right)^6 \right] + \frac{q_i q_j}{r_{ij}} \right) \quad (2.56)
 \end{aligned}$$

$V(\mathbf{r}^N)$ denotes the potential energy, which is a function of the positions (\mathbf{r}) of N particles. The various contributions are schematically represented in Fig. 2.1. The first term in Eq. (2.56) refers to a harmonic potential which models the interaction between pairs of atoms, and describes the deviation in bond length l_i from the reference value $l_{i,0}$. The second term, again modelled using a harmonic potential is a summation over all valence angles¹ in a molecule. The third term (a *periodic* potential) models the torsional motions. The fourth contribution in Eq. (2.56) is the non-bonded interaction term, calculated between all pairs of atoms (i and j) that are in different molecules or in the same molecule but separated by at least three bonds (*i.e.*, have a $1,n$ relationship where $n \geq 4$). In a simple force field non-bonded interactions are usually modelled by Coulomb potential for electrostatic interaction and a Lennard-Jones potential for van der Waals interactions.

2.2.2 GULP

One of the most commonly used force fields for ionic solids is GULP (general utility lattice program) which has different functional forms depending on whether they should describe short-distance bonding forces or long-distance non-bonding interactions.

¹A valence angle is formed between three atoms A–B–C in which A and C both are bonded to B.

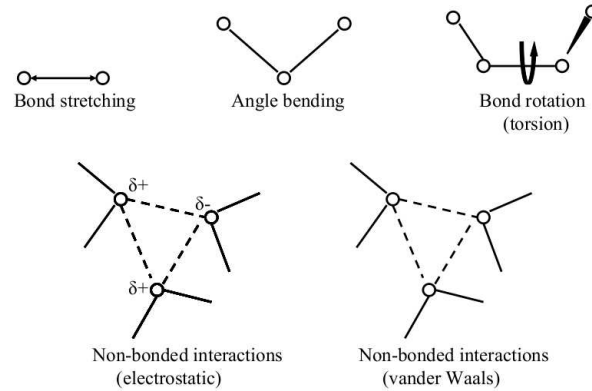


FIGURE 2.1: Schematic representation of the four main contributions to a molecular mechanics force field, adapted from Ref. [33].

Empirical interatomic potentials with particular regard to ionic materials [34] are implemented in the GULP [35] program. The basic form for the potential describing the interaction of a pair of ions is given below:

$$V_{ij} = \frac{q_i q_j}{r_{ij}} + \underbrace{A_{ij} \exp\left(-\frac{r_{ij}}{\rho_{ij}}\right) - \frac{C_{ij}}{r_{ij}^6}}_{\text{Buckingham potential}}. \quad (2.57)$$

Here, i and j refer to the interacting ions, q_i and q_j to their charges, and A_{ij} , ρ_{ij} and C_{ij} are short-range potential parameters. The first term is the Coulomb interaction term. The second one represents the ‘short-range’ Pauli repulsion between two approaching, atomic-centered electron clouds at short distances. The third term describes the dispersive interaction at long distances. The second and third terms together take the form of the Buckingham potential. However, the Buckingham potential has the rather unphysical property of being negatively infinite at zero separation; *so the barrier must be sufficiently large that this region is inaccessible, particularly in molecular dynamics* [34]. To overcome this, several variations of the Buckingham potential have been postulated.

Ionic polarizability can be incorporated by using the shell model potential of Dick and Overhauser [36]. It is an ion pair potential which describes the ions (often anions only) by a pair of point charges, the positive core, and the negative, massless shell coupled by a harmonic force:

$$V_{(\text{core-shell})} = \frac{1}{2} k_{cs} r^2 \quad (2.58)$$

For tetrahedrally coordinated partial covalent materials such as zeolites, the so-called three-body interaction term is included [37, 38].

$$V_{(3\text{-body})} = \frac{1}{2} \sum_i \sum_{jl} k_i^b (\theta_{ijl} - \theta_0)^2 \quad (2.59)$$

The indices j and l run over the shells of all oxygen atoms which are bonded to the T (Si or Al) atom i . The reference angle θ_0 is 109.47° [38].

Therefore the full potential expression is as follows:

$$V = V_{ij} + V_{(\text{core-shell})} + V_{(3\text{-body})} \quad (2.60)$$

2.3 Combined Quantum Mechanics and Molecular Mechanics Methods

Understanding the detailed mechanism (elementary steps) of a chemical reaction is one of the fundamental applications of quantum mechanics. Conformational changes of a complex molecular system can be studied by using empirical potential functions based on ‘classical’ contributions of bond stretching, bond angle bending, bond twisting, non-bonded interactions, etc.. However, it is generally inappropriate for the description of processes involving bond-making or bond-breaking, *i.e.*, chemical reactions. To model such processes adequately, quantum mechanical methods are required. Nevertheless, the region of space within which significant changes in electronic structure occur during the course of a reaction is often relatively small compared to the size of the reacting system as a whole. For example, a very large enzyme may convert one molecule to another in a relatively small volume of space (active site). The rest of the enzyme may be important for maintaining the structure, recognizing co-enzymes, folding, etc., but not responsible to exert any quantum mechanical influence on the catalytic active site.

However, the size of complex systems of interest limits the use of quantum mechanical methods. Therefore, it is necessary to simplify the problem. Thus, from a modeling perspective, we may construct the situation as described in Fig. 2.2 resulting in a combined quantum mechanical (QM) and molecular mechanical (MM) model which is widely used to overcome this limitation. In a QM/MM scheme, the system is divided

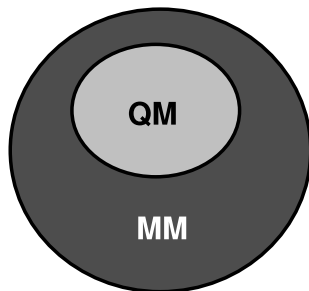


FIGURE 2.2: A simple QM/MM partitioning of a large system.

into two parts – the active site, that makes use of the quantum mechanical tools to accurately model an electronic-structure problem, and the surrounding region, modelled by a force field within the approximation that environmental effects are included in the chemical process.

The complete Hamiltonian for the system must be some kind of hybrid of QM and MM methodologies, defining a so-called QM/MM technique, written in a disarmingly simple fashion

$$H_{\text{complete}} = H_{\text{QM}} + H_{\text{MM}} + H_{\text{QM/MM}} \quad (2.61)$$

where H_{QM} accounts for the full interaction energy of all quantum mechanical particles with each other, H_{MM} accounts for the full interaction energy of all classical particles with each other, and $H_{\text{QM/MM}}$ accounts for the energy of all interactions between the quantum mechanical particles and the classical particles. The first two terms of Eq. (2.61) are already discussed in preceding sections, the last term is in the heart of the hybrid QM/MM methods.

The coupling Hamiltonian $H_{\text{QM/MM}}$ is described as a sum of electrostatic and other non-bonded interactions, and can be written as follows:

$$H_{\text{QM/MM}} = - \sum_i^{\text{QM electrons}} \sum_m^{\text{MM atoms}} \frac{q_m}{r_{im}} + \sum_k^{\text{QM nuclei}} \sum_n^{\text{MM atoms}} \left[\frac{Z_k q_n}{r_{kn}} + 4\epsilon_{kn} \left(\frac{\sigma_{kn}^{12}}{r_{kn}^{12}} - \frac{\sigma_{kn}^6}{r_{kn}^6} \right) \right] \quad (2.62)$$

Taking the expectation value of H_{complete} in Eq. (2.61):

$$\begin{aligned}
\langle \Psi | H_{\text{complete}} | \Psi \rangle &= \langle \Psi | H_{\text{QM}} | \Psi \rangle + \langle \Psi | H_{\text{MM}} | \Psi \rangle + \langle \Psi | H_{\text{QM/MM}} | \Psi \rangle \\
&= \left\langle \Psi \left| \sum_i^N -\frac{1}{2} \nabla_i^2 - \sum_i^N \sum_k^K \frac{Z_k}{r_{ik}} + \sum_{i<j} \frac{1}{r_{ij}} + \sum_{k<l} \frac{Z_k Z_l}{r_{kl}} \right| \Psi \right\rangle \\
&\quad + \langle \Psi | \Psi \rangle H_{\text{MM}} - \left\langle \Psi \left| \sum_i^N \sum_m^M \frac{q_m}{r_{im}} \right| \Psi \right\rangle \\
&\quad + \langle \Psi | \Psi \rangle \sum_k^K \sum_m^M \left[\frac{Z_k q_m}{r_{km}} + 4\epsilon_{km} \left(\frac{\sigma_{km}^{12}}{r_{km}^{12}} - \frac{\sigma_{km}^6}{r_{km}^6} \right) \right] \\
&= \left\langle \Psi \left| \underbrace{\sum_i^N -\frac{1}{2} \nabla_i^2 - \sum_i^N \sum_k^K \frac{Z_k}{r_{ik}} + \sum_{i<j} \frac{1}{r_{ij}} + \sum_{k<l} \frac{Z_k Z_l}{r_{kl}}}_{\text{free QM system}} - \underbrace{\sum_i^N \sum_m^M \frac{q_m}{r_{im}}}_{\text{QM/MM}} \right| \Psi \right\rangle \\
&\quad + H_{\text{MM}} + \sum_k^K \sum_m^M \left[\frac{Z_k q_m}{r_{km}} + 4\epsilon_{km} \left(\frac{\sigma_{km}^{12}}{r_{km}^{12}} - \frac{\sigma_{km}^6}{r_{km}^6} \right) \right] \tag{2.63}
\end{aligned}$$

where i and j run over N electrons in the QM region, k and l run over K nuclei in the QM fragment, and m runs over the M molecular mechanics atoms. The second equality in Eq. (2.63) simply expands the QM Hamiltonian into its individual components and uses Eq. (2.62) to expand the QM/MM Hamiltonian. Following terms are independent of electronic coordinates: H_{MM} , the QM-nuclei/MM-atom electrostatic interactions, and the LJ interactions which can be taken outside of expectation value integrals. The third equality simply collects the components together in a convenient fashion.

Note that, among the electronic coordinates dependent operators in Eq. (2.63), the only operator involving the charges of the MM atoms would not be present in the isolated QM system. In operator formalism, these atoms behave exactly as QM nuclei do, except that they bear partial atomic charges instead of atomic-number-based charges. As such, they enter into the standard Fock operator like nuclear charges, *i.e.*, as part of the one-electron operator. Elements of the QM/MM Fock matrix that minimize the energy computed from Eq. (2.63) are thus calculated as:

$$\begin{aligned}
F_{\mu\nu} = & \left\langle \mu \left| -\frac{1}{2} \nabla_i^2 \right| \nu \right\rangle - \sum_k^{\text{QM nuclei}} Z_k \left\langle \mu \left| \frac{1}{r_k} \right| \nu \right\rangle - \sum_k^{\text{MM atoms}} q_m \left\langle \mu \left| \frac{1}{r_m} \right| \nu \right\rangle \\
& + \sum_{\lambda\sigma} P_{\lambda\sigma} \left[(\mu\nu|\lambda\sigma) - \frac{1}{2}(\mu\lambda|\nu\sigma) \right] \quad (2.64)
\end{aligned}$$

where only the third term in the r.h.s. of Eq. 2.64 differs from the original QM expression. The third term involves the computation of M one-electron integrals and this term accounts for polarization of the QM region due to the MM charges. This type of QM/MM modeling scheme is known as *electrostatic embedding* taking care of Polarized QM/Unpolarized MM. The bottleneck in HF theory is in computing the two-electron integrals. The actual increment in computation time required for the QM/MM calculation compared to the conventional QM calculation for the same fragment is negligible.

Allowing the QM system to be polarized by the MM charges, and at the same time accounting for polarization of the molecules comprising the MM system (MM polarization), *i.e.*, each MM molecule or atom is polarizable, such approach is called fully polarizable QM/MM scheme. In this scheme, evaluation of all of the terms must proceed iteratively until self-consistency is reached. Therefore, it is computationally demanding and used rarely. The first QM/MM approach described by Warshel and Levitt [39] gave such a formalism which is some sort of fully polarizable QM/MM scheme.

So far, the discussed QM/MM procedure refers to one side of a spectrum, called *additive embedding* scheme named because of its additive nature of formulation in Eq. 2.61, and the other side defines the *subtractive embedding* scheme. In this philosophy, the energy of a whole system can be expressed as a linear combination of model compounds of different sizes and at different levels of theory. In the most general form

$$E_{\text{complete}} = E_{\text{QM}}^{\text{small}} + \left(E_{\text{MM}}^{\text{large}} - E_{\text{MM}}^{\text{small}} \right) \quad (2.65)$$

large refers to the complete molecule, treated at the MM level of theory, *small* represents the ‘core’ part whose electronic structure is of primary interest, and it is computed at both QM and MM levels. The primary motivations of this embedding scheme are,

- clearly the simplest method, since every energy computation is to be carried out completely independent of the others.

- all the important quantum effects are captured into the small system and the long-range interactions are well captured as an ‘embedding energy’, *i.e.*, the difference between the MM energy of the small system and the large system.

2.3.1 QM-Pot

I have used a program called “QM-Pot” which makes use of the hybrid QM/MM method. Here the site of interest of a system is computed by a quantum mechanical (QM) method and the embedding environment is described by an empirical potential function (Pot). The QM-Pot program applies the *subtractive embedding* scheme which proved to be successful in describing the structures for silica polymorphs, and the interaction of extraframework molecules with it [38, 40–43]. Both the environment and the active site are completely relaxed. Therefore, it can accommodate the framework distortions caused by the adsorbate-adsorbent interactions.

- In the embedding scheme of the QM-Pot model (cf. Appendix B.2 for implementation details) the system (S) is divided into two regions : (i) inner region (I) which is the active site treated at the QM level, (ii) outer region (O) includes the rest of the periodic system which is described using a polarizable ion-pair-shell model potential. $S = I + O$
- Partitioning of the whole system creates dangling bonds which are saturated by H atoms (link atoms L). The inner part along with the terminating L atoms form the cluster (C): $C = I + L$.
- The QM-Pot energy is expressed in a subtractive scheme as follows:

$$E(S) = E(C)_{QM} + E(S)_{Pot} - E(C)_{Pot} + \Delta \quad (2.66)$$

with,

$$\Delta = -E_{QM}(L) - E_{QM}(I - L) + E_{Pot}(L) + E_{Pot}(I - L). \quad (2.67)$$

In the above equation, $E_{QM}(I - L)$ and $E_{Pot}(I - L)$ are the QM and potential function interaction energies between the inner part and link atoms. If the analytical potential function mimics the QM energy contribution connected to the link

region ideally, then the influence of the link atoms can be neglected. With $\Delta = 0$, the Eq. 2.66 becomes,

$$E(S) = E(C)_{QM} + E(S)_{Pot} - E(C)_{Pot} \quad (2.68)$$

- This scheme substantially depends on the potential function used for MM calculation. The parameterization of the potential function could be performed by quantum mechanical calculations. To maintain consistency, the QM level of theory used for the parameterization should be employed for the embedding calculation also.
- Note that, from Eq. 2.66, the double counting of the contribution from MM potential and QM energy of the inner part is eliminated, and the influence of the L atoms which are not part of the real system is eliminated as well.
- Polarization of the QM wave function by the charge distribution of the outer part is not included. The *free gas-phase* cluster is different from the *embedded* cluster, in a way that the structural changes take place when it is embedded with the outer part, *i.e.*, the relaxation of the nuclei on interaction is constrained when cluster is a part of the solid lattice.

Chapter 3

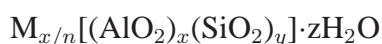
Zeolites

Voids with molecular dimensions can manipulate, separate, arrange, and activate molecules. In a porous solid, the shape and size of voids control these processes, while the chemical identity of functionals and reactive sites control sorptive selectivity and catalytic reactivity. The ordered arrays of atoms lining the pore walls can be thought of as designating a surface internal rather than external to the solid. The best established examples of porous materials with these functions are aluminosilicate zeolites [44].

3.1 Structure and Functionality

What are zeolites? Zeolites are abundant in nature and were discovered by the Swedish mineralogist Cronstedt in 1756 [45]. He observed that a new class of minerals released water while heated rapidly and appeared to boil. Therefore Cronstedt called them “zeolite” originating from two Greek words “*zeo*” and “*lithos*” meaning “*to boil*” and “*a stone*”.

Zeolites are three-dimensional, crystalline, microporous solid materials with orderly-defined structures consisting of Al, Si, O atoms in their regular framework, with the following formula:



M is an exchangeable cation with valency n . Cations and water molecules are located inside the pores. Si and Al atoms (known as T atoms) are tetrahedrally coordinated with each other through O atoms to form a three-dimensional network (Fig. 3.1). These TO_4

tetrahedral units (called primary building units) are linked and form polyhedral units which are further linked and build up the entire framework of a zeolite. Different zeolite frameworks may consist of finite or infinite, *i.e.*, chain- or layer-like polyhedral units. Although zeolites are naturally available, synthetic zeolites are scientifically as well as industrially interesting because of their immense applicability to chemical processes.

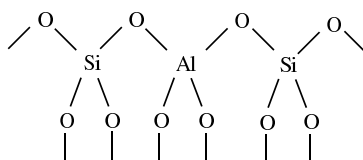


FIGURE 3.1: A simple aluminosilicate chain.

What properties do zeolites make so special? The question arises, what makes a zeolite so special as compared to other crystalline inorganic oxide materials? The answer lies in combination of several properties of zeolites:

- microporous character with uniform pore dimensions,
- shape-selectivity,
- ion-exchange properties,
- ability to develop internal acidity,
- high thermal stability.

Microporous character with uniform pore dimensions: The situation is quite different in zeolites than in non-porous inorganic oxide solids where a small fraction of metal-oxygen atoms in the bulk is exposed. In zeolites, all atoms of the internal micro-pore surface are accessible. Further, the internal surface of the zeolite is intrinsically more rigid because the zeolite structure is built up by aluminosilicate tetrahedra, and consequently the pores are formed by corner-connected tetrahedra.

Shape-selectivity: The shape-selectivity as the phrase says, is a delicate matching of size and shape of the reactant, transition state, and product molecules with the size and shape of the pores of the crystalline zeolites. The reactant selectivity allows certain sized (or shaped) molecules to enter into the pore volume of the zeolite, while the product selectivity typically controls diffusion of the reaction products from the confined space of the zeolite pore. The transition state selectivity excludes formation of several

possible configurations, and the most appropriate one is formed depending on the spatial configuration around a transition state located inside a pore of zeolite. All these properties together influence the rate of a chemical reaction.

Ion-exchange properties: Ion exchange is an intrinsic property of most zeolites, which is reversible as well. This ability arises as a consequence of an isomorphous replacement of a tetravalent framework cation (*i.e.*, silicon) by a cation of lower charge (normally aluminum). This imposes a net negative charge on the framework ($\text{Si}^{4+} \rightarrow \text{Al}^{3+}$) neutralized by cations held within the cavities and channels. These cations can be any metal cations, or alkylammonium cations, and it is the widest variety in nature, and the extent of cation-exchange which may occur in zeolites that provides the richness of its chemistry.

Ability to develop internal acidity:

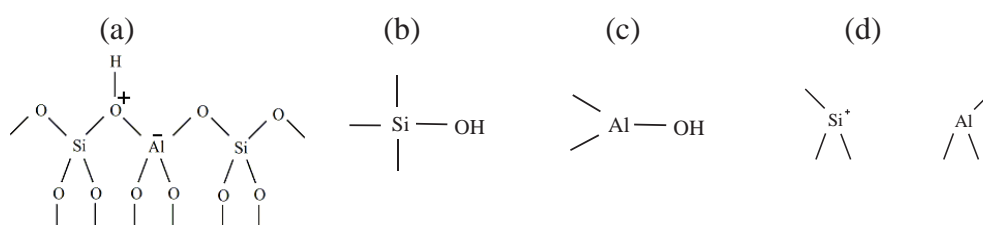


FIGURE 3.2: Schematic representation of different types of hydroxyl groups and acid sites in zeolites. (a) Brønsted acid site; (b), (c) Terminal acid sites (silanol groups, OH gr. at extra-framework aluminum species; (d) Lewis acid sites.

As each Al atom introduces one negative charge, a metal cation (univalent/divalent) or a hydroxyl proton forms a weak Lewis acid site or a strong Brønsted acid site, respectively. Brønsted acid sites, *i.e.*, as proton donors, are located at oxygen bridges connecting a tetrahedrally coordinated silicon and aluminum cation on aluminosilicate framework positions (Fig. 3.2, (a)). These OH groups are commonly referred to as structural or bridging OH groups (Si–OH–Al). The aluminum site distribution is considered to be the primary factor controlling the acid strength of SiOHAl groups [46]. The key reason is the lower electronegativity of aluminum atoms in comparison to silicon atoms. Next nearest neighbors (NNNs) concept can be illustrated by Fig. 3.3. According to the NNN concept, the acid strength of SiOHAl groups in aluminosilicate-type zeolites is affected by the number of framework aluminum atoms on NNN positions. Upon dealumination, on one hand the total acidity of zeolites decreases, on the other hand the strength of the acid sites associated with the remaining aluminum atoms increases in order $3\text{-NNN} < 2\text{-NNN} < 1\text{-NNN} < 0\text{-NNN}$ [47]. See Fig. 3.3.

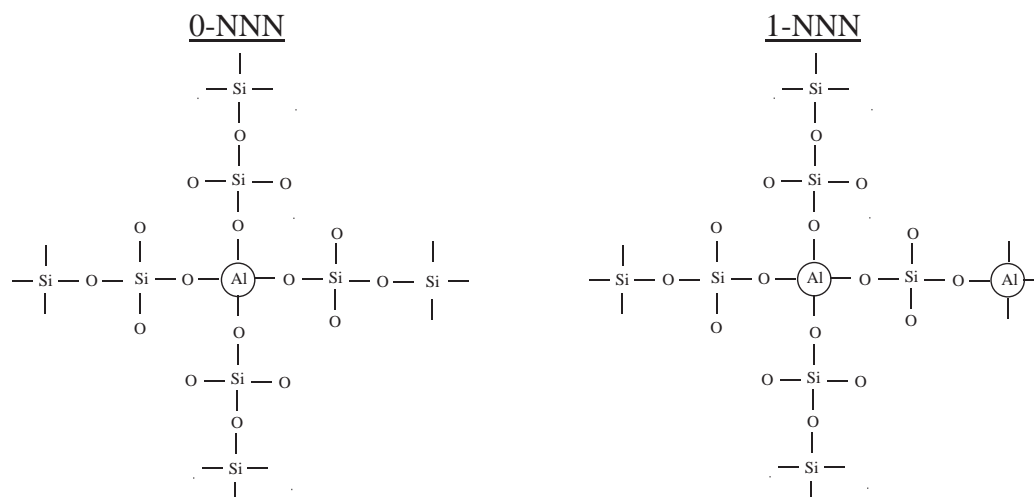


FIGURE 3.3: Next nearest neighbour (NNN) concept.

High thermal stability: Silica-rich zeolite materials often exhibit high thermal and hydrothermal stabilities which allow their use as catalysts at high temperatures, and their oxidative regeneration even in the presence of steam.

3.1.1 Application

There are several applications where the ion-exchange properties of zeolites are directly exploited. These include:

- as water softeners (or “builders”) in detergents
- in waste water treatment (including municipal, industrial, agricultural waste water)
- in radioactive waste treatment

The prime catalytic applications are in petrochemical processes especially in fluid catalytic cracking (FCC) process. Zeolites are used as drying agent, as desiccant in gas purification, in separation process. See Table 3.1, which relates a particular property with its application.

3.2 Catalysis

As shown in Fig. 3.4, catalysis is not the largest market segment of the application of zeolites, but for synthetic zeolites the highest market value lies in catalytic purposes [48]. The FAU-type zeolite covers more than 95% of the catalysis market [49, 50]. In

TABLE 3.1: Properties and applications of zeolites.

Property	Natural zeolites	Synthetic zeolites
Adsorbing agent		Drying of gases and fluids
Catalyst		Cracking processes, synthesis of fine chemicals
Filler	Pozzolan cement Paper additive Soil improvement Cat litter	
Ion exchanger	Sewage treatment	Detergent builder

petrochemical processing, zeolites (mainly zeolite Y) are used as catalysts for Fluid Catalytic Cracking (FCC process), a process which transforms long-chain alkanes (heavy oil) into shorter ones (petrol), and to enhance the octane number of the petrol by producing branched species.

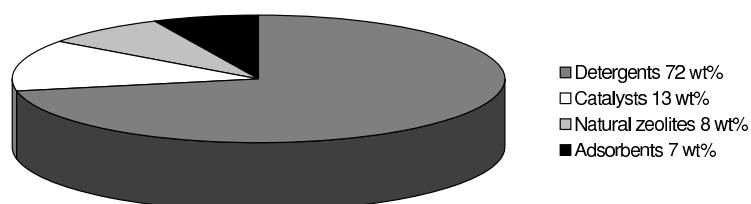


FIGURE 3.4: Estimated annual zeolite consumption (wt% of total 1.8 million metric ton) by the major individual applications, excluding China's annual > 2.4 million metric tons of natural zeolite consumption [48].

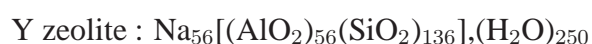
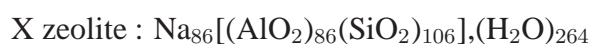
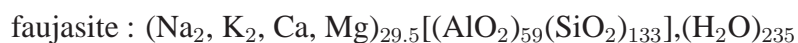
3.3 Faujasite Zeolite

Faujasite zeolite is categorized as a framework *type* called **FAU** by the Structure Commission of the International Zeolite Association (<http://www.iza-structure.org/>) according to rules set up by an IUPAC Commission on Zeolite Nomenclature published in the *Atlas of Zeolite Framework Types* [51] and in the internet at <http://www.iza-structure.org/databases/>.

Early history: Faujasite zeolite was named in honor of the French geologist Barthelemy Faujas de Saint-Fond in 1842. The zeolite X and Y are isomorphs or isostructural with

the naturally occurring mineral faujasite. The founding father of synthetic zeolites, Dr. Robert M. Milton had synthesized zeolite X in high purity by 1950, and in 1954, he discovered zeolite Y together with Dr. Donald W. Breck [52, 53]. The removal/dealumination of framework aluminum leads to “*ultrastable Y*” zeolite which is thermally and hydrothermally stable, thus making it almost the prime commercial hydrocracking catalyst. Starting from 1960s, several methods have been developed to prepare highly siliceous faujasite structures [54], but it is important to understand that dealumination of framework aluminum results in a decrease of the number of acid sites, and thus effectively show low catalytic activity in cracking reactions. Therefore, to prepare a optimum catalyst, a compromise must be reached between high thermal stability and sufficient acid sites to maintain activity. Selectivity is highly important commercially, regardless of the methods used. For the past four decades, transition metal ion exchanged zeolites have attracted great interest. Cu-exchanged Y zeolites are investigated in terms of their structural aspects, and catalytic activities [55–60]. Several chemical reactions have been studied in order to know the catalytic behavior, and optimized for their potential environmental applications. The removal reaction of undesired NO as byproduct from chemical plant exhaust gases always holds the attention. Numerous studies have been reported on interaction of NO with CuY zeolite, and on the transformation of NO into N₂, O₂ with or without reductants [61–67].

Chemical composition and framework structure: The unit cells of faujasite and zeolites X and Y are cubic, $a_0 \sim 25 \text{ \AA}$, and each of them contains 192 silicon- or aluminum-centered oxygen tetrahedra which are linked through shared oxygen atoms. Because of the presence of net negative charge on each of the aluminum-centered tetrahedra, each unit cell contains an equivalent number of charge-balancing cations (H⁺, Na⁺, Cu⁺, etc . . .). These are exclusively Na⁺ ions in zeolites X and Y in their synthesised form, and a complex distribution of several cations such as sodium, potassium, magnesium, and calcium in naturally-occurring faujasite. Typical cell compositions for the three zeolites in the hydrated form are:



Zeolites X and Y are conventionally distinguished on the basis of the relative number of silicon and aluminum atoms, and the consequent effects on structural properties and related chemical and physical properties. The aluminum atoms in the unit cell of zeolite

X vary from 96 to 77 giving a Si : Al ratio between 1 and 1.5, whereas for zeolite Y they vary from 76 to 48 giving a Si : Al ratio between 1.5 and 3.0 [68]. The primary building units are the TO_4 tetrahedra, where T is any tetrahedrally coordinated cation, and the secondary building units are sodalite cages (or β -cage) and double 6-rings (or hexagonal prism) (Fig. 3.5). Sodalite cages are connected via double 6-rings and form the so-called supercage (or α -cage) with four tetrahedrally oriented 12-ring pore openings. A 12-ring has a diameter or pore width of 7.4 Å. The α - and β -cages together create $\sim 50\%$ void volume of the dehydrated X and Y zeolite.

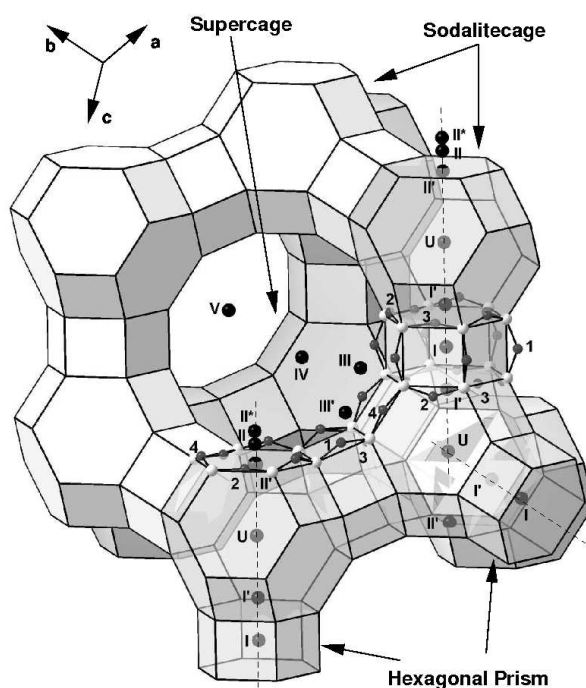


FIGURE 3.5: Structure of Y zeolite (faujasite) consisting of sodalite cages and hexagonal prisms forming the supercage.

Cation position: Zeolite Y has three dimensional periodic crystalline structure, and cations are distributed at variety of crystallographic positions. Crystallographic studies have presented at least 6 potential positions for Cu [68–71]. According to the nomenclature of Smith [71], cations are mainly located at site I, I', II, II', III (Fig. 3.6). The cation sites are:

Site I at the center of an hexagonal prism;

Site I' in the β -cage adjacent to an hexagonal face shared by a sodalite unit and an hexagonal prism;

Site II in the α -cage adjacent to an unshared hexagonal face of a sodalite unit;

Site II' in the β -cage adjacent to an unshared hexagonal face of a sodalite unit;

Site II* as II, but displaced further into the α -cage;

Site III in the α -cage adjacent to a four-membered ring of a sodalite unit

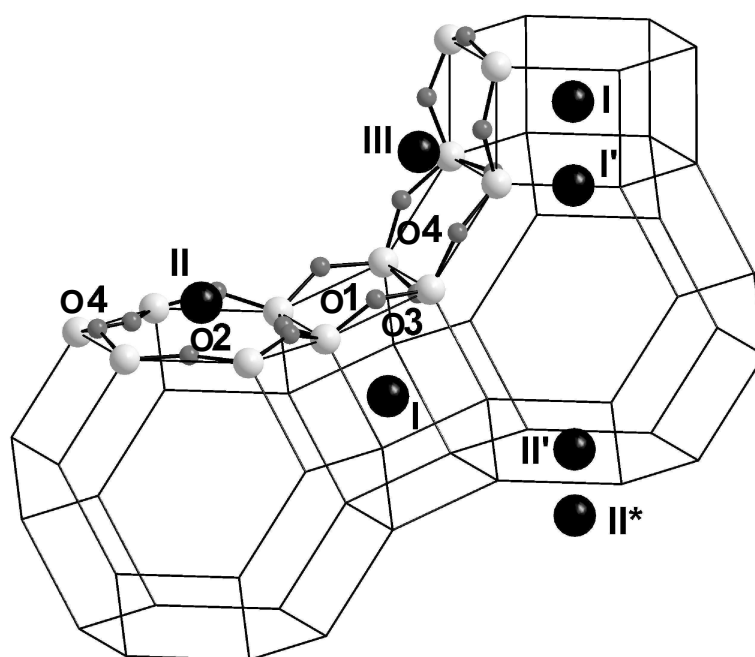


FIGURE 3.6: Copper sites (black balls) in Y zeolite: vertices are occupied by T (Si/Al) atoms; the light and dark grey balls represent T atoms and crystallographic oxygen positions (O1, O2, O3, O4), respectively.

Cations located at site I are octahedrally coordinated by 6 framework oxygens, because of that highly populated by cations. Therefore those are practically inaccessible for guest molecules. Site I' cations are tri-coordinated (three oxygens of the base of the prism). They are accessible only to molecules which can penetrate through a 6-membered ring from the supercage into the sodalite cage. CO and N₂ molecules [72] cannot penetrate, although H₂ [73] can do that.

Sites II and II' are coordinated to three framework oxygens. The simultaneous occupation of adjacent I, I' sites and II, II' sites is forbidden, because of Coulombic repulsion. Palomino et al. [74] reports that site III is occupied by Cu only at low Si/Al ratios (X zeolite). Maxwell and Boer [70] describes Cu at sites I, I', II, II', III in dehydrated Y zeolite, on the other hand in the hydrated form only the copper ions at site I' have been located with certainty. They also report that site III cations are favorably located for the

interaction with the adsorbate molecules. In the dehydrated form, the relatively strong Cu(II) binding to the zeolite framework causes a large framework deviation particularly lengthening of the Si(A1)–O bonds.

3.3.1 Characterization Techniques for Zeolites

Characterization of zeolite materials are aimed at elucidating the exact structure, in particular the location, coordination, and valence states of transition metal ions which are thought to be the active species. Such information are of high importance, as they help to modify or develop sorbents, catalysts. Several authors have published articles on spectroscopic studies of Cu(II) and Cu(I) locations in Y zeolite, such as X-ray diffraction (XRD), electron paramagnetic resonance (EPR), and infrared spectroscopy (IR) [69, 70, 74–76].

Individual analysis techniques probe particular aspects of a zeolite material. Therefore, for an overall characterization of a zeolite, a combination of experimental as well as theoretical methods is highly required.

Before going into infrared spectroscopy in detail, just a brief overview should be given as, how some of the most important experimental techniques have been applied to furnish information about the 3-dimensional crystal structure of zeolite. Table 3.2 shows a brief outline of some characterization techniques, and their usage in zeolites.

X-ray diffraction (XRD): X-ray diffraction experiments are the most widely used methods for analyzing long-range ordered structures of crystalline zeolite materials. They yield precise information about structural details at the atomic level, including the locations of the exchangeable cations. The minimum set of information one can get from diffraction experiments is: *unit cell* size, *space group* (gives information about *lattice* type and the *symmetry*), and a list of relevant atomic coordinates. One limitation of XRD in structure determination of Y zeolite is that there is no distinction between Si and Al atoms. As a result, the symmetry is overestimated and structures show equivalent Si–O and Al–O bond lengths as well as O–Si–O and O–Al–O angles.

X-ray absorption spectroscopy (XAS): The chemical composition of Cu(I)/Cu(II) can be obtained by XAS. In addition, the EXAFS (Extended X-ray Fine Absorption Spectroscopy), the XANES (X-ray Absorption Near-Edge Structure) techniques have also been used to characterize the local environment and bond distances, oxidation states of Cu, and the extent of disorderness present in the vicinity of Cu. Palomino et al. [74]

TABLE 3.2: A brief outline of characterization techniques

Technique	Abbreviation	Structure	Pore size	Chemical composition	Functional groups
X-ray diffraction	XRD	•		•	
X-ray absorption spectroscopy	XAS	•		•	
Infrared spectroscopy	IR	•			•
Nuclear magnetic resonance	NMR		•	•	•
Electron paramagnetic resonance	EPR			•	

observed Cu(I)–O bond distance of ~ 2.02 Å and Cu(I) has around three-fold (2.8 – 3) coordination in Cu(I)–Y zeolite. Whereas, similar results have been reported in case of partially exchanged Cu(I) ($\sim 70\%$) from Na–Y sample [77] indicating that Cu(I) has slightly lower coordination than Cu(II).

Electron paramagnetic resonance (EPR): An alternative way of gaining coordination information of transition metal exchanged zeolite is EPR, provided the sample is paramagnetic. EPR spectra are obtained with low Cu(II) loadings to avoid magnetic dipole interactions between Cu(II) centers. A characteristic EPR spectrum provides g tensor values and hyperfine coupling constants which allow for a correlation between the coordination number of transition metals in the framework [76]. Pierloot et al. [78] have reported that the different aluminum distributions in the six-ring site give rise to two different sets of g -factors, which is consistent with the presence of two different signals in the EPR spectra of CuNa-FAU. Those signals at $g_{||} = 2.32$ and $g_{||} = 2.37$ were tentatively assigned to Cu²⁺ ion on the six-ring site with one or two Al and to Cu²⁺ on the six-ring site with more than two Al, respectively. Even adsorbate-adsorbent interaction in partially copper ion exchanged Na–Y zeolite (CuNa–FAU) were measured by EPR technique in the presence of paramagnetic gases such as nitrogen monoxide (NO) and oxygen (O₂) [79].

Nuclear magnetic resonance (NMR): NMR can measure the framework Si/Al ratio in zeolite. High-resolution solid-state ^{29}Si NMR technique was used to determine detail information about Si, Al ordering in faujasite zeolite by Ramdas et al. [80]. The geometry and the location of the bridging hydroxyl (Si–OH–Al) groups in the zeolite framework was examined by ^1H MAS NMR measurements [81].

3.3.2 IR Spectroscopy of Y Zeolite

Infrared spectroscopy is a very useful and common technique for investigations of zeolites even in *in situ* experiments. It gives information about structures, strength of bonds, and adsorbed molecules. The spectral range of absorption infrared (IR) spectroscopy is approximately subdivided into three parts:

	Wavenumber	Wavelength
far-IR	$\sim 10 - 400 \text{ cm}^{-1}$	1 - 0.025 mm
mid-IR	$\sim 400 - 4000 \text{ cm}^{-1}$	25 - 2.5 μm
near-IR	$\sim 4000 - 12500 \text{ cm}^{-1}$	2.5 - 0.8 μm .

Framework vibrations: Framework vibrations of zeolites typically give rise to bands in the mid and far infrared region depending on the framework composition and on the manner in which the individual tetrahedra ($\text{TO}_{4/2}$) are interlinked. Table 3.3 gives an overview of the framework infrared bands [82]. The bands showing up in the mid infrared region were grouped into two main categories: (i) bands due to internal vibrations of $\text{TO}_{4/2}$ tetrahedra (T = Si or Al) named as *Intra-tetrahedral bands*, and (ii) external vibrations of tetrahedral linkages e.g. double rings or pore openings defined as *Inter-tetrahedral bands*. *Intra-tetrahedral* vibrational bands appeared in the ranges 1250–950, 720–650 and 500–420 cm^{-1} which were assigned to the asymmetric stretching ($\leftarrow\text{OT}\rightarrow\leftarrow\text{O}$) mode, the symmetric stretching mode ($\leftarrow\text{OTO}\rightarrow$), and the T–O bending of $\text{TO}_{4/2}$ tetrahedra respectively. Similarly bands in the region of 650–500 and 420–300 cm^{-1} were assigned to vibrations of double four-membered rings (D4R) or double six-membered rings (D6R), and pore opening vibrations respectively. It was found out by a comparison between spectral and structural features that the *Intra-tetrahedral* vibrations are greatly structure insensitive whereas *Inter-tetrahedral* vibrations are often sensitive to structure. For example, *Intra-tetrahedral* modes are only little affected when the zeolite structure is partially collapsed by a thermal treatment or so, but the *Inter-tetrahedral* modes decrease in intensity and finally disappear upon the destruction of the characteristic zeolitic structure. A theoretical investigation

studied by de Man and van Santen [83], gives an excellent comparison between framework structure and vibrational spectra.

TABLE 3.3: Assignment of zeolite framework vibrations.

Intra-tetrahedral bands (structure insensitive)	
Asymmetrical stretch	$\sim 950-1250 \text{ cm}^{-1}$
Symmetrical stretch	$\sim 650-720 \text{ cm}^{-1}$
O–T–O bending	$\sim 420-500 \text{ cm}^{-1}$
Inter-tetrahedral bands (structure sensitive)	
Double ring	$\sim 500-650 \text{ cm}^{-1}$
Pore opening	$\sim 300-420 \text{ cm}^{-1}$
Symmetrical stretch	$\sim 750-820 \text{ cm}^{-1}$
Asymmetrical stretch	$\sim 1050-1150 \text{ cm}^{-1}$

Hydroxyl groups: IR spectroscopy is the most direct and useful method to study hydroxyl groups of a zeolite. The OH stretching vibration (ν_{O-H}) depends on several factors, such as, chemical composition of the zeolite, Si–O, Al–O bond lengths, T–O–T bending angle, location in the framework, and the coordination of the framework oxygen of the OH group, *i.e.*, a terminal versus a bridging hydroxyl oxygen can have different effects. Bridging hydroxyl groups ((Si–OH–Al) groups, Brønsted-type acid sites) show up in most types of zeolites between 3550 and 3680 cm^{-1} . For HY zeolite, two bands appear at 3570 and 3650 cm^{-1} , assigned to –OH group in six-ring windows of the sodalite cages, and –OH group pointing into the supercages respectively [84]. Complexity arises in assigning the hydroxyl group, while it forms hydrogen-bonds with the framework oxygen atoms. Typically ν_{O-H} is lowered for hydroxyl groups in the six-ring windows than in supercages while forming H-bond with the framework oxygen atoms in the sterically crowded environment. In addition to the strong Brønsted acidic bridging hydroxyl groups, non-acidic terminal silanol groups Si(OH) in zeolite are observed in the high-frequency region ($\sim 3740 \text{ cm}^{-1}$). However the presence of hydrogen-bonding interaction shifts the band to $\sim 3500 \text{ cm}^{-1}$ [84].

Cation vibrations: The frequencies of stretching vibrations of the charge balancing cations relative to the zeolite lattice depend on the charge, mass and location of the cations in the zeolite lattice. For example for Na^+ in faujasite, bands at 160 , 108 , 190 and 80 cm^{-1} were observed, which were assigned to cations in I, I', II and III positions, respectively [84]. However Cu^+ , Cu^{2+} in CuHY zeolite show up at 979 and 918 cm^{-1} [1].

Probe molecules-adsorbates: IR spectroscopy is extensively employed to characterize zeolite-adsorbate interactions. If the goal is to study a particular property of a zeolite such as sorption, catalysis, acid strength, cation positions etc. then it is advantageous to use the reactants or target molecules as probes. Adsorption can take place at different active sites of a zeolite like Brønsted acidic sites, cation exchanged positions (Lewis acid sites). IR spectroscopic studies of O₂, CO, H₂ adsorption onto zeolite have been studied by several authors [85–87]. Brønsted acidic sites (Si–OH–Al) and Lewis acidic groups are differentiated [88] using a probe molecule such as pyridine which is the most frequently used base. The frequency of the ring deformation vibration of pyridine allows to distinguish whether it is adsorbed on Brønsted acid sites in the form of pyridinium ions (1544 cm⁻¹) or coordinatively adsorbed on Lewis acid sites (1455–1442 cm⁻¹) [84]. A similar distinction is made for the adsorption of NH₃ ligand where the formation of NH₄⁺ ions (band at 1450 cm⁻¹) indicates the presence of Brønsted acid sites, while the coordinative adsorption of NH₃ on Lewis acid sites results in a band at 1640 cm⁻¹ [84]. When CO is adsorbed to a cation-exchanged zeolite the C atom of the CO molecule interacts with cations and leads to a blue shifted CO stretching vibration (ν_{CO}) compared to the gas phase value (2143 cm⁻¹). The adsorption of CO on M–Y zeolite (M = alkali metal ion) shows that the highest frequency for ν_{CO} is observed for Li–Y, and a continuous decrease down to 2145 cm⁻¹ for Cs–Y is observed [89].

Chapter 4

Benchmark Studies

4.1 Computational Details

QM methods: Quantum chemical calculations have been performed using density functional theory (DFT). A combined quantum mechanics and molecular mechanics (QM/MM) approach has been employed. The Becke-Perdew-1986 (BP86) density functional [28–32] within a resolution-of-identity (or density fitting) implementation has been used throughout [90, 91]. In addition, the Becke3-Lee-Yang-Parr (B3LYP) [28–30, 92, 93] hybrid functional has been used in some particular cases.

Basis sets used: For DFT calculations, two different all electron basis sets have been tested for the treatment of all atoms (H, O, C, Si, Al) but copper: the valence double- ζ SVP basis and the valence triple- ζ TZVP basis [94]. For copper the relativistic small core ECP10MDF pseudopotential [95] (replacing the 10 innermost electrons) in combination with the cc-pVDZ-PP and cc-pVTZ-PP basis sets has been used [96].

QM-Pot: QM/MM calculations have been performed using the QM-Pot program which couples the TURBOMOLE [97, 98] program for quantum mechanical calculations with the GULP [34, 35] program for lattice energy minimization. As discussed in Section 2.3.1, it makes use of a subtractive QM/MM scheme. In this embedding scheme, a system is divided into two parts, (*i*) an active part treated at the QM level which contains the Cu^+ –adsorbate (either O_2 or C_6H_6 or both C_6H_6 and O_2) moiety and the zeolitic framework in the vicinity of this moiety, and (*ii*) the environment described by interatomic potential functions which includes the rest of all the atoms of the periodic cell.

The QM-Pot program provides optimizers for minima, saddle points as well as the computation of the Hessian matrix, *i.e.*, the 2^{nd} derivatives of energy with respect to all atomic coordinates. The optimization strategy follows two key steps: (i) A minimum or transition structure is searched using the interatomic potential functions alone. The Hessian matrix is obtained for the stationary point (structure) found. (ii) A search on the QM-Pot potential energy surface is done using the structure and Hessian matrix obtained in step (i) [99]. The QM-Pot gradients are used to update the Hessian matrix. Proton transfer reactions in zeolite catalysts studied by Sierka and Sauer [99] demonstrate the combined QM-Pot approach as a tool for investigating potential energy surfaces in extended systems like zeolites. In the present work, a similar combined QM-Pot approach is used to study the oxidation reaction of benzene to phenol using dioxygen in Cu–Y zeolite describing the reaction center as accurate as possible with modest computational expense.

MM parameters: The interatomic potential functions (also called force fields) provide a theoretical prediction of the structure of the whole system, thereby producing an analytic approximation to the potential energy surface of the system. Traditionally, empirical interatomic potentials have been used, and they are system specific, even property specific. However, as long as parameters are transferable within a particular kind of systems, one can use them. Sierka and Sauer [43] developed an ion-pair shell-model potential with functional parameters using quantum mechanical DFT calculations for aluminosilicates which are the building blocks of zeolites. These DFT parametrized potentials are used to describe structures and vibrational properties of silica polymorphs with a reliable agreement with experimental data. Structural parameters are presented for faujasite zeolite in Ref. [43] using different approaches: DFT and HF free clusters, DFT- and HF-derived shell-model potentials, and also with the combined QM-Pot approach. The parametrization of ion-pair shell-model potential based on DFT calculations gave reliable predictions for structures and properties of zeolites [43]. Therefore those parameters from DFT calculations are used in the present study. (MM parameters are described in Appendix, B.3. A Cut-off radius of 10 Å is chosen for calculating the summation of the short-range interactions. The interaction parameters for Cu(I) are: $A_{Cu(I)O} = 2676.727189$ eV and $\rho_{Cu(I)O} = 0.24243$ Å [100].) The QM cluster was cut out in such a way that the cluster terminates with OH groups. The hydrogen link atoms are kept fixed at a distance of 96.99 pm (for DFT) from terminating oxygens of the cluster.

Within the QM/MM calculations van der Waals interactions between molecular oxygen

(benzene) and the zeolite framework oxygens are modeled by a Lennard-Jones 6-12 potential solely in the MM region with parameters taken from Ref. [101, pages 1111 & 1112]. Periodic boundary conditions are imposed in order to account for long-range electrostatic effects.

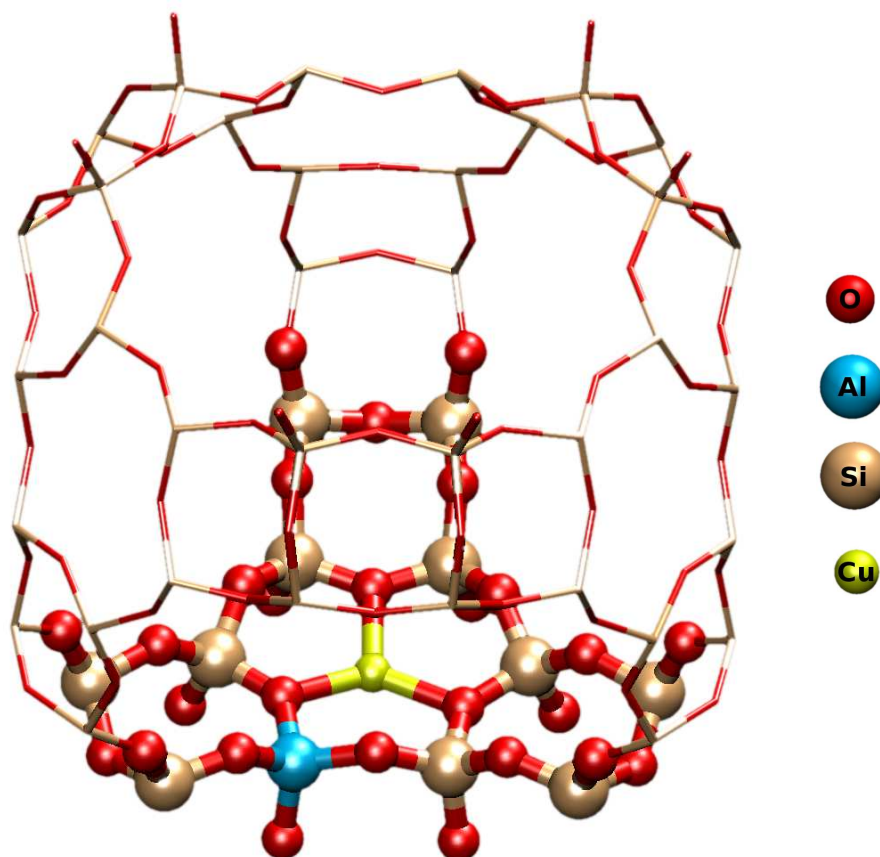


FIGURE 4.1: QM/MM model for Cu–Y zeolite: cluster treated at the quantum mechanical level is depicted as balls and sticks; site II is modelled by 12 Si/Al atoms.

System set-up: Interactions of adsorbates (O_2 , C_6H_6 , and both simultaneously) with the Cu(I) ion at site II, which is located above the 6-membered rings of sodalite cages and at site III, which is located in the fold between two 4-membered rings in the supercages of Y zeolite (faujasite zeolite) (Fig. 3.6), are studied in this work. The full unit cell ($Fd\bar{3}m$) of faujasite zeolite contains 192 Si/Al atoms (called T atoms because of their tetrahedral coordination) and 384 O atoms (in dehydrated Y zeolite), but a smaller rhombohedral unit cell containing just 48 Si/Al atoms and 96 O atoms (Figs. 4.1 & 4.2) is taken in the present work. Y zeolite has only one symmetry distinct crystallographic position of T atoms, whereas it has four different O positions (O1, O2, O3, O4). As discussed in Section 3.3, 6 types of possible cation sites can be distinguished. An aluminosilicate ring consisting of n T (Si, Al) atoms is represented as n T ring or cluster.

The QM part of the Y zeolite model contains one or two Al atoms, whereas the embedding part of it is pure silica. In case of clusters containing 2 Al atoms, an additional H^+ ion is incorporated in order to neutralize the charge of the zeolite. Distribution of the second Al atom follows the Loewenstein rule [102], *i.e.*, Al–O–Al connectivity is excluded. Model clusters of Y zeolite (representing the QM of the QM/MM calculations) are set up by 12 Si/Al atoms and 33 O atoms in case of site II, *i.e.*, site II is modeled by a 12T cluster which consists of one 6T ring and three 4T rings (see Fig. 4.1). Site III is described by an 8T cluster model, consisting of three 4T clusters. 8 Si/Al atoms and 22 O atoms in case of site III, (Fig. 4.2) are treated at the DFT level. After introduction of the 2nd Al into the model clusters (which are embedded within the zeolite framework), each of these two sites gives 9 isomers depending on the position of the two Al atoms to each other.

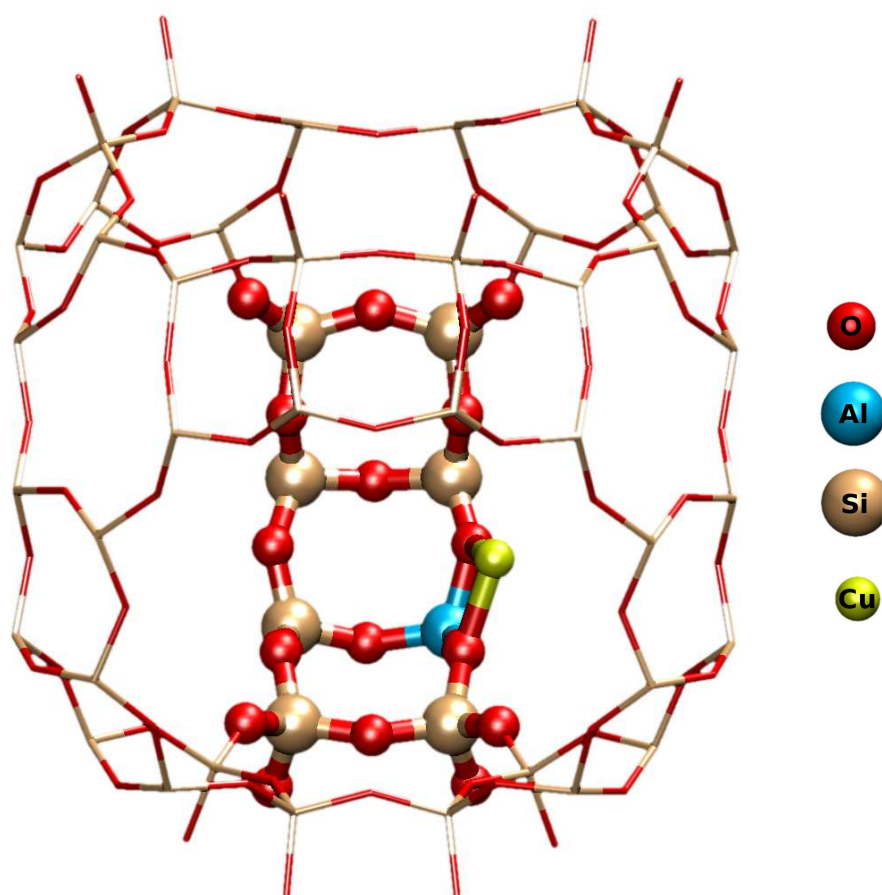


FIGURE 4.2: QM/MM model for Cu–Y zeolite: cluster treated at the quantum mechanical level is depicted by balls and sticks; site III is modelled by 8 Si/Al atoms.

There are many more different model clusters chosen for checking the convergence in the cluster size. In order to limit the computational effort in some of the benchmark

calculations, a small cluster has been used for site II, comprising only 6 Si/Al atoms and 18 O atoms - this will be mentioned explicitly in the corresponding section.

4.2 Basis Set Effects

The computational demands of the QM/MM calculations are dominated by the DFT calculations of the active sites. In order to reduce the computational cost, the basis set should be kept as small as possible while it should be able to represent the structural parameters as accurately as possible. All geometries of adsorption complexes of O₂ and C₆H₆ in zeolite at both sites II and III are optimized using an SVP and a TZVP basis set for studying basis set effects. Within these test calculations, a smaller QM region comprising only 6 T atoms for site II is used, and site III consists of an 8T cluster. As an example, Table 4.1 shows selected structural parameters of dioxygen adsorbed to site II containing only one Al atom. (In Appendix A.1, the geometrical parameters of all the bare Cu-complexes containing 2 Al atoms using both basis sets are given.) While the bond lengths of the CuO₂ moiety are in fairly nice agreement, rather large deviations of up to 0.5 Å can be seen for the distances between the copper atom and the oxygen atoms of the zeolite framework. This indicates that the position of the Cu(I) ion within the zeolite framework is very sensitive to small effects, *i.e.*, the potential energy surface is very flat and the Cu atoms “float” within the oxygen basin. Consequently, the basis set requires sufficient flexibility to describe this situation properly. Since the SVP basis does not contain diffuse functions which are needed for an appropriate description of this situation all further calculations of the study refer to the more accurate TZVP basis.

TABLE 4.1: Basis set dependence of some selected geometrical parameters of O₂ adsorbed to site II with one Al atom. Bond lengths are given in Å. For the numbering of the atoms see Fig. 5.1.

	SVP	TZVP
O'–O''	1.260	1.271
Cu–O'	1.883	1.828
Cu–O4a	2.565	2.185
Cu–O2a	2.224	2.555
Cu–O2b	2.434	2.982
Cu–O2c	1.988	1.984

4.3 QM/MM Calculations vs. Molecular Fragment Calculations

The impact of environmental effects on structural parameters of the active site was studied by comparing results from DFT/MM calculations and DFT calculations on the QM cluster. For cluster fragment calculations at the QM level, initial geometries are taken from QM/MM optimized calculations. There are at least three sources of inherent errors for cluster fragment calculations. (i) Difficulties arise while optimizing the geometry of the fully relaxed cluster fragment due to the formation of the artificial intra-molecular hydrogen-bonds between the cluster terminating OH groups. (ii) The wavefunction is perturbed near the cluster boundary. (iii) Long-range interactions are neglected.

Because the cluster is cut out from the zeolite structure, artificial “dangling bonds” are created at the cluster boundaries and those are saturated with hydrogen atoms. Hydrogen atoms are kept along the direction to the neighboring framework atoms. The influence of the zeolite framework on the active site was mimicked by freezing either OH-bonds or H atoms to the positions obtained from the DFT/MM calculations. Table 4.2 shows the same set of geometrical parameters as has been chosen for studying the basis set effects. Environmental effects appear to be less pronounced than basis set effects.

TABLE 4.2: Dependence of some selected geometrical parameters of O₂ adsorbed to site II with one Al atom on the computation scheme. Bond lengths are given in Å. For the numbering of the atoms see Fig. 5.1.

	H frozen	OH frozen	QM/MM
O'–O''	1.269	1.272	1.271
Cu–O'	1.828	1.833	1.828
Cu–O4a	2.033	2.147	2.185
Cu–O2a	2.717	2.539	2.555
Cu–O2b	3.402	3.015	2.982
Cu–O2c	2.029	1.962	1.984

However, within the frozen cluster models an ambiguity shows up:

Here, from Table 4.2 one can see that OH-constrained cluster gives results which are close to the QM/MM results compared to the H-constrained ones. Therefore a question arises to which position should the terminating H atoms (or the corresponding OH

bonds) be frozen in order to mimic the zeolite framework. Since the initial geometries for the frozen cluster model calculations are provided by the QM/MM results, the effects shown do not include the error introduced by fixing the coordinates to some estimated values (in the absence of QM/MM results). Consequently, without relying on QM/MM data the overall error of frozen cluster models must be expected to be even larger. In order to limit the error and to avoid this ambiguity, the QM/MM scheme has been chosen for calculations of the interaction energies of O₂, C₆H₆ with Cu–Y zeolite, and vibrational frequencies of O₂, C₆H₆, and barrier heights of the oxidation reaction of benzene to phenol.

In spite of all the problems mentioned above, cluster models are used advantageously for performing some special tasks in zeolite modeling. Using a smaller cluster size, post-HF methods, even state-of-the-art CCSD(T) method are employed for benchmark calculations. In any case, cluster model calculations bring information about the detail topology of zeolite structure and properties of the active sites.

4.4 Size of the Embedded Cluster

A sensitive parameter within the QM/MM calculations is the size of the QM region. A QM region being too small may result in artifacts. Consequently, rather large QM regions have been suggested by other authors [103, 104], but usually at the cost of the quality of the basis set.

Therefore, calculations were performed with different sized QM clusters. For site II, two different sized clusters consisting of 6 and 12 T atoms are used, while QM regions of 8T and 10T clusters are chosen for site III. Tables 4.4 & 4.6 show the results of differently sized clusters.

For site II, the maximum difference in the relative energies between 6T- and 12T-adsorption complexes is ~ 6 kcal mol⁻¹ whereas in the case of bare Cu–complexes, it is ~ 10 kcal mol⁻¹. These results indicate that a model comprising 6 T atoms is too small, and thus, the 12T cluster model should be considered. On the contrary, for site III, the maximum difference in the relative energies of 8T- and 10T-adsorption complexes is only ~ 0.5 and in the case of bare Cu–complexes, it is ~ 1.1 kcal mol⁻¹. This suggests a QM region of 8 T atoms can be used for calculating molecular properties.

Moreover, the O₂ stretching mode, which will be used for analyzing the zeolite is a

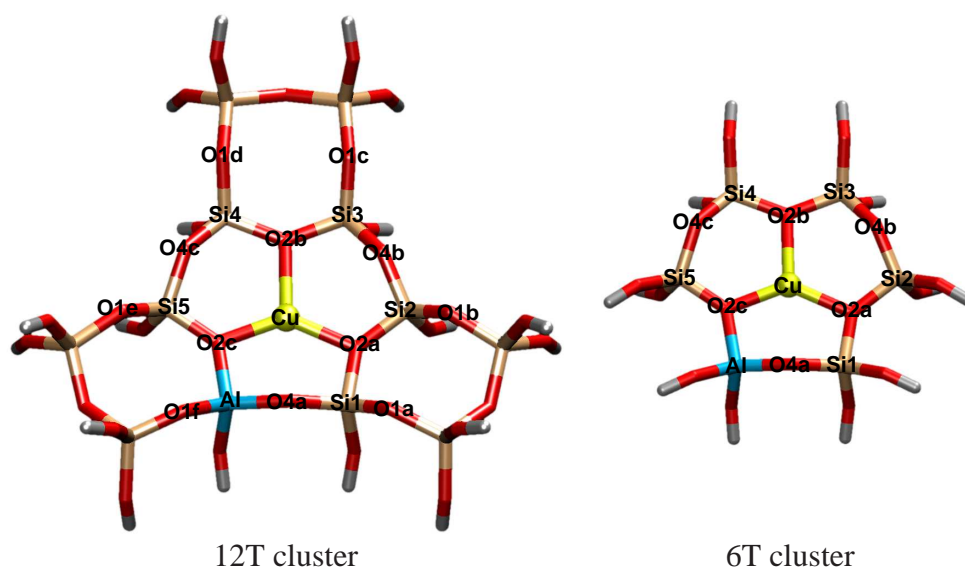


FIGURE 4.3: Quantum mechanically treated zeolite fragment (12T cluster and 6T cluster with 1 Al) without adsorbate at cationic site II. The second Al atom replaces any of the Si atoms except the neighbouring ones.

TABLE 4.3: Site II: labeling of Cu–Y zeolite model complexes (with/without adsorbates) according to the replacement of a Si atom by a second Al atom and the position of the additional H atom sitting on a zeolite framework oxygen atom. For the numbering of the atoms see Fig. 4.3/12T cluster.

Isomers	2^{nd} Al atom replaces	H atom is connected to
A	Si2	O2a
N1	Si2	O1b
B	Si2	O4b
C	Si3	O4b
N2	Si3	O1c
D	Si3	O2b
E	Si4	O2b
E'	Si4	O2b
N3	Si4	O1d
F	Si4	O4c

rather local quantity which is mainly affected by a correct position of the copper atom rather than the outer regions of the cavities. Nachtigall *et al.* [105] also discussed the effect of the opposite zeolite channel wall on the CO stretching frequency in ZSM-5 zeolites. The effect becomes non negligible once the CO–wall distance is less than 6 Å. However, the large supercage in Y zeolites leads to distances of about 6 and 9 Å (for sites III and II, respectively) and thus this effect must be considered rather small.

TABLE 4.4: Comparison between 12T and 6T QM cluster models at site II of Cu–Y zeolite: relative stabilities (E_{rel}) of different complexes (with/without adsorbate) and binding energies (E_b) of O_2 . The results in the first line refer to the case of 1 Al-complexes, the others to the various isomers containing 2 Al atoms. Isomers (cf. Table 4.3) A, B, C, D, E, E', F contain the H atom on 6T ring O atom (of 12T and 6T clusters), whereas the additional H atom of isomers N1, N2, N3 is positioned at the 4T ring O atom of 12T cluster. For the numbering of the atoms see Fig. 4.3. All the quantities are given in kcal mol⁻¹.

Isomers	12T cluster			6T cluster		
	E_{rel}^a	E_b	E_{rel}^b	E_{rel}^a	E_b	E_{rel}^b
1 Al	–	-10.5	–	–	-10.9	–
A	23.2	-12.0	25.2	23.8	-9.1	22.2
N1	0.9	-10.2	1.0			
B	7.1	-12.1	9.0	2.1	-12.9	4.4
C	4.5	-13.0	7.4	0.0	-14.9	4.3
N2	0.3	-9.8	0.0			
D	22.0	-17.3	29.2	17.5	-18.1	25.0
E	24.3	-24.7	38.9	18.9	-19.7	27.9
E'	22.1	-26.9	38.9	16.1	-22.1	27.9
N3	0.0	-12.0	1.9			
F	4.3	-8.3	2.5	0.8	-9.8	0.0

^a for O_2 adsorption complexes; ^b for bare complexes

TABLE 4.5: Site III: labeling of Cu–Y zeolite model complexes (with/without adsorbates) according to the replacement of a Si atom by a second Al atom and the position of the additional H atom sitting on a zeolite framework oxygen atom. For the numbering of the atoms see Fig. 4.4/10T cluster.

Isomers	2 nd Al atom replaces	H atom is connected to
A	Si2	O1a
B	Si2	O2a
C	Si3	O2a
D	Si3	O1b
E	Si4	O1b
F	Si4	O3a
G	Si4	O4b
H	Si6	O1c
I	Si6	O2b
J	Si8	O3c
K	Si8	O1e

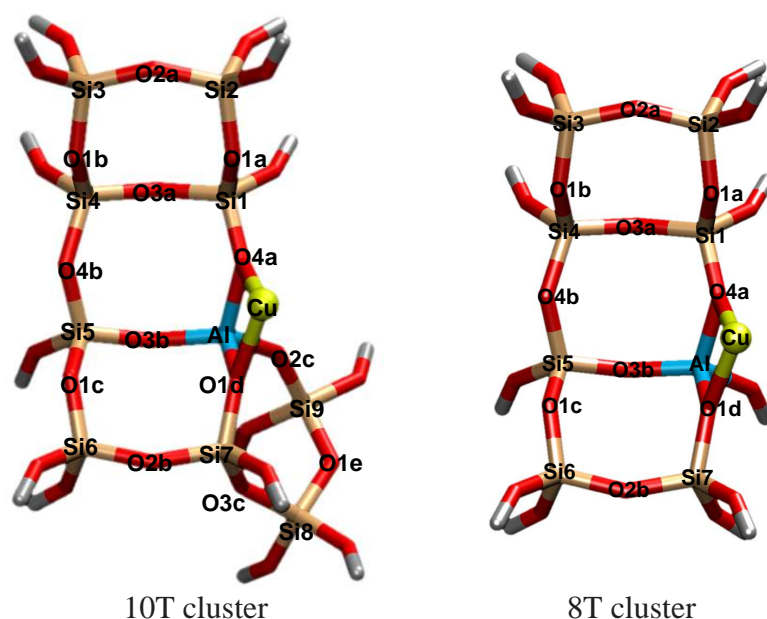


FIGURE 4.4: Quantum mechanically treated zeolite fragment (10T cluster and 8T cluster with 1 Al) without adsorbate at cationic site III. The second Al atom replaces any of the Si atoms except the neighbouring ones.

TABLE 4.6: Comparison between 10T and 8T QM cluster models at site III of Cu–Y zeolite: relative stabilities (E_{rel}) of different complexes (with/without adsorbate) and binding energies (E_b) of O_2 . The results in the first line refer to the case of 1 Al-complexes, the others to the various isomers (cf. Table 4.5) containing 2 Al atoms. For the numbering of the atoms see Fig. 4.4. All the quantities are given in kcal mol⁻¹.

Isomers	10T cluster			8T cluster		
	E_{rel}^a	E_b	E_{rel}^b	E_{rel}^a	E_b	E_{rel}^b
1 Al	–	-28.3	–	–	-28.6	–
A	13.3	-28.7	13.2	13.6	-29.0	13.3
B	0.9	-28.6	0.8	1.0	-28.9	0.6
C	1.2	-29.1	1.5	1.1	-29.5	1.3
D	7.5	-27.7	6.4	7.5	-27.9	6.2
E	7.1	-29.1	7.4	6.6	-29.5	6.9
F	31.1	-28.1	30.4	30.2	-28.4	29.4
G	10.8	-28.4	10.5	10.3	-28.7	9.8
H	0.0	-28.8	0.0	0.0	-29.3	0.0
I	3.4	-27.6	2.3	4.9	-27.8	3.4
J	21.6	-27.3	20.2			
K	0.7	-28.5	0.4			

^a for O_2 adsorption complexes; ^b for bare complexes

4.5 Verification of DFT Results by MRCI Calculations

To evaluate the ability of the chosen BP86 functional for correctly representing and predicting the electronic and structural properties of CuO_2 moieties, high-level *ab initio* calculations have been performed on a simple CuO_2^+ model system. Comparative studies on the geometrical parameters of this benchmark system have also been performed by other authors [106–108]. However, in some of the work, the geometry of the CuO_2^+ triplet was not fully optimized, or only a limited set of methods was invoked for the comparison. Thus, these calculations were extended to fully optimized geometries and other state-of-the-art methods. The *ab initio* calculations performed here are of the single-reference coupled-cluster type, with single and double substitutions and a perturbative account of triples CCSD(T) [109, 110] and of the multi-reference configuration-interaction type with single and double substitutions and a Davidson correction for the effect of higher substitutions MRCISD+Q [111, 112]. While the former method is size-consistent and should give a reliable account of the geometrical parameters of the triplet state, as well as of its binding energy with respect to $\text{Cu}^+ + \text{O}_2$, the latter method is well suited to describe the multi-reference character of the singlet state, and should give a reliable account of singlet-triplet splittings.

TABLE 4.7: DFT/BP86 and *ab initio* CCSD(T) and MRCISD+Q results for geometrical parameters, binding energies E_b with respect to $\text{Cu}^+ + \text{O}_2$, and singlet-triplet splittings ΔE_{S-T} of the CuO_2^+ complex. Numbers in parentheses are symmetry-broken results in the DFT case; they denote a second minimum in the MRCISD+Q case. Basis sets are aug-cc-pVTZ and cc-pVTZ-PP for O and Cu, respectively.

	BP86, RKS (UKS)		CCSD(T)	MRCISD+Q	
	singlet	triplet	triplet	singlet	triplet
$R(\text{O1}-\text{O2}) [\text{Å}]$	1.226 (1.235)	1.235 (1.235)	1.208	1.223 (1.228)	1.215
$R(\text{Cu}-\text{O1}) [\text{Å}]$	1.864 (1.861)	1.867 (1.869)	2.024	2.076 (2.057)	2.073
$\angle \text{Cu}-\text{O1}-\text{O2}$	123.6 (124.8)	124.6 (124.6)	130.7	130.0 (118.8)	130.4
E_b/eV	-0.06 (-0.66)	-0.98 (-0.97)	-0.51	–	-0.36
$\Delta E_{S-T}/\text{eV}$	0.92 (0.31)	–	–	0.99 (0.98)	–

The results listed in Table 4.7 refer to calculations with triple-zeta quality basis sets throughout: for O, Dunning’s aug-cc-pVTZ basis set [113] is used, while for Cu the ECP10MDF pseudopotential and corresponding cc-pVTZ-PP basis set mentioned in Section 4.1 are applied. The orbitals for the MRCI calculations are taken from a

full-valence complete-active-space self-consistent-field (CASSCF) calculation, with a O $2sp$ /Cu $3d$ active space. The full set of valence electrons in the O $2sp$ /Cu $3d$ orbitals has been correlated in the CCSD(T) and MRCI calculations.

For the triplet state, differences between spin-restricted Kohn-Sham (RKS) calculations and spin-unrestricted ones (UKS) are negligible. Comparison with the CCSD(T) results shows that the Cu–O bond length is substantially underestimated by DFT with the BP86 functional (by 0.15 Å), while a slight overestimation is found for the O–O distance (by 0.03 Å). Also, DFT predicts a too small \angle Cu–O–O angle (by 6°). The underestimation of the r (Cu–O) bond length with DFT is in line with a too large binding energy with respect to the separation into $\text{Cu}^+ + \text{O}_2$; the CCSD(T) value is smaller by nearly a factor of 2 (*i.e.* by 0.5 eV). On the other hand, the agreement between the two *ab initio* methods, CCSD(T) and MRCI, is satisfactory. The approximate treatment of higher substitutions (and especially the neglect of connected triples) leads to slightly larger bond lengths (by 0.05 Å for r (Cu–O)) in the latter scheme. Also, the binding energy becomes slightly smaller in MRCI, when evaluated with respect to isolated fragments, due to size-consistency errors. Note that the difference between DFT and CCSD(T) becomes significantly smaller with a hybrid functional (B3LYP); in that case the binding energy differs by only 0.2 eV, bond lengths by less than 0.06 Å, and bond angles by less than 1° from the CCSD(T) value. However, due to the increased computational demands of such functionals, their application to the large clusters (selected cases) used in this study was computationally expensive and thus BP86 calculations are presented throughout.

Turning now to the discussion of the singlet state, larger differences are seen between RKS and UKS results than for the triplet case, but still a quite similar end-on geometry is obtained in both cases (which is also quite similar to the triplet one). However, the binding energy with respect to $\text{Cu}^+ + \text{O}_2$ is different for RKS and UKS, indicating the heavy admixture of triplet to singlet in the symmetry-broken UKS solution. In the MRCI case, two nearly degenerate singlet states of different spatial symmetry are obtained. The first one has nearly the same geometry as the MRCI triplet one, while in the second one the \angle Cu–O–O is reduced by around 10°. Still, the differences for the Cu–O bond lengths of the two spin states are smaller, both in the MRCI case as well as in the DFT one, than the difference for a given spin state between the two methods. On the other hand, the singlet-triplet energy difference is similar between the MRCI calculations and the spin-restricted DFT/BP86 ones, with values between 0.9 and 1.0 eV. The significantly smaller S-T splitting of 0.3 eV for the UKS solution with respect

to the RKS one is most probably due, to the major part, to the singlet-triplet mixing in the symmetry-broken UKS singlet state.

Summarizing the results so far, an overall good agreement between the DFT results and more accurate *ab initio* CCSD(T), MRCI ones are obtained, which supports the use of the chosen DFT treatment. Also, since the triplet state comes out to be lower in energy than the lowest singlet ones, subsequent DFT calculations are restricted to the triplet state only. The latter statement is based, of course, on the assumption that electronic effects of the zeolite on the Cu atom do not change this order. To corroborate this assumption, some additional calculations are performed. A comparison is made between the energies of the triplet and broken-symmetry singlet states, in their respective equilibrium structures determined in DFT/MM calculations with the TZVP basis set, for O₂ adsorption on Cu zeolites with one Al atom. For adsorption at site II comprising only 6 T atoms, the singlet-triplet separation is 0.23 eV; the corresponding value for site III is 0.14 eV. These values are lower than the singlet-triplet splitting of the CuO₂⁺ model system, by up to a factor of 2, but the triplet is still lowest in energy. MRCISD+Q calculations for zeolites are very time consuming, and some approximations are introduced, therefore. A smaller SVP basis set is used and the calculations are restricted to the singlet-triplet splitting at the fixed DFT/MM triplet equilibrium geometries. In the Pipek-Mezey localization, all the localized orbitals were fixed with the exception of the Cu 3*d*-like orbitals and the valence orbitals of the adsorbed O₂ molecule. The localization was performed starting with the DFT wavefunction. The latter orbital sets were then re-optimized in CASSCF calculations with a small active space of 2 orbitals (the O–O π* ones). The localized Cu and O₂ orbitals were finally correlated at the MRCISD+Q level. At this level of approximation, singlet-triplet splittings of 0.06 eV and 0.14 eV are obtained for II (with 6T QM model cluster) and for III, respectively. This is in reasonable agreement with the DFT results discussed above.

Chapter 5

Single Adsorption

5.1 Adsorption of Dioxygen

5.1.1 Local Structure of Bare Cu(I) Ion Sites

Site II: Table 5.1 shows structural parameters for the Y zeolite model containing a Cu(I)¹ cation at site II (cf. Fig. 4.1). The maximum coordination radius for Cu to framework oxygens (Cu–O) is taken to be 2.5 Å. All of the Cu–Y zeolites (containing 1 or 2 Al atoms) show a Cu⁺ ion with three coordinated O2 type framework oxygen atoms except isomers A, D and E. Cu(I) in isomer D is 3-fold coordinated, two of the oxygens are of O2 type while the other is an O4 type oxygen. In this isomer an additional H atom is located at an O2 type O atom, which more or less forms a linear bond ($\angle \text{O2b-H-Cu} = 162.7^\circ$) with the Cu center in the 6-ring of the sodalite cage. Isomer E has a two-fold coordinated Cu center – one framework oxygen is of O2 type, and another one is of O4 type. Isomer A shows also a two-fold coordination of the Cu atom, but both the framework oxygens are solely of O2 type.

A three-fold coordination of the Cu(I) center in Y zeolite nicely agrees with the computational results of Rejmak et al. [103] and Jardillier et al. [104]. However, due to bonding to the Cu atom, the framework O2 type oxygens of site II move towards the plane of the 6-rings, so that the Cu atom, the T (Si/Al) atoms, as well as the O2 atoms are practically within the same plane. Again, this finding is similar to that of Sierka,

¹See Appendix D to compare the results of Cu(I) containing Y zeolite with Cu(II).

TABLE 5.1: Cu–O coordination at bare site II in Y zeolite (12T QM cluster): Cu–O bond distances (Å) to the nearest-neighbour O atoms, and the crystallographic positions of the coordinated O atoms; for the numbering of the atoms see Fig. 5.1.

Isomers	2^{nd} Al atom replaces	H atom is connected to	R_{Cu-O}
1 Al	–	–	O2(2.010, 2.226, 1.948)
A	Si2	O2a	O2 (1.935, 1.893)
N1	Si2	O1b	O2 (1.983, 2.223, 1.961)
B	Si2	O4b	O2 (1.905, 2.499, 1.898)
C	Si3	O4b	O2 (2.115, 2.018, 1.984)
N2	Si3	O1c	O2 (2.039, 2.125, 1.992)
D	Si3	O2b	O2 (1.921, 1.872); O4(2.319)
E	Si4	O2b	O2 (2.009); O4 (2.043)
N3	Si4	O1d	O2 (2.128, 2.071, 1.953)
F	Si4	O4c	O2 (2.081, 2.024, 2.000)

TABLE 5.2: Cu–O coordination at bare site III in Y zeolite (8T QM cluster): Cu–O bond distances (Å) to the nearest-neighbour O atoms, and the crystallographic positions of the coordinated O atoms; for the numbering of the atoms see Fig. 5.2.

Isomers	2^{nd} Al atom replaces	H atom is connected to	R_{Cu-O}
1 Al	–	–	O1 (1.982); O4 (2.035)
A	Si2	O1a	O1 (1.947); O4 (2.095)
B	Si2	O2a	O1 (2.000); O4 (2.023)
C	Si3	O2a	O1 (1.984); O4 (2.034)
D	Si3	O1b	O1 (1.975); O4 (2.054)
E	Si4	O1b	O1 (1.989); O4 (2.026)
F	Si4	O3a	O1 (1.976); O4 (2.067)
G	Si4	O4b	O1 (2.018); O4 (2.009)
H	Si6	O1c	O1 (1.965); O4 (2.067)
I	Si6	O2b	O1 (2.024); O4 (2.013)

Sauer and co-workers [103] who observed that *in all cases equilibrium Cu(I) ion positions are found almost exactly in the plane of the 6T rings*. Isomer E shows a different topology around the Cu center as compared to other ones. In this isomer, the additional proton located at O2b forms a H-bond ($R_{(O..H)} = 2.644$ Å and $\angle O2b-H-O2a = 146.4^\circ$) with the O2a framework atom. As a result the Cu atom tries to move out of the plane of T atoms of the 6-ring. In all other Cu–complexes at site II, the Cu atom tends to move slightly below the plane of the 6-ring, *i.e.* into the sodalite cage, due to

the presence of the additional proton. Cu–O bond distances lie in the range of 1.9–2.3 Å for all Cu–complexes at site II. Finally regarding site II, in Cu–complexes where a proton is located at the O2 type oxygen, Cu to zeolitic oxygen coordination is lowered from 3 to 2.

Site III: For site III (see Table 5.2), two-fold coordination is favored. Introduction of the second Al atom into the unit cell, hardly brings about any change for the immediate surroundings of the Cu atom at site III. In all these structures, the Cu(I) ion is bound to O1 and O4 type crystallographic oxygens (at the edge of the hexagonal prism) which are lying above the plane of the T atoms and the Cu atom is well above (cf. Fig. 4.2) the planes of the 4-rings. The Cu–O bond lengths vary between 1.9 and 2.0 Å, which are in the same range as for the CuO_2^+ model complex discussed in Section 4.5.

5.1.2 Cu(I) Binding Energies

The Cu(I) binding energy is defined as the energy of the reaction scheme below:

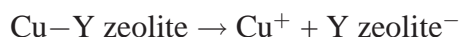


Table 5.3 shows the Cu(I) binding energies for site II. While the additional proton is located at an O2 type oxygen atom, much weaker binding energies are obtained than the other ones. Binding energies of Cu(I) in energetically low-lying isomers (B, C, F) of site II vary in the range between ~ -146 and ~ -152 kcal mol⁻¹. For site III, Cu(I) is found to be more weakly bound than at site II, within the range between ~ -132 and ~ -142 kcal mol⁻¹ (see Table 5.4).

A comparison of the relative stability of various isomers arising from the introduction of a 2nd Al atom in the bare site II and III clusters, without adsorbed O₂, is discussed in the following section.

1. For site II (Table 4.4, 12T cluster), the most stable isomers without adsorbed dioxygen are those where the additional proton is located in an adjacent 4-ring (connected to an O1 type oxygen), in particular, isomers N1 and N2 differ by just 1 kcal mol⁻¹. Once the proton is bonded to an O4 type oxygen and thus resides in the inner 6T ring, the energy rises by several kcal mol⁻¹. The most unfavorable isomers are obviously those where an additional proton is bonded to an O2 type oxygen.

2. For site III (Table 4.6, 8T cluster), the most stable bare cluster with 2 Al atoms is that where the second Al atom is as close as possible to the first one (which is separated by only one Si atom) and the additional proton is located at an O1 type atom. However, there are quite a number of other isomers nearly degenerate in energy with the latter one.

TABLE 5.3: Relative energies (E_{rel}) and binding energies (E_b) of Cu^+ in bare (without adsorbate) Cu–Y zeolites (6T QM cluster) with different Al contents (1 Al, and 2 Al atoms) and H distribution at site II; the result in the first line refers to the case of 1 Al-complex, and the others to the various isomers containing 2 Al atoms. For the numbering of the atoms see Fig. 5.1. All the quantities are given in kcal mol^{-1} .

Isomers	2 nd Al atom replaces	H atom is connected to	E_{rel}	E_b
1 Al	–	–	–	-148.5
A	Si2	O2a	22.2	-130.4
B	Si2	O4b	4.4	-151.9
C	Si3	O4b	4.3	-147.9
D	Si3	O2b	25.0	-133.2
E	Si4	O2b	27.9	-136.3
F	Si4	O4c	0.0	-146.1

TABLE 5.4: Relative energies (E_{rel}) and binding energies (E_b) of Cu^+ in bare (without adsorbate) Cu–Y zeolites (8T QM cluster) with different Al contents (1 Al, and 2 Al atoms) and H distribution at site III; the result in the first line refers to the case of 1 Al-complex, and the others to the various isomers containing 2 Al atoms. For the numbering of the atoms see Fig. 5.2. All the quantities are given in kcal mol^{-1} .

Isomers	2 nd Al atom replaces	H atom is connected to	E_{rel}	E_b
1 Al	–	–	–	-141.0
A	Si2	O1a	13.3	-128.0
B	Si2	O2a	0.6	-141.8
C	Si3	O2a	1.3	-137.5
D	Si3	O1b	6.2	-138.0
E	Si4	O1b	6.9	-143.9
F	Si4	O3a	29.4	-134.2
G	Si4	O4b	9.8	-139.7
H	Si6	O1c	0.0	-140.3
I	Si6	O2b	3.4	-132.3

Relative energies of the isomers are classified into three categories as follows:

- (i) within 1 kcal mol⁻¹
- (ii) from ~ 3.0 to ~ 7.0 kcal mol⁻¹
- (iii) from ~ 10.0 to ~ 29.0 kcal mol⁻¹

Cu(I) binding energies in bare faujasites (without adsorbate) have very recently been studied by Sierka, Sauer and co-workers who used an approach very similar to the present work. As discussed in Ref. [103] Cu⁺ at site II is significantly more stable than at site III, which is also confirmed in the present study.

5.1.3 Geometries

The structural changes associated with the adsorption of O₂ onto Cu-containing zeolites are discussed here. The present results refer to the triplet state of the complex which correlates with the ³Σ_g⁻ ground state of O₂ and the closed-shell zeolite upon dissociation.

1 Al atom containing complexes: In case of 1 Al atom per unit cell, adsorption leads to an elongation of the O₂ bond, from 1.22 Å for free O₂ (the experimental value is 1.208 Å) to 1.27 Å for O₂ adsorbed at site II of zeolite, and to 1.32 Å for adsorption at site III. Thus, activation of O₂ is larger at site III, which is consistent with a larger binding energy at this site (cf. Section 5.1.5). There is another important difference between the two adsorption sites: O₂ adsorbs end-on at site II (see Table 5.5), with very different Cu–O' (O'') bond distances (1.82 and 2.75 Å), while adsorption at site III can be characterized as side-on, with quite similar Cu–O' (O'') bond distances of 1.94 and 1.97 Å, see Table 5.6.

In contrast to the adsorption of CO to Cu–faujasites [103], the angle between the copper atom and dioxygen (∠ Cu–O'–O'' = 124.6° at site II) deviates significantly from linearity. The average Cu–O bond distance seen experimentally from EXAFS measurements is 1.95 ± 0.02 Å [114] which is in excellent agreement with the calculated values for site III Cu–complexes. However, the averaging also includes the oxygen atoms of the zeolite framework. Within the calculations for sites II and III, there are Cu–O distances with respect to framework oxygens which are in the same range and therefore it is hardly possible to judge about the preferred adsorption site on the basis of the Cu–O distances.

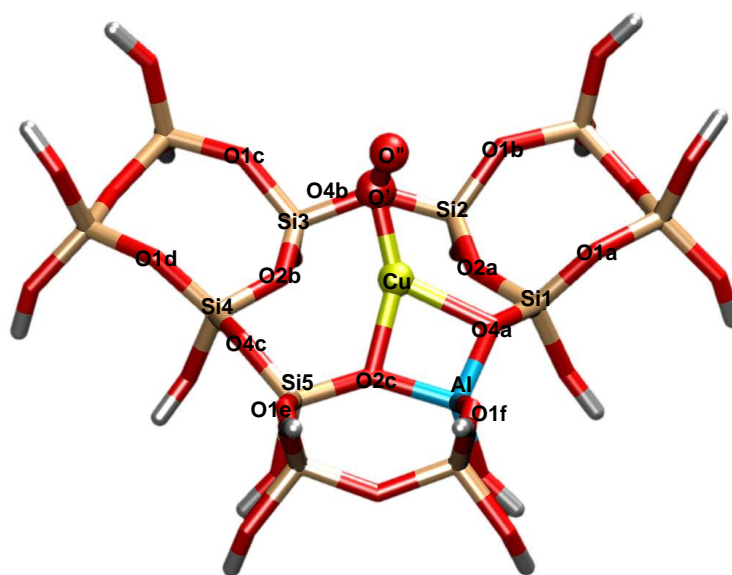


FIGURE 5.1: Quantum mechanically treated zeolite fragment (12T model) with adsorbed O₂ at cationic site II, for the case of the 1 Al-complex.

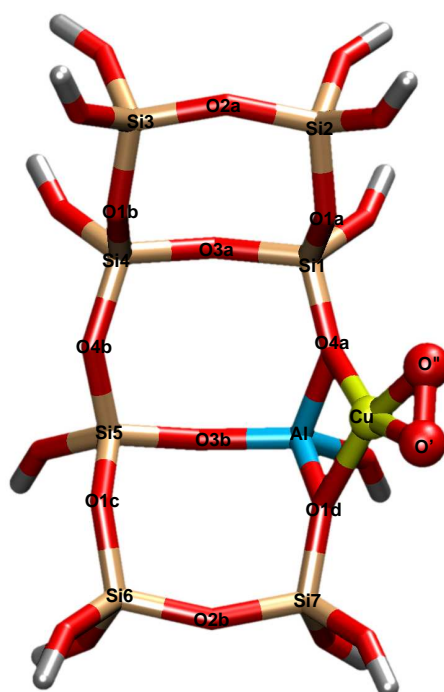


FIGURE 5.2: Quantum mechanically treated zeolite fragment (8T model) with adsorbed O₂ at cationic site III, for the case of the 1 Al-complex.

TABLE 5.5: O₂ adsorption onto Cu(I) at site II in Y zeolites (12T QM cluster): Cu–O, Cu–O', Cu–O'', and O'–O'' bond distances in Å, ∠Cu–O'–O''(°), and binding mode of O₂. For the numbering of the atoms see Fig. 5.1.

Isomers	2 nd Al atom replaces	H atom is connected to	R _{Cu–O}	R _{Cu–O'}	R _{Cu–O''}	R _{O'–O''}	∠Cu–O'–O''	Mode of binding
1 Al	–	–	O2 (1.996), O4(2.103)	1.824	2.750	1.268	124.6	end-on
A	Si2	O2a	O2 (2.171, 2.027); O4 (2.233)	1.923	2.768	1.278	118.3	end-on
N1	Si2	O1b	O2 (2.103, 2.477, 1.998)	1.882	2.792	1.270	123.6	end-on
B	Si2	O4b	O2 (2.186, 2.079); O4 (2.106)	1.851	2.668	1.284	115.4	end-on
C	Si3	O4b	O2 (2.244, 1.969); O4 (2.335)	1.880	2.648	1.284	112.2	end-on
N2	Si3	O1c	O2 (2.283, 2.312, 2.013)	1.883	2.765	1.270	121.3	end-on
D	Si3	O2b	O2 (2.103); O4 (1.954)	1.915	2.011	1.311	74.5	side-on
E	Si4	O2b	O2 (1.955); O4 (2.108)	1.818	2.773	1.268	127.1	end-on
E'	Si4	O2b	O2 (2.007); O4 (1.999)	1.956	1.960	1.316	62.1	side-on
N3	Si4	O1d	O2 (1.986); O4 (2.032)	1.977	1.950	1.317	69.3	side-on
F	Si4	O4c	O2 (2.204, 2.168, 2.096)	1.909	2.783	1.267	121.0	end-on

Compared to the bare zeolite, O₂ adsorption induces significant changes in the geometry around the Cu(I) center at site II. For site II adsorption, Cu moves out of the plane of the T atoms towards the supercage and comes closer to the nearest-neighbor Al atom, by 0.18 Å. Also, the distance of Cu to the nearest-neighbor O atoms connected to the Al atom in the ring becomes smaller so that these atoms (which are O2 and O4 type framework oxygens) become the atoms to which the Cu atom is coordinated, rather than the O2 atoms solely as in the case of the adsorbate-free zeolite. This amounts to a change from a three-fold coordinated to a two-fold coordinated Cu atom which has also been found by Sierka, Sauer and co-workers [103] for the adsorption of CO. For site III, changes within the zeolite upon adsorption are, rather surprisingly, much smaller, and the coordination number does not change. The distance of Cu to the nearest-neighbor Al atom in the ring becomes slightly larger, by 0.06 Å, while the coordination to the two O1 and O4 type oxygen atoms of the ring (above the plane of the T atoms) becomes stronger, with a decrease of the Cu–O bond distances by ~ 0.02 Å. The optimized structures for the two adsorption sites are shown in Figs. 5.1 and 5.2.

2 Al atom containing complexes: For site II, the bond length of the adsorbed O₂ varies among all 9 adsorption complexes from 1.27 to 1.32 Å. Consequently, there are significant changes of the O₂ binding energy between the different isomers (cf. Table 5.8). Also, different isomers show different modes of O₂ to Cu binding patterns: there is still end-on bonding in most cases, but there are also isomers which bind side-on.

Moreover, in isomer A with end-on bonding, a non-linear hydrogen-bond ($R_{(O..H)} = 1.754$ Å and $\angle O'' \dots H-O2a = 160^\circ$) is formed between one of the O atoms of the adsorbed dioxygen to the additional proton attached to one of the ring O atoms (cf. Fig. 5.3).

In all cases, the Cu atom moves out of the plane of T atoms of the 6-ring towards the supercage (as it does with 1 Al per unit cell), but there is considerable flexibility with respect to coordination of the Cu atoms to the O atoms of the ring: for several of the isomers a two-fold coordination to one O2 type and one O4 type atoms appears (as for the case with 1 Al atom), but there are also isomers with three-fold coordination to O2 type atoms only, and in some cases even the 3-fold coordination to two O2 type and one O4 type 6-ring oxygens atoms is observed. Displacements toward the supercage were also observed experimentally for the adsorption of CO and confirmed by corresponding cluster calculations [74, 115].



FIGURE 5.3: Quantum mechanically treated zeolite fragment (12T model) with adsorbed O_2 at cationic site II, showing an internal hydrogen-bond.

Again, the situation at adsorption site III is much more clear-cut: O_2 bonding is side-on for all isomers resulting from the introduction of a second Al atom. O_2 bond lengths of the adsorbed species vary only slightly between 1.31 and 1.32 Å. Cu–Al nearest-neighbor bond distances are virtually unchanged as compared to the calculations with 1 Al atom, and the two-fold coordination of Cu to the 2 next-neighboring O ring atoms is retained. The optimized structures for the energetically lowest isomers of the two adsorption sites are shown in Figs. 5.4 and 5.5.

The Cu–O' bond distances with respect to the isomers of site II are systematically shorter than for the site III isomers, (the average Cu–O' distance for the site III is 1.956 Å while it is 1.895 Å for site II). Again, the value for site III is in better agreement with the experimental value of 1.95 Å [114]. Besides the better agreement between the experimental and computed values for site III, a shoulder at about 1.895 Å (corresponding to the average value of the site II) cannot be seen in the radial distribution function obtained from the EXAFS experiment [114].

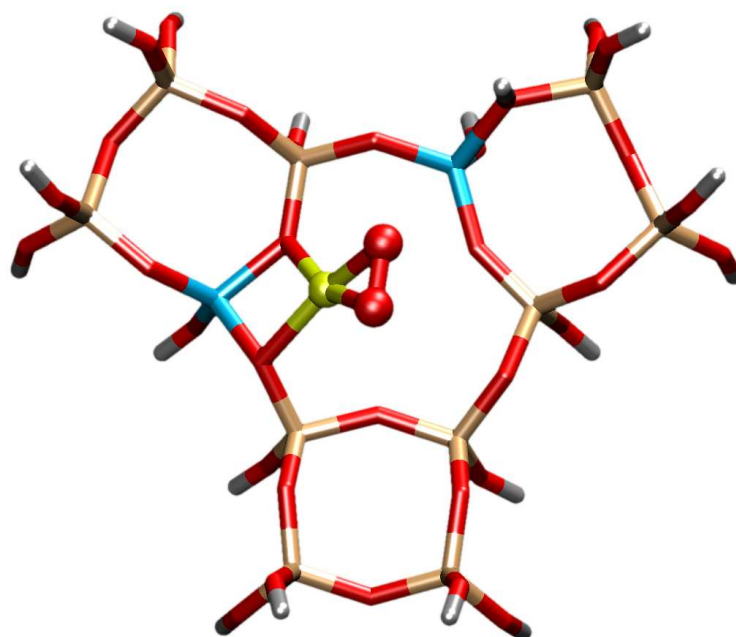


FIGURE 5.4: The most stable O_2 adsorption complex (N3) at site II. Charge neutrality is conserved by additional proton (Brønsted acid site) at O1d.

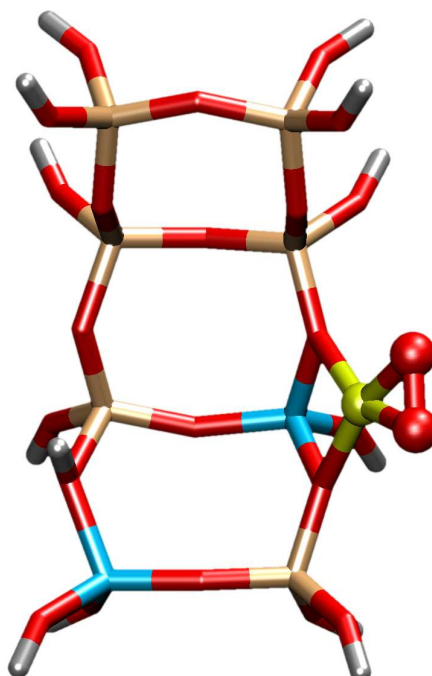


FIGURE 5.5: The most stable O_2 adsorption complex (H) at site III. Charge neutrality is conserved by additional proton (Brønsted acid site) at O1c.

TABLE 5.6: O₂ adsorption onto Cu(I) at site III in Y zeolites (8T QM cluster): Cu–O, Cu–O', Cu–O'', and O'–O'' bond distances in Å, ∠Cu–O'–O''(°), and binding mode of O₂. For the numbering of the atoms see Fig. 5.2.

Isomers	2 nd Al atom replaces	H atom is connected to	R _{Cu–O}	R _{Cu–O'}	R _{Cu–O''}	R _{O'–O''}	∠Cu–O'–O''	Mode of binding
1 Al	–	–	O1 (1.968); O4 (2.019)	1.971	1.940	1.318	69.0	side-on
A	Si2	O1a	O1 (1.922); O4 (2.076)	1.998	1.916	1.319	67.0	side-on
B	Si2	O2a	O1 (1.984); O4 (2.003)	1.957	1.953	1.320	70.1	side-on
C	Si3	O2a	O1 (1.965); O4 (2.022)	1.974	1.938	1.319	68.8	side-on
D	Si3	O1b	O1 (1.965); O4 (2.033)	1.973	1.937	1.317	68.8	side-on
E	Si4	O1b	O1 (1.974); O4 (2.010)	1.966	1.945	1.320	69.4	side-on
F	Si4	O3a	O1 (1.957); O4 (2.055)	1.987	1.926	1.317	67.8	side-on
G	Si4	O4b	O1 (2.003); O4 (1.989)	1.946	1.964	1.319	71.0	side-on
H	Si6	O1c	O1 (1.949); O4 (2.045)	1.992	1.923	1.319	67.5	side-on
I	Si6	O2b	O1 (1.992); O4 (2.021)	1.946	1.969	1.317	71.3	side-on

5.1.4 Charges

For the equilibrium structures of the Cu-containing zeolite models with 1 Al atom, a population analysis using the natural orbital scheme of Reed and Weinhold [116] as implemented in TURBOMOLE has been performed.

TABLE 5.7: Population analysis results for site II and III, bare Cu and O₂ adsorption complexes containing 1 Al atom.

Adsorption site	Atom	Charges	Orbital	Population	Spin density
Bare-complex					
II	Cu	0.85	4s	0.25	
			3d	9.89	
III	Cu	0.89	4s	0.17	
			3d	9.92	
O ₂ -complex					
II	Cu	1.10	4s	0.28	0.35
			3d	9.61	
	O'	-0.24	2s	1.81	0.62
			2p	4.43	
O''	-0.04	2s	1.84	0.88	
		2p	4.19		
III	Cu	1.20	4s	0.27	0.53
			3d	9.51	
	O'	-0.20	2s	1.86	0.72
			2p	4.33	
	O''	-0.20	2s	1.86	0.70
			2p	4.34	

Without O₂ adsorption, the Cu(I) ion carries a charge of less than 1, *i.e.*, 0.85 for site II and 0.89 for site III (cf. 5.7). In both cases, there is a 3*d* hole of about 0.1 and a 4*s* occupation of about 0.2. There is a notable change upon O₂ adsorption: the adsorbed O₂ withdraws a fractional electronic charge of 0.25 \cdots 0.3 from the Cu atom, so that the charge of the latter becomes 1.10 and 1.20 for sites II and III, respectively. Interestingly, the 4*s* occupation is practically unchanged (site II) or even increases by 0.1 (site III), while the 3*d* hole enlarges to 0.4 (0.5) for site II (site III). Since the adsorbed O₂ is in a triplet state, the Cu 3*d* hole becomes spin-polarized, and the Cu 3*d* spin density is essentially identical with the hole charge (0.35 for site II, 0.53 for site III). The charge distribution on the adsorbed O₂ is almost symmetrical for the site III side-on adsorption

(-0.20 per atom) while it is rather unsymmetrical for the site II end-on adsorption (-0.24 and -0.04). The total negative charge acquired by O_2 upon adsorption is higher for site III than for site II, in accordance with the stronger binding in the former case. Of course, the spin density on O_2 becomes smaller upon adsorption, *i.e.*, it is reduced from $+1$ to values between 0.9 and 0.6 , due to the spill-out of spin-density towards the Cu $3d$ shell.

The zeolite oxygens are more negatively charged than the adsorbed O_2 , with charges between -1.1 and -1.4 . The highest negative charge appears for the O2-type oxygens which are directly coordinated to Cu. The negative charges of the oxygens are compensated by positive charges of about 2.4 for Si and about 2.1 for Al atoms. See Appendices C.1 and C.2 for charges on Cu and O_2 in all the isomers without and with O_2 adsorption at sites II and III.

5.1.5 Energies

Relative energies of dioxygen adsorption complexes of site II: There are two categories of adsorption complexes concerning the position of the additional proton, *i.e.*, whether H^+ is attached to the framework oxygen of the 6-ring or the 4-ring of the 12T cluster model which is chosen to be the QM part of the QM/MM calculations. To the first category belong the complexes where the proton can be located either at the O4 type or at the O2 type oxygen of the 6-ring. The complexes where the proton resides at the O2 type oxygen are higher in energy than the complexes containing a proton at an O4 type oxygen. To the second category belong the complexes where H^+ is attached to the O1 framework oxygen of the 4-ring. This 4-ring is the immediate neighbor of the 6-ring. It may be one of the reasons that there is not much repulsion between two positive centers, *i.e.*, H^+ and Cu^+ . Therefore these complexes are the most stable ones. As a consequence, there are three regions of relative energies among all the O_2 adsorption complexes:

- (i) ~ 22.0 to ~ 23.0 kcal mol $^{-1}$: proton at O2 type oxygen atoms of the 6-ring
- (ii) ~ 4.0 to ~ 7.0 kcal mol $^{-1}$: proton at O4 type oxygen atoms of the 6-ring
- (iii) within 1 kcal mol $^{-1}$: proton at O1 type oxygen atoms of the 4-ring

Adsorption energies of dioxygen adsorption complexes of site II: Now, coming to the adsorption energies of O_2 in the adsorption complexes, some simple relations between the above discussed classification of relative energies of the different complexes, and

TABLE 5.8: O₂ adsorbed at site II in Cu–Y zeolites (12T QM cluster model): relative stabilities (E_{rel}) of different adsorption complexes, and binding energies (E_b) of O₂. The result in the first line refers to the case of 1 Al–complex, and the others to the various isomers containing 2 Al atoms. For the numbering of the atoms see Fig. 5.1. All the quantities are given in kcal mol⁻¹.

Isomers	2 nd Al atom replaces	H atom is connected to	E_{rel}	E_b
1 Al	–	–	–	-10.5
A	Si2	O2a	23.2	-12.0
N1	Si2	O1b	0.9	-10.2
B	Si2	O4b	7.1	-12.1
C	Si3	O4b	4.5	-13.0
N2	Si3	O1c	0.3	-9.8
D	Si3	O2b	22.0	-17.3
E	Si4	O2b	24.3	-24.7
E'	Si4	O2b	22.1	-26.9
N3	Si4	O1d	0.0	-12.0
F	Si4	O4c	4.3	-8.3

their coordination number around the Cu center, and its corresponding effects on the adsorption energies of O₂ can be provided. First of all, Table 5.8 shows that there are two regions of adsorption energies of O₂ – one between ~ -8.0 and ~ -13.0 kcal mol⁻¹, and the other one between ~ -17.0 and ~ -27.0 kcal mol⁻¹. The first classified region of adsorption energies of O₂ corresponds to regions (ii) and (iii) (see above) and they lie at the lower end of the relative energies. These are the ones which show a three-fold coordinated Cu center concerning the framework oxygens (Table 5.5), thus the O₂ binding weakens, resulting in lower adsorption energies. The second category of the adsorption energies of O₂ is at the higher end of the relative energies, *i.e.*, region (i). These complexes show a two-fold coordinated Cu center with respect to the framework oxygens (Table 5.5), implying better binding to O₂ which is reflected in their adsorption energy values.

In spite of all these facts, there are two isomers (A and N3) showing different behavior than the others discussed in the previous paragraph. Isomer A shows a Cu(I) center with three-fold coordination, and the additional proton is located at an O2 type oxygen. Both these facts are reflected truly in the O₂ adsorption energy, and relative energy respectively. Introduction of an additional proton at an O2 type oxygen should have enforced a two-fold coordinated Cu complex, but it was not the fact. Possibly, the topology of the H-bonding between one of the oxygens of O₂ and the proton (see Fig. 5.3) caused

TABLE 5.9: O₂ adsorbed at site III in Cu–Y zeolites (8T QM cluster model): relative stabilities (E_{rel}) of different adsorption complexes, and binding energies (E_b) of O₂. The result in the first line refers to the case of 1 Al–complex, and the others to the various isomers containing 2 Al atoms. For the numbering of the atoms see Fig. 5.1. All the quantities are given in kcal mol⁻¹.

Isomers	2 nd Al atom replaces	H atom is connected to	E_{rel}	E_b
1 Al	–	–	–	-28.6
A	Si2	O1a	13.6	-29.0
B	Si2	O2a	1.0	-28.9
C	Si3	O2a	1.1	-29.5
D	Si3	O1b	7.5	-27.9
E	Si4	O1b	6.6	-29.5
F	Si4	O3a	30.2	-28.4
G	Si4	O4b	10.3	-28.7
H	Si6	O1c	0.0	-29.3
I	Si6	O2b	4.9	-27.8

this isomer to increase its coordination from two-fold in the bare complex to three-fold in the adsorption complex. Now, the isomer N3 containing two-fold coordinated Cu, should have the higher O₂ adsorption energy. But, in reality, the adsorption energy value for this complex is -12 kcal mol⁻¹. It may be that the position of the proton at an O1 oxygen of the next-neighbor 4-ring has an effect. It can be further noted that the binding energy for O₂ adsorption onto Cu(I) in zeolite with only one Al atom per unit cell is -10.5 kcal mol⁻¹, *i.e.*, also at the lower end of the binding energies for the 2 Al atoms containing adsorption complexes.

Relative energies of dioxygen adsorption complexes of site III: A similar kind of division of relative energies as in the case of bare Cu–complexes (see Section 5.1.2) is observed with little differences. Those are:

- (i) within 1 kcal mol⁻¹
- (ii) from ~ 5.0 to ~ 7.0 kcal mol⁻¹
- (iii) from ~ 10.0 to ~ 30.0 kcal mol⁻¹

Adsorption energies of dioxygen adsorption complexes of site III: It is remarkable that the O₂ binding energies for all of the site III isomers are nearly identical, between -28 and -30 kcal mol⁻¹ (see Table 5.9), and also quite similar to the case of the site

III complex with only 1 Al atom. These values are more than twice as large as the binding energies at the energetically lowest site II complexes discussed above. Thus, the preferred site for O_2 adsorption definitely is site III rather than site II. In a similar study [103] of CO adsorption to Cu(I)–Y zeolite, it was found that CO is more strongly bound to site III than to site II. This is in accordance with the present findings.

5.1.6 Comparison between Computed and Experimentally Obtained Vibrational Frequencies

5.1.6.1 Experimental Results

Oxygen adsorptions on Cu–free and Cu–containing HY zeolite with Cu(I) and Cu(II) were measured at 80 K by means of FTIR spectroscopy [2]. Upon O_2 adsorption onto the Cu–free HY zeolite two lines appear in the spectrum at 1556 and 1551 cm^{-1} . Consequently, they are assigned to the weakly adsorbed dioxygen. These bands are attributed in literature to the adsorption on Brønsted and Na sites under formation of end-on adducts [117, 118].

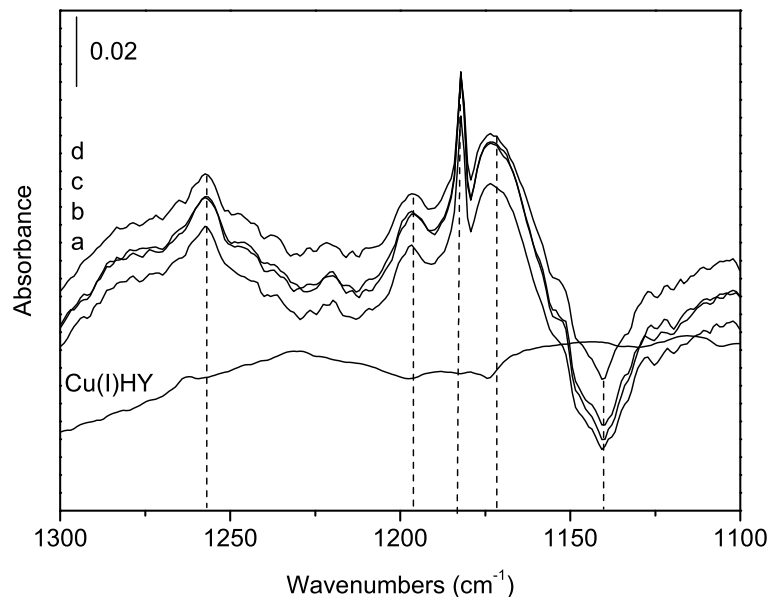


FIGURE 5.6: Low frequency range of FTIR spectra at 80 K of O_2 on Cu(I)HY, compared with the spectrum of the blank zeolite. The equilibrium pressure amounts to 5 (a), 10 (b), 50 (c) and 100 mbar oxygen (d).

The stretching frequencies of O_2 adsorbed in the Cu–containing zeolites lie in a range of intense absorptions by the zeolite lattice, which makes their detection difficult. The

TABLE 5.10: Scaled harmonic O₂ stretching frequencies (ν_{O-O}/cm^{-1}) of various adsorption complexes (with different Al atom contents) of site II. The scaling factor is 1.02.

Isomers	2 nd Al atom replaces	H atom is connected to	ν_{O-O}
1 Al	–	–	1319
A	Si2	O2a	1278
N1	Si2	O1b	1316
B	Si2	O4b	1260
C	Si3	O4b	1263
N2	Si3	O1c	1315
D	Si3	O2b	1207
E	Si4	O2b	1318
E'	Si4	O2b	1195
N3	Si4	O1d	1192
F	Si4	O4c	1324

experimental spectrum (Fig. 5.6) shows the low frequency spectrum of the Cu(I)HY zeolite without O₂ adsorption and the difference spectra obtained after O₂ adsorption depending on the oxygen pressure. In this range, the Cu-free zeolite does not show any absorption but Cu(I) and Cu(II) zeolites show identical results. Two small peaks arise upon O₂ adsorption: the first one appears at 1256 cm⁻¹ and the second, very sharp one, at 1180 cm⁻¹. These correspond to frequency shifts of 300 and 376 cm⁻¹, respectively. Note that the frequency shifts due to adsorption of CO are much smaller as discussed in Ref. [103].

5.1.6.2 Theoretical Results

The experimental Raman frequency of free dioxygen in the $^3\Sigma_g^-$ state is 1556 cm⁻¹ [119]. The corresponding harmonic frequency at the BP86/TZVP level is 1525 cm⁻¹. The DFT result shows that the O₂ stretching frequency is slightly underestimated. This is a well known trend and has been studied in detail by Neugebauer and Hess [120]. Consequently, a scaling factor of 1.02 is used in order to correlate computed and experimental O₂ stretching frequencies.

Free oxygen is IR inactive, but when it is adsorbed, no matter whether this is end-on or side-on, its symmetry is broken and its stretching vibration becomes IR active [117, 118]. The calculated frequencies of the O₂ stretching modes for the different

TABLE 5.11: Scaled harmonic O₂ stretching frequencies (ν_{O-O}/cm^{-1}) of various adsorption complexes (with different Al atom contents) of site III. The scaling factor is 1.02.

Isomers	2 nd Al atom replaces	H atom is connected to	ν_{O-O}
1 Al	–	–	1188
A	Si2	O1a	1164/1157
B	Si2	O2a	1184/1185
C	Si3	O2a	1185/1183
D	Si3	O1b	1189/1191
E	Si4	O1b	1182
F	Si4	O3a	1190
G	Si4	O4b	1187
H	Si6	O1c	1184
I	Si6	O2b	1190/1193

adsorption complexes are listed in Tables 5.10 & 5.11. Calculation of the harmonic frequency of dioxygen adsorbed to the sites II and III in model clusters containing one Al atom yield transitions at 1319 cm^{-1} and 1188 cm^{-1} . The assignment of the oxygen stretching modes in clusters with two Al atoms is not as clear as in the previous case. Due to the strong coupling with framework vibrations in many cases there is no distinct O₂ stretching mode observed but a significant O₂ stretching contribution to two or more framework modes instead. As can be seen from Table 5.10 the stretching modes for site II scatter over a range of more than 100 cm^{-1} and thus do not allow for a definite assignment. On the other hand, for site III the O₂ stretching modes (cf. Table 5.11) of all energetically low lying isomers, *i.e.*, structures B, C, D, E, H and I (cf. Table 5.9) scatter by less than 10 cm^{-1} .

Under the assumption that the computed stretching modes in Tables 5.10 & 5.11 are underestimated as observed for free dioxygen, the theoretical results can be compared to the experimental spectrum. For site II with one Al atom, the computed frequency does not match one of the experimental bands. However, the transition for site III with one Al atom agrees nicely with the sharp peak at 1180 cm^{-1} in (Fig. 5.6).

For site III with two Al atoms, the stretching modes of all energetically low-lying isomers are in the range of $1183\text{--}1193 \text{ cm}^{-1}$ and this supports the experimentally observed peak at 1180 cm^{-1} . The O₂ stretching frequencies of the most stable isomers for site II scatter tremendously and thus it is very difficult to relate the observed peak to a specific

isomer although the frequency of the most stable isomer N3 (1192 cm^{-1}) may also be associated with the observed band. The peak at 1256 cm^{-1} cannot be explained on the basis of the adsorption of O_2 at site III, while two isomers of site II (B and C) result in frequencies at 1260 and 1263 cm^{-1} . However, these isomers are significantly higher in energy than isomer N3 and thus it is rather questionable if these structures are responsible for the observed band. Consequently, the experimental peak at 1180 cm^{-1} can be explained on the basis of the DFT calculations for site III but the interpretation for the band observed at 1256 cm^{-1} remains open.

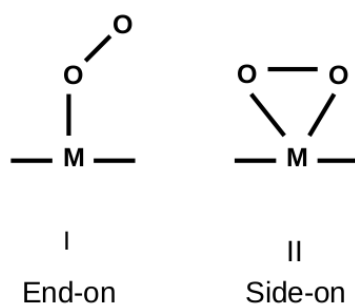
Assignment of Brønsted sites: In order to study the adsorption of dioxygen to Brønsted sites, QM/MM calculations were performed for complexes consisting of dioxygen and zeolite fragments containing one Al atom and an additional proton attached to one of the neighboring O atoms, *i.e.*, forming a Si(OH)Al moiety. Copper atoms had to be eliminated from these calculations because of the preferred binding of dioxygen to copper in comparison to the Brønsted center. In these model calculations, O_2 is adsorbed end-on to the additional proton with an adsorption energy up to 0.6 kcal mol^{-1} , a value much lower than for the copper complexes. Harmonic O_2 stretching frequencies scatter in the range between 1518 and 1528 cm^{-1} (1548 – 1558 cm^{-1} after scaling). Consequently, our QM/MM calculations readily explain the occurrence of the new bands in the experimental spectrum due to the adsorption of dioxygen to Brønsted centers in copper-free cavities. Therefore, these peaks have no relevance for the adsorption process studied here.

Other bands: Now the bands around 1200 cm^{-1} in the experimental spectrum are discussed in detail. One explanation for the origin of the two broad bands about 20 cm^{-1} above and below the sharp peak at 1180 cm^{-1} may belong to the rotational sidebands which may show up due to symmetry breaking. The rotational splitting could not be detected due to the fact that the expected splitting value of oxygen adsorbed on sites II and III lies in the range of the spectral resolution. The combination of pure stretching vibrations with the bands of vibration-rotational mode is well known in the case of hydrogen adsorption on alkali metals in Y and X zeolites [121, 122]. The detection of vibration-rotational bands, their splitting and displacement indicate different hindering of free rotation of hydrogen depending on the alkali metal. However, the negative amplitude at about 1140 cm^{-1} indicates that the broad band at about 1170 cm^{-1} cannot only be due to a rotational sideband but may also involve some framework vibrations. A combination of these two effects can easily explain the asymmetry of the two bands

below and above the sharp band at 1180 cm^{-1} . Another explanation of these two broad bands could be that they arise from different adsorption sites.

End-on vs. Side-on O_2 adducts: $\nu_{\text{O}-\text{O}}$ stretching vibrations of dioxygen adducts of $\text{M}(\text{O}_2)$ -type show up in the region of $1200\text{--}1100\text{ cm}^{-1}$, and this type of dioxygen adducts of metal complexes are called “*superoxo*” complexes, because their frequencies are close to that of KO_2 [123].

The structures of dioxygen adducts of $\text{M}(\text{O}_2)$ -type can be classified into two types:



Hence, a side-on adduct has two equivalent oxygens (as long as the symmetric environment is concerned), and an end-on adduct has two non-equivalent oxygens, therefore isotope substitution technique will be able to distinguish between side-on and end-on adducts. $\nu_{\text{O}^{16}\text{--}\text{O}^{18}}$ vibration splits into two bands in case of end-on adduct, whereas for side-on no splitting will be observed. However, the distinction of dioxygen adducts is not always clear-cut, because of the environmental effects of complex compounds. From the calculated harmonic O_2 stretching frequencies, finally a conclusion can be drawn: O_2 stretching frequencies in side-on O_2 adsorption complexes lie in the frequency region ~ 1160 to $\sim 1190\text{ cm}^{-1}$, and in the case of end-on O_2 adsorption complexes, the range is ~ 1200 to $\sim 1300\text{ cm}^{-1}$.

5.2 Adsorption of Benzene

5.2.1 Geometries

A systematic theoretical study of cluster models for the adsorption of benzene to different cationic sites (II and III) within the zeolite has been performed in full analogy to the previous study on the O_2 adsorption to CuHY zeolite [2] except for the size of the cluster for site II. A 6T cluster model is chosen for studying the adsorption complexes of C_6H_6 as the QM part within the QM/MM calculations, while in the case of O_2 adsorption, a larger 12T QM model was considered. The adsorption energies of C_6H_6 in 1 Al atom containing 6T and 12T adsorption complexes are -17 , and -19 kcal mol $^{-1}$, with a difference of 2 kcal mol $^{-1}$, which is non-negligible. Nevertheless, considering the additional computational cost due to the increase of the number of atoms, a 6T QM cluster is taken for QM/MM calculations.

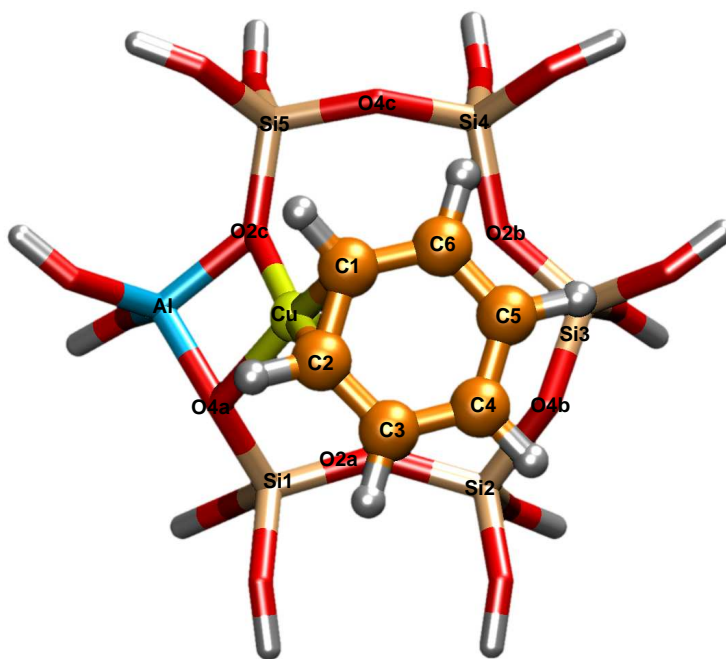


FIGURE 5.7: Quantum mechanically treated zeolite fragment (6T model) with adsorbed C_6H_6 at cationic site II, for the case of 1 Al atom containing complex demonstrating the η^2 -coordination of benzene to Cu.

Different Si/Al ratios in zeolite complexes based on 1 or 2 Al atoms per unit cell have been considered. Due to the different substitution patterns for the second Al atom and the addition of a proton (to neutralize the extra charge) [2], 6 and 9 isomers (adsorption

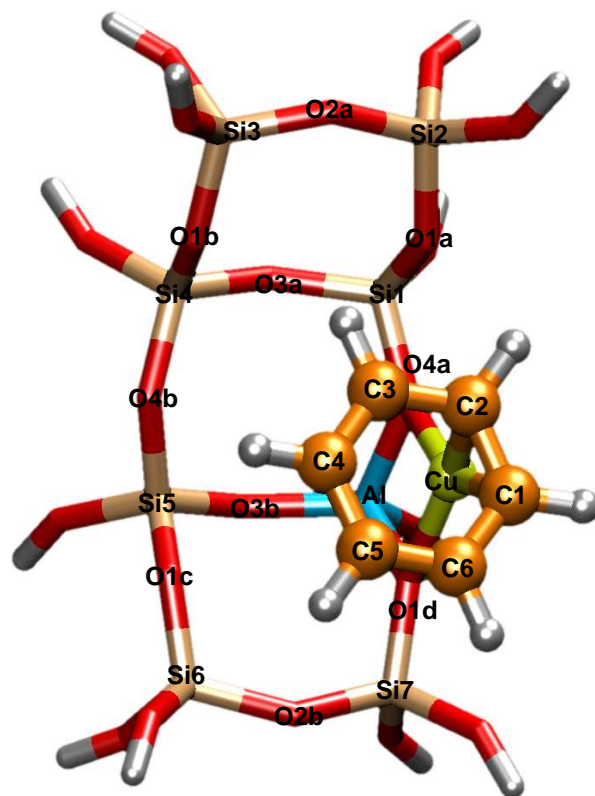


FIGURE 5.8: Quantum mechanically treated zeolite fragment (8T model) with adsorbed C_6H_6 at cationic site III, for the case of 1 Al atom containing complex demonstrating the η^2 -coordination of benzene to Cu.

complexes) are obtained for sites II and III, respectively. These isomers are described in Tables 5.12 & 5.13.

1 Al atom containing complexes: Upon benzene adsorption onto Cu(I) atom in Y zeolite with 1 Al atom per unit cell, the following features have been computed for the adsorption complexes:

1. At site II (see Fig. 5.7), the coordination around the Cu atom changes from three-fold to two-fold concerning the zeolitic framework oxygen atoms. While in the bare cluster (without adsorbate) solely O2 type oxygens are bonded to the Cu atom, after adsorption of benzene O2 and O4 type oxygen atoms are coordinated to copper. After benzene adsorption the Cu atom moves out of the plane of T (Si/Al) atoms of the 6-ring and comes closer to the nearest neighboring Al atom [75].

TABLE 5.12: Geometrical parameters of various adsorption complexes of benzene at site II with 2 Al atoms. The results in the first line refer to the case of 1 Al atom in a unit cell. Distances are given in Å. For the numbering of atoms, see Fig. 5.7.

Isomers	2 nd Al atom replaces	H atom is connected to	R_{Cu-O}	R_{C1-C2}	${}^a\sigma_{C-C}$	${}^b\pi_{C-C}$	R_{Cu-C1}	R_{Cu-C2}	${}^cR_{Cu-C}$
1 Al	-	-	O2 (2.104); O4 (2.098)	1.434	1.420	1.386	2.051	2.036	2.794
A	Si2	O2a	O2 (1.952)	1.429	1.416	1.393	2.063	2.067	2.690
B	Si2	O4b	O2 (2.100, 2.121)	1.431	1.420	1.390	2.064	2.076	2.858
C	Si3	O4b	O2 (2.068); O4 (2.113)	1.435	1.421	1.388	2.048	2.039	2.828
D	Si3	O2b	O4 (1.909)	1.429	1.417	1.392	2.098	2.030	2.725
E	Si4	O2b	O2 (2.128); O4 (2.064)	1.435	1.421	1.387	2.038	2.045	2.782
F	Si4	O4c	O2 (2.225); O4 (2.051)	1.435	1.419	1.387	2.060	2.038	2.778

${}^a\sigma_{C-C}$ is the average bond length of R_{C2-C3} , R_{C4-C5} , R_{C6-C1} .

${}^b\pi_{C-C}$ is the average bond length of R_{C3-C4} , R_{C5-C6} .

${}^cR_{Cu-C}$ is the average Cu–C bond length.

2. For site III (see Fig. 5.8), there is no significant change in the structural parameters of the adsorption complexes with respect to the bare cluster. Though there is no change in the coordination number (two-fold coordination by O1 and O4 type oxygen atoms) of the Cu atom concerning the framework oxygens, both Cu–O (coordinated oxygens) and Cu–Al bond distances are increased.
3. The bonding pattern of benzene to the Cu atom is η^2 at both sites (II and III). The C1–C2 bond, directly connected to the Cu(I) ion, elongates from 1.399 Å in our calculation for free benzene (experimental value is 1.3902 ± 0.0002 Å [124]) to 1.434 Å at site II (1.432 Å at site III). There are two similar Cu–C1(C2) bonds of length ~ 2.0 Å at both sites. The average Cu–C bond distances are 2.794 Å and 2.697 Å at site II and site III, respectively. The average σ (C–C) and average π (C–C) bond lengths of the adsorbed benzene are 1.420 Å and 1.386 Å respectively at site II (Table 5.12), and 1.419 Å and 1.388 Å respectively at site III (Table 5.13).

2 Al atom containing complexes: Moving now to the benzene adsorption complexes with two Al atoms per unit cell (Figs. 5.9 and 5.11), the following features can be noted:

1. For some isomers (A, D, E) of site II, internal hydrogen-bonding (see Fig. 5.10) between an O2 type oxygen atom and the additional proton (located at another O2 type oxygen atom) is observed. The C1–C2 bond length varies from 1.429 Å to 1.435 Å in different isomers, and the Cu–C1(C2) bond distances vary from 2.03 Å to 2.1 Å (Table 5.12). The average Cu–C bond distance lies in the range from 2.690 Å to 2.858 Å. The η^2 -benzene coordination remains unchanged throughout all the isomers, but there are significant differences among the isomers with respect to the coordination of Cu to the 6-ring oxygens. Several isomers retain their two-fold Cu coordination (one O2 type and one O4 type) as seen in the 1 Al atom containing complex, but there is also one isomer with two-fold coordination by two O2 type oxygens only. Surprisingly there are even two isomers with one-fold coordination to one of the framework oxygen atoms: in one of them Cu is bound to an O2 type oxygen atom (isomer A) and in the other to an O4 type oxygen atom (isomer D). Note that these two isomers belong to those which establish an internal hydrogen-bond on the plane of the 6-ring, and thereby causing the $\text{Cu}^+\text{C}_6\text{H}_6$ moiety to be repelled from the plane towards the supercage.

TABLE 5.13: Geometrical parameters of various adsorption complexes of benzene at site III with 2 Al atoms. The results in the first line refer to the case of 1 Al atom in a unit cell. Distances are given in Å. For the numbering of atoms, see Fig. 5.8.

Isomers	2 nd Al atom replaces	H atom is connected to	R_{Cu-O}	R_{C1-C2}	${}^a\sigma_{C-C}$	${}^b\pi_{C-C}$	R_{Cu-C1}	R_{Cu-C1}	${}^cR_{Cu-C}$
1 Al	-	-	O1 (2.016); O4(2.165)	1.432	1.419	1.388	2.071	2.024	2.697
A	Si2	O1a	O1 (1.909)	1.427	1.413	1.399	1.988	2.243	2.630
B	Si2	O2a	O1 (2.029); O4 (2.125)	1.432	1.420	1.388	2.068	2.015	2.700
C	Si3	O2a	O1 (1.987); O4 (2.243)	1.432	1.419	1.390	2.093	2.006	2.687
D	Si3	O1b	O1 (2.001); O4 (2.174)	1.433	1.421	1.387	2.048	2.033	2.745
E	Si4	O1b	O1 (2.046); O4 (2.082)	1.435	1.421	1.386	2.027	2.039	2.774
F	Si4	O3a	O1 (1.966); O4 (2.353)	1.432	1.418	1.390	2.074	2.025	2.691
G	Si4	O4b	O1 (2.080); O4 (2.070)	1.435	1.421	1.387	2.035	2.037	2.763
H	Si6	O1c	O1 (1.998); O4 (2.173)	1.434	1.421	1.388	2.054	2.025	2.771
I	Si6	O2b	O1 (2.047); O4 (2.159)	1.432	1.420	1.389	2.085	2.014	2.704

${}^a\sigma_{C-C}$ is the average bond length of R_{C2-C3} , R_{C4-C5} , R_{C6-C1} .

${}^b\pi_{C-C}$ is the average bond length of R_{C3-C4} , R_{C5-C6} .

${}^cR_{Cu-C}$ is the average Cu–C bond length.

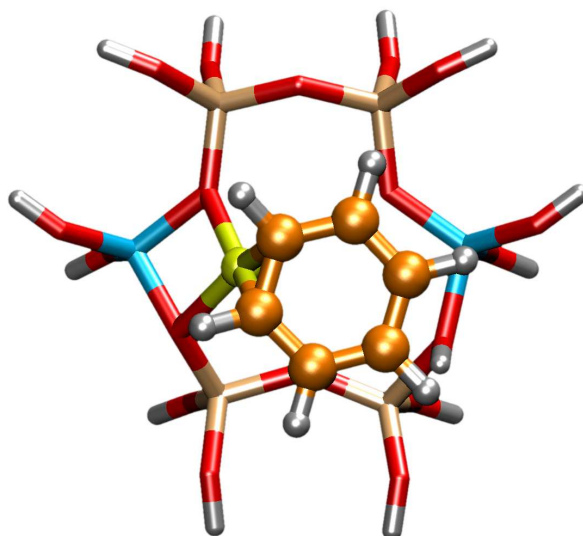


FIGURE 5.9: Quantum mechanically treated zeolite fragment (6T model) with adsorbed C₆H₆ at cationic site II, 2 Al atoms containing complex (isomer C) demonstrating the η^2 -coordination of benzene to Cu.

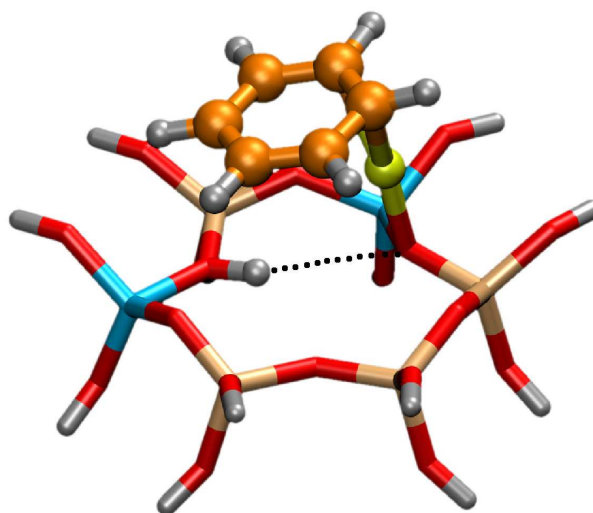


FIGURE 5.10: Quantum mechanically treated zeolite fragment (6T model) with adsorbed C₆H₆ at cationic site II (isomer A), showing an internal hydrogen-bond.

Besides, the movement of the Cu atom from the plane of T atoms towards the supercage has been observed in rest of the isomers, although it was not as strong as it is observed in case of isomers A and D.

2. At site III, the introduction of the second Al atom does not lead to a significant change among the adsorption complexes of benzene. Here too η^2 -benzene

coordination prevails except isomer A where an η^3 -benzene is observed (see Fig. 5.12). Two-fold coordination (O1 and O4 type of zeolitic oxygens) around the Cu atom remains the same in all isomers except for one isomer (A) where one-fold coordination to the 4-ring O atom is found. This isomer contains the additional proton located at an O1 type oxygen. This particular proton is oriented towards the $\text{Cu}^+\text{C}_6\text{H}_6$ moiety. Both these species, possibly repelling each other, are situated at the edge of two 4-rings. The $\text{Cu}^+\text{C}_6\text{H}_6$ moiety is displaced towards the supercage. The C1–C2 bond distance in benzene varies for different isomers from 1.427 Å (in isomer A) to 1.435 Å (all other isomers). A little asymmetry is observed in η^2 -coordinated Cu–C1(C2) bond lengths for isomer A: 1.988 (2.243) Å. The rest of the isomers have symmetrical Cu–C1(C2) lengths, scattering between 2.01 Å and 2.09 Å (Table 5.13). The average Cu–C bond length lies between 2.630 Å and 2.774 Å.

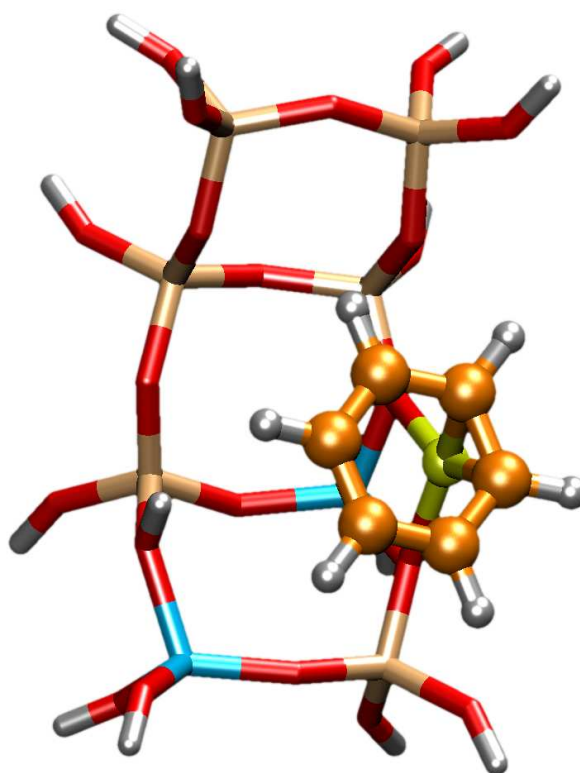


FIGURE 5.11: Quantum mechanically treated zeolite fragment (8T model) with adsorbed C_6H_6 at cationic site III, 2 Al atoms containing complex (isomer H) demonstrating the η^2 -coordination of benzene to Cu.

Within experimental studies, different positions of Cu(I) ions in Y zeolite have been investigated employing XRPD (X-ray Powder Diffraction), XAS (X-ray Absorption

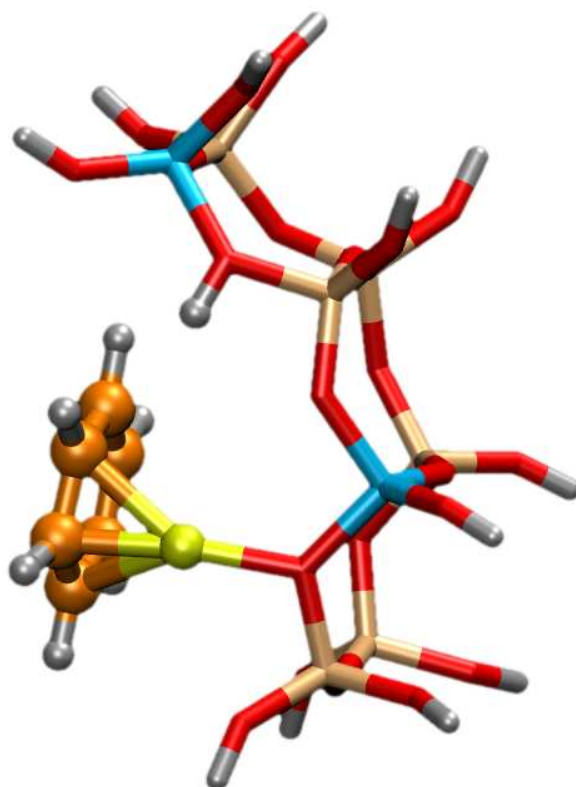


FIGURE 5.12: Quantum mechanically treated zeolite fragment (8T model) with adsorbed C_6H_6 at cationic site III, 2 Al atoms containing complex (isomer A) demonstrating the η^3 -coordination of benzene to Cu.

Spectroscopy) and IR spectroscopies [74]. In the adsorption complexes, Cu(I) coordination to the framework oxygen atoms is lowered upon adsorption of C_6H_6 , and the Cu(I) cations show migration towards the supercage. Similar behavior of Cu(I) has been observed by Kumashiro *et al.* and Lamberti *et al.* through EXAFS experiments in case of CO adsorption in copper–Y zeolite [74], ZSM-5 [125, 126], and theoretically by Nachtigall *et al.* in ferrierite [127].

According to the calculations, the length of the C1–C2 bond, (*i.e.*, the bond directly connected to Cu) lies in the range of 1.429–1.434 Å at site II (1.427–1.435 Å at site III) in comparison to 1.3902 ± 0.0002 Å [124] in the case of free benzene. This indicates a slight activation of the C–C bond in benzene by the Cu-exchanged Y zeolite. According to Datka and co-workers [128] and the results from Hübner *et al.* [129, 130], C–C bond activation by Cu^+ in zeolites is much weaker in benzene than in alkenes (ethene, propene, *cis*-but-2-ene, *trans*-but-2-ene) and alkyne (acetylene). An EXAFS experiment shows an average Cu–C bond length of 2.64 ± 0.03 Å [114], which is in nice agreement with the values calculated for site III (2.63 – 2.77 Å). More precisely,

$C_6H_6/CuHY$ zeolite with 2 Al atoms at site III seems to represent the real situation better than site II.

5.2.2 Charges

Population analysis can determine and interpret the charge distribution of associated atoms of a molecule. To get a deeper insight into the process of activation of benzene in the Cu-exchanged zeolite matrix, population analysis calculations were performed for Cu–Y zeolites (sites II and III) containing 1 Al atom per unit cell of interest, with and without benzene, using the natural population analysis of Reed and Weinhold [116] as implemented in TURBOMOLE.

TABLE 5.14: Population analysis results for sites II and III: bare–Cu complexes and C_6H_6 adsorption complexes containing 1 Al atom.

Adsorption site	Atom/molecule	Charges	Orbital	Population
Bare–complex				
II	Cu	0.85	4s	0.26
			3d	9.88
III	Cu	0.89	4s	0.17
			3d	9.92
C_6H_6 –Complex				
II	Cu	0.96	4s	0.29
			3d	9.74
III	C_6H_6	-0.11		
	Cu	0.96	4s	0.29
			3d	9.74
	C_6H_6	-0.10		

Before benzene adsorption, the Cu cation changes its charge from +1.0 for the free cation to +0.85 at site II (+0.89 at site III). There is a 3d hole of charges 0.12 and 0.08 at sites II and III, respectively, whereas the corresponding 4s orbital occupations are 0.26 and 0.17, respectively. After adsorption of benzene the following results are obtained: The Cu cation has a net charge of +0.96, (*i.e.*, it is even more positive than at pre-adsorption) at both sites, and benzene has a net charge of –0.11 at site II (–0.10 at site III). Also, the 3d hole increases by 0.14 and 0.18 at sites II and III, respectively.

All these mean that there is a net flow of electron density from Cu to the adsorbed benzene, mainly from the $3d$ orbitals. However, there is also a σ electron donation from benzene: the $4s$ occupation of Cu is increased by 0.03 and 0.12 for sites II and III, respectively, and there is even a very slight electron donation to the $4p$ orbitals. Thus, the Dewar-Chatt-Duncanson [131, 132] model of the synergetic combination of σ donor and π acceptor interaction between metal and π system is applicable. Note that all these effects are significantly smaller than seen for the O_2 adsorption process. Refer to Appendix C.5 for charge analyses of benzene in all isomers of sites II and III.

5.2.3 Energies

As reported by Sierka and co-workers [103] and discussed in the case of adsorption of O_2 [2], Cu(I) is bound stronger to site II than to site III in the bare Y zeolite. Lamberti *et al.* reported that Cu(I) occupancy was higher at site II than at site III according to their XRPD (X-ray Powder Diffraction) [74] and EXAFS [77] studies on Y zeolite. This situation is reversed in the case of adsorbates [2, 103], *i.e.*, adsorbates bind more strongly to the lower coordinated copper at the cationic site. As a general rule, weak coordination of the adsorbate to the strongly interacting Cu(I) site has been observed by several authors [103, 133], as in the present case of benzene adsorption.

Relative energies of benzene adsorption complexes of site II: As in the case of O_2 adsorption complexes of site II, the additional proton can either be located at the O4 or O2 type oxygen atom of the 6-ring. The complexes where the proton is residing on an O2 type oxygen, are higher in energy than the complexes containing a proton located at an O4 type oxygen – thus, reflecting the situation of O_2 adsorption and bare Cu–complexes as well. As a consequence, two regions of relative energies (Table 5.15) are found among all the benzene adsorption complexes:

- (i) lower-end, $< 1 \text{ kcal mol}^{-1}$ where the proton is located at the O4 type oxygen atom of the 6-ring
- (ii) higher-end, $> 1 \text{ kcal mol}^{-1}$ where the proton is located at the O2 type oxygen atom of the 6-ring

Adsorption energies of benzene adsorbed complexes of site II: Binding energies of benzene vary between $\sim -11 \text{ kcal mol}^{-1}$ and $\sim -35 \text{ kcal mol}^{-1}$ among the isomers with two Al atoms at site II (Table 5.15), and $\sim -17 \text{ kcal mol}^{-1}$ is the corresponding

TABLE 5.15: C_6H_6 adsorbed at site II in Cu–Y zeolites (6T QM cluster model): relative stabilities (E_{rel}) of different adsorption complexes, and binding energies (E_b) of C_6H_6 . The result in the first line refers to the case of 1 Al–complex, and the others to the various isomers containing 2 Al atoms. For the numbering of atoms, see Fig. 5.7. All the quantities are given in kcal mol⁻¹.

Isomers	2 nd Al atom replaces	H atom is connected to	E_{rel}	E_b
1 Al	-	-	-	-16.9
A	Si2	O2a	7.0	-27.5
B	Si2	O4b	0.1	-16.6
C	Si3	O4b	0.0	-16.7
D	Si3	O2b	2.1	-35.2
E	Si4	O2b	10.5	-29.8
F	Si4	O4c	1.1	-11.3

value in CuY zeolite with one Al atom. According to our relative energy classification, the lower-end is occupied by isomers B, C, F – the energetically low-lying (most stable) isomers with the additional proton bonded to O4 type zeolitic oxygens, and the adsorption energies of benzene vary between ~ -11 and -17 kcal mol⁻¹. On the other hand, the higher-end of relative energies belong to isomers A, D, and E – where the additional proton is located at the O2 type oxygen atoms, and the adsorption energies of benzene lie in the range of ~ -27 to -35 kcal mol⁻¹. Thus, there are two categories of adsorption complexes in this case too:

- (i) complexes where the proton is located at the O4 type oxygen atom of the 6-ring with adsorption energies in the range of ~ -11 to -17 kcal mol⁻¹
- (ii) complexes where the proton is located at the O2 type oxygen atom of the 6-ring with adsorption energies in the range of ~ -27 to -35 kcal mol⁻¹

Relative and adsorption energies of benzene at site III: Benzene binds stronger at site III than at site II with one or two Al atoms. The binding energies of benzene in all of these adsorption complexes lie between ~ -32 and ~ -38 kcal mol⁻¹ (Table 5.16). There are several low energy isomers (0.0 to ~ 1.4 kcal mol⁻¹) such as B, C, H, I; but in all these isomers the binding energy is very similar. One isomer (F) is significantly higher in energy ($+28.4$ kcal mol⁻¹) than the others, which is a result of an unfavorable connection of the additional proton to the bridging O3 type (see Fig. 5.8) framework oxygen atom.

TABLE 5.16: C_6H_6 adsorbed at site III in Cu–Y zeolites (8T QM cluster model): relative stabilities (E_{rel}) of different adsorption complexes, and binding energies (E_b) of C_6H_6 . The result in the first line refers to the case of 1 Al–complex, and the others to the various isomers containing 2 Al atoms. For the numbering of atoms, see Fig. 5.8. All the quantities are given in kcal mol⁻¹.

Isomers	2 nd Al atom replaces	H atom is connected to	E_{rel}	E_b
1 Al	-	-	-	-33.5
A	Si2	O1a	7.6	-38.7
B	Si2	O2a	0.9	-32.7
C	Si3	O2a	0.3	-34.1
D	Si3	O1b	4.3	-34.9
E	Si4	O1b	5.5	-34.4
F	Si4	O3a	28.4	-34.1
G	Si4	O4b	7.1	-35.7
H	Si6	O1c	0.0	-36.4
I	Si6	O2b	1.4	-35.1

The isomer A, which has only one-fold Cu–framework oxygen coordination, Cu– C_6H_6 shows strong binding. Thus, this isomer has the highest adsorption energy (-38.7 kcal mol⁻¹) for this isomer. All other adsorption complexes show similar two-fold Cu–O coordination, and their adsorption energies lie between ~ -32 and ~ -36 kcal mol⁻¹.

Therefore all of these observations support the assumption that the position of the additional proton, the detailed distribution of Al atoms, the coordination around the metal center may play significant roles in catalysis. In the present study, site III appears to be the preferred adsorption site in CuHY zeolite for benzene.

5.2.4 Frequencies

After adsorption to surfaces, the gas-phase vibrational bands of a molecule may shift differently depending on the strength of interaction with active sites. For instance, in the case of X zeolite the ν_{13} mode of adsorbed benzene is shifted from the gas-phase value of 1484 cm⁻¹ to 1478 cm⁻¹, due to the bonding with Na⁺ (which is still present in Cu–X zeolite), and an extra band shows up at 1468 cm⁻¹ corresponding to the bonding to Cu⁺ [134]. This differs from the adsorption of benzene to bimetallic Pt,CuZSM-5 zeolite where two new bands emerge [135]. Similar effects in the case of gaseous

transition metal–benzene complexes are described in IR-REMPD (Infrared resonance-enhanced multiple-photon dissociation) studies by Duncan *et al.* [136]; where the frequency shift is explained by charge-transfer between benzene and metal ion. According to the population analysis results in Section 5.2.2, such a charge transfer occurs indeed in the bonding of benzene to the Cu–Y zeolite. Both σ donation (and a minute π donation) from benzene to Cu–Y and π back-donation is observed, and both effects weaken the C–C bond and result in a large redshift.

5.2.4.1 Computed Frequencies

In this section, calculated harmonic frequencies of adsorbed benzene at two different cationic sites (II, III) of Cu(I)–Y zeolite are discussed. The frequencies are scaled by a factor obtained from a comparison of the corresponding experimental [137] and calculated frequencies (excluding the C–H stretching modes) of free benzene. The scaling factor is 1.012 at the BP86/TZVP level of theory (0.982 at the B3LYP/TZVP level). The BP86/TZVP harmonic frequencies, experimental IR frequencies, frequency shifts of free benzene and adsorbed benzene are compared in Table 5.17 (for selected modes).

The computed IR frequency value of the ν_{13} band (C–C in-plane ring stretching) in free benzene is 1489 cm^{-1} , at the BP86/TZVP level, as compared to the experimental value of 1484 cm^{-1} [137]. After adsorption of benzene to Cu(I), ν_{13} of benzene in the adsorption complex containing one Al atom appears at 1463 cm^{-1} and 1465 cm^{-1} , at sites II and III, respectively. This particular C–C ring stretching vibration scatters over a range of 9 cm^{-1} (from 1461 to 1470 cm^{-1}) at sites II and III (from 1463 to 1472 cm^{-1}) for adsorption complexes with two Al atoms (see Table 5.17). Thus, a down-shift of $19 - 28\text{ cm}^{-1}$ at site II and $17 - 26\text{ cm}^{-1}$ at site III are obtained among all the adsorption complexes, while the experimental IR spectrum shows a down-shift of 13 cm^{-1} for ν_{13} . Although calculated and experimental values do not match exactly, and even some calculated frequency shifts are doubly as large as the experimentally predicted value, there is good agreement between experiment and theory for some of the adsorption complexes (*e.g.* isomer A at sites II and III).

In contrast to the ν_{13} band, the experimental ν_{14} (C–H bending) and ν_4 (C–H bending) modes remain nearly unchanged, while the calculations predict a redshift for ν_{14} , and

TABLE 5.17: Comparison between experimental and calculated harmonic frequencies ν/cm^{-1} and frequency shifts $\Delta\nu/cm^{-1}$ of benzene in gas-phase and in adsorbed state at two sites II, III of CuHY zeolite with different Al contents (1 Al and 2 Al atoms per unit cell) at the BP86/TZVP level. Calculated frequencies are scaled by a factor of 1.012.

	ν_{13} (C–C ring stretch)	$-\Delta\nu_{13}^a$	ν_{14} (C–H bend)	$-\Delta\nu_{14}^a$	ν_4 (C–H bend)	$\Delta\nu_4^a$
Exp/Free ^b	1484		1038		674	
Exp ^c /CuHY	1479	5	1037	1	672	- 2
Exp ^c /CuHY	1471	13				
Calc/Free	1489		1048		672	
Site II						
Calc/Cu-1Al	1463/1459	26/30	1033/1021	15/27	668	- 4
Calc/Cu-2Al						
A	1470/1466	19/23	1030/1021	18/27	677	+ 5
B	1466/1457	23/32	1030/1021	18/27	649	- 23
C	1462/1458	27/31	1034/1017	14/31	657	- 15
D	1467/1463	22/26	1030/1028	18/20	657	- 15
E	1461/1458	28/31	1031/1020	17/28	670	- 2
F	1464/1460	25/29	1031/1024	17/24	661	- 11
Site III						
Calc/Cu-1Al	1465/1458	24/31	1031/1024	17/24	676	+ 4
Calc/Cu-2Al						
A	1472/1464	17/25	1034/1026	14/22	668	- 4
B	1463/1457	26/32	1031/1023	17/25	676	+ 4
C	1467/1458	22/31	1029/1027	19/21	674	+ 2
D	1466/1456	23/33	1031/1022	17/26	673	+ 1
E	1467/1455	22/34	1032/1021	16/27	676	+ 4
F	1465/1460	24/29	1030/1025	18/23	673	+ 1
G	1468/1456	21/33	1032/1022	16/26	677	+ 5
H	1463/1455	26/34	1030/1021	18/27	671	- 1
I	1464/1459	25/30	1031/1025	17/23	675	+ 3

^a $\Delta\nu$ is the frequency shift of benzene from the gas-phase to the adsorbed state.

^b Taken from Ref. [137]

^c Taken from Ref. [1]

TABLE 5.18: Comparison between experimental and calculated harmonic frequencies ν/cm^{-1} and frequency shifts $\Delta\nu/cm^{-1}$ of benzene in gas-phase and in adsorbed state at two sites II, III of CuHY zeolite with different Al contents (1 Al and 2 Al atoms per unit cell) at the B3LYP/TZVP level. Calculated frequencies are scaled by a factor of 0.982.

	ν_{13} (C–C ring stretch)	$-\Delta\nu_{13}^a$	ν_{14} (C–H bend)	$-\Delta\nu_{14}^a$	ν_4 (C–H bend)	$\Delta\nu_4^a$
Exp/Free ^b	1484		1038		674	
Exp ^c /CuHY	1479	5	1037	1	672	- 2
Exp ^c /CuHY	1471	13				
Calc/Free	1491		1043		677	
Site II						
Calc/Cu-1Al	1471/1470	20/21	1032/1020	11/23	673	- 4
Calc/Cu-2Al						
B	1474/1469	17/22	1031/1021	12/22	652	- 25
C	1472/1469	19/22	1034/1017	9/26	663	- 14
F	1476/1472	15/19	1031/1026	12/17	682	+ 5
Site III						
Calc/Cu-1Al	1472/1468	19/23	1030/1022	13/21	681	+ 4
Calc/Cu-2Al						
B	1471/1468	20/23	1032/1022	11/21	682	+ 5
C	1478/1469	13/22	1030/1027	13/16	682	+ 5
H	1472/1467	19/24	1030/1021	13/22	679	+ 2

^a $\Delta\nu$ is the frequency shift of benzene from the gas-phase to the adsorbed state.

^b Taken from Ref. [137]

^c Taken from Ref. [1]

an almost regular blue-shift of 3 to 5 cm^{-1} for ν_4 at site III and a less regular shift at site II (cf. Table 5.17).

B3LYP frequencies: The large redshift of the ν_{13} mode is due to the strong interaction of the C–C bond in benzene with Cu(I). Since pure gradient-corrected functionals are known to overestimate the interaction of molecules (CO, NO) with Cu(I) due to too small HOMO-LUMO gaps [127, 138, 139], some of the adsorption complexes were also studied using the B3LYP functional. The geometries of the low-energy adsorption complexes from BP86/TZVP calculations were re-optimized and harmonic frequencies were computed again. The B3LYP/TZVP results provided in Table 5.18 show lower values of frequency shifts for the ν_{13} and ν_{14} modes, but the shifts of the ν_4 mode remain unchanged.

Reasons behind the mismatch with the experimental results: In the present investigation of benzene–CuHY zeolite adsorption complexes, the calculated frequencies do not match the experimental IR spectra satisfactorily. Plausible explanations would be:

- (i) **Choice of quantum chemical methods:** A strong redshift corresponds to an overestimation of the adsorption energy; both the overbinding between C_6H_6 and Cu^+ and the reduction of the strength of the intramolecular C–C bond in benzene are due to σ electron donation from benzene and back-donation from the Cu $3d$ orbitals. Thus, DFT/TZVP calculations tend to overestimate the interaction energies as well as the frequency shifts. Therefore, more sophisticated methods are needed for obtaining accurate results.
- (ii) **Choice of models:** Benzene could be adsorbed to several adsorption sites rather than our preferred sites of interest. In different kinds of faujasites Barthomeuf and co-workers observed high adsorption on cationic sites (strong Lewis acidity) as well as low adsorption in the 12T ring window (weak oxygen basicity) of a supercage [140–143].

5.2.4.2 Comparison with Related Systems

The strong redshift of the calculated frequencies ν_{13} and ν_{14} in the adsorbed state in comparison to free benzene demonstrates the strong interaction of benzene molecules with copper. Similar effects in the case of gaseous transition metal–benzene complexes were described in previous IR-REMPD studies by Jaeger et al. [136]. In Ref. [136], the frequency shift is explained by a charge-transfer between benzene and metal ions, analogous to those in metal–carbonyl complexes. Consequently, the C–C bonds become weaker and result in the appearance of vibrational bands at lower frequencies. In the present study on the adsorption of benzene to Cu–Y zeolite, a population analysis reveals a large charge-transfer from copper(I) to benzene, and the C–C bond elongates from 1.399 Å in free benzene to 1.434 and 1.432 Å at sites II and III, respectively. The reported binding energies for one benzene molecule (32.1–37.1 kcal mol⁻¹) and Cu–C bond length (2.434 Å) in $Cu(benzene)_2^+$ by Jaeger et al. [136], are comparable with the present calculated results in the case of benzene adsorption at site III and the EXAFS study of the same system [114]. The results of di-benzene copper complexes in the gas

phase are compared with the present benzene adsorption study under the assumption that the zeolite six-ring window of the sodalite cage may play a similar role in the geometry as the second benzene ring. Moreover the $\text{Cu}(\text{benzene})_2^+$ complexes described by Jaeger et al. [136], show similar copper dislocation away from the benzene 6-fold axis, whereas copper is located at the axis in the structure of monomer in $\text{Cu}(\text{benzene})^+$. The benzene–copper adsorption complexes at sites II and III with direct coordination of copper to the C1–C2 bond demonstrate the displacement of the copper ion from the benzene-6-fold axis as well, so that the obtained geometry can probably be explained by the repulsion of the benzene molecule and the zeolite ring window. As mentioned before, despite the lower copper occupancy at site III, benzene seems to be preferentially adsorbed at site III rather than at site II (Tables 5.15 & 5.16). The average Cu–C bonds also show shorter distances at site III, and they are comparable with the EXAFS measurements [114].

The earlier studies on adsorption of ethylene to CuNaY zeolite [129] give a detailed assignment of different vibration bands of ethylene. In the FTIR spectrum a C–H stretching mode appears at $\sim 3011 \text{ cm}^{-1}$ which is IR-silent in gas-phase ethylene. Ethylene binds to Cu as η^2 -ethylene-copper adsorption complex as in this study. A well known example in the literature [144] showed a detailed characterization of ethane adsorption complexes on copper sites of Cu–ZSM-5 zeolites. The appearance of C–H IR-bands at room temperature with a frequency redshift of more than 300 cm^{-1} compared to gaseous ethane was established through the formation of η^1 - and η^2 -ethane-copper adsorption complexes, which lead to the weakening of the C–H bonds. On the other hand, in the experimental FTIR spectra of benzene adsorbed onto Cu–HY zeolite by Archipov et al. [1], IR-forbidden C–H stretching bands were not detected, because the copper ions interact directly with the carbon atoms of benzene (π -bonds) so that the formation of C–H–Cu (σ -bonds) is not possible.

5.2.4.3 Splitting of Degenerate Modes

The computed splitting of the degenerate ν_{13} and ν_{14} bands due to symmetry breaking upon adsorption could not be confirmed by experimental results of Archipov et al. [1]. According to the DFT/MM calculations this splitting varies between 2 and 17 cm^{-1} (Table 5.17) depending on the adsorption on different sites and should be detectable at the experimental resolution of 2 cm^{-1} . The appearance of only one band for each adsorption on Brønsted sites and on copper at room temperature may be explained by

the rotational motion of the benzene molecules about the 6-fold (pseudo-6-fold) axis [145] or/and by the re-orientational jumps of benzene molecules to other active sites within the super cage [146, 147].

According to Archipov et al. [1], the IR spectra were measured at room temperature and at 80 K to search for a splitting of the 1471 cm^{-1} band. At 80 K the intensity of the band at 1479 cm^{-1} increases whereas the intensity of the copper band at 1471 cm^{-1} remains unchanged. This fact could lead to the conclusion that the splitting of the copper band may exist and overlap with the band at 1479 cm^{-1} , which is responsible for Brønsted sites.

Interestingly, in previous IR-REMPD experiments the splitting of these bands was also not detected [136]. When benzene is adsorbed to the zeolites of the BEA family, the frequencies of the in-plane C–C/C–H stretching bands match with the characteristic vibration bands of liquid-phase benzene, but the out-of-plane bending vibrations undergo splitting [148].

Chapter 6

Simultaneous Adsorption of Dioxygen and Benzene

6.1 The Motivation

The motivation behind the present work is to investigate the reaction: $2\text{C}_6\text{H}_6 + \text{O}_2 \xrightarrow{\text{Cu}-\text{Y}} 2\text{C}_6\text{H}_5\text{OH}$ (See Section 1.3). To study the mechanistic steps involved in this reaction, first one has to determine the precursor complex which should initiate the reaction. The main requirement of the precursor complex is that both O_2 and C_6H_6 should be simultaneously adsorbed on the zeolite. Since the Cu center is the strongest reactive site in the zeolite, it is possible to limit the structural variations when searching for a possible precursor complex:

1. The sites at disposal are site II, site III and the slightly displaced cationic sites (I', II', III').
2. In order for O_2 and C_6H_6 to be simultaneously adsorbed, a single Cu center is sufficient where simultaneous adsorption occurs. The O_2 and C_6H_6 could even be located at different Cu centers (at different sites) as long as the distance permits the adsorbates to interact with each other and become activated to perform the reaction.

The “*lone*” adsorptions of O_2 and C_6H_6 provide important electronic and structural information which certainly can contribute to think about the initial geometry of the model precursor complexes.

The following conclusions can be drawn from the Cu–Y zeolite complexes containing a single Al atom:

Conclusions from the interaction of O₂ with Cu(I) in Y zeolite: O₂ is stronger bound to Cu(I) at site III (cf. Table 5.9) than at site II (cf. Table 5.8). Site III adsorption complexes show side-on bonded O₂, whereas at site II, O₂ prefers to bind Cu from end-on.

Conclusions from the interaction of C₆H₆ with Cu(I) in Y zeolite: C₆H₆ also binds more strongly to site III Cu compared to site II Cu center, both in η^2 -coordination (cf. Tables 5.16 & 5.15).

In the case of “lone” O₂ adsorption at site II, Cu increases its natural charge from 0.85 (0.89 at site III) in bare Cu–complexes to 1.10 (1.20 at site III) in the adsorbed states (see Table 5.7) whereas, C₆H₆ causes a little (~ 0.10) increase in charge of Cu upon adsorption (see Table 5.14). In any case, there is a net flow of electrons from the 3*d* orbital of Cu towards the adsorbates. The larger the electron donation from Cu⁺, the stronger it activates the adsorbed molecule by π -back donation.

Previous studies [1, 2, 103, 149] have shown that the most important adsorption sites in Cu–Y zeolite are sites II and III. Evidently, Cu(I) is bound stronger at site II than at site III. As a consequence, site III is more flexible towards the uptake of external molecules. All these observations point towards site III being the most important site for the reaction to happen on. Datka et al. [150] studied the co-adsorption of organic molecules (alkenes, acetylene, benzene, acetone) and CO with Cu⁺ sites in Cu–zeolites (X, Y, ZSM-5) using IR spectroscopy. They reported that there are Cu⁺ centers, which are able to bind simultaneously to both organic molecules and CO at relatively high CO pressure. In another theoretical study, Kozyra and Datka [151] had suggested that the co-adsorption of NO together with organic molecules (acetone, formaldehyde, ethene, acetylene) on the same Cu⁺ site of CuZSM-5 zeolite was possible. Simultaneous adsorption of O₂ and C₆H₆ on the same Cu⁺ center at both sites II and III of Y zeolite is investigated in the present work.

6.2 Geometries

6.2.1 Van der Waals Complexes at Sites II and III

TABLE 6.1: Selected geometrical parameters of vdW complexes at sites II & III (6T cluster & 8T cluster) in triplet electronic state: Cu–O (framework) coordination and bond lengths (Å).

Site	R_{Cu-O}	$R_{Cu-O'}$	$R_{Cu-O''}$	$R_{O'-O''}$	$R_{C-O'(O'')}$	R_{C1-C2}	${}^a\sigma_{C-C}$	${}^b\pi_{C-C}$	R_{Cu-C1}	R_{Cu-C2}
II/1 Al/Dioxygen ^c	O2 (1.978, 2.321, 2.435)	1.852	2.755	1.266	> 3.0					
II/1 Al/Benzene ^c	O2 (2.074, 2.342, 2.460)			1.227	> 3.0	1.431	1.419	1.389	2.077	2.079
III/1 Al/Benzene ^c	O1 (2.021); O4 (2.116)			1.229	> 3.0	1.434	1.422	1.390	2.058	2.016

^a σ_{C-C} is the average bond length of R_{C2-C3} , R_{C4-C5} , R_{C6-C1} .

^b π_{C-C} is the average bond length of R_{C3-C4} , R_{C5-C6} .

^c directly connected to Cu center.

For computing the van der Waals complexes the BP86-D density functional [152, 153] was used for the QM calculations within the QM/MM framework.

Site II: In the present work, “simultaneous” adsorption complexes at site II contain only one Al atom per unit cell. At site II, van der Waals complexes are formed due to the adsorption of both adsorbates simultaneously. There is no direct concurrent attachment of both molecules to the Cu center. One of the molecules is attached directly to the Cu center, and the other one just stays on top of the attached one. Thus two types of van der Waals complexes are obtained:

1. complexes which show a direct O₂ to Cu coordination and C₆H₆ resides on top it (cf. Fig. 6.1 [A])
2. complexes which show a direct C₆H₆ to Cu coordination and O₂ resides over it (cf. Fig. 6.1 [B]).

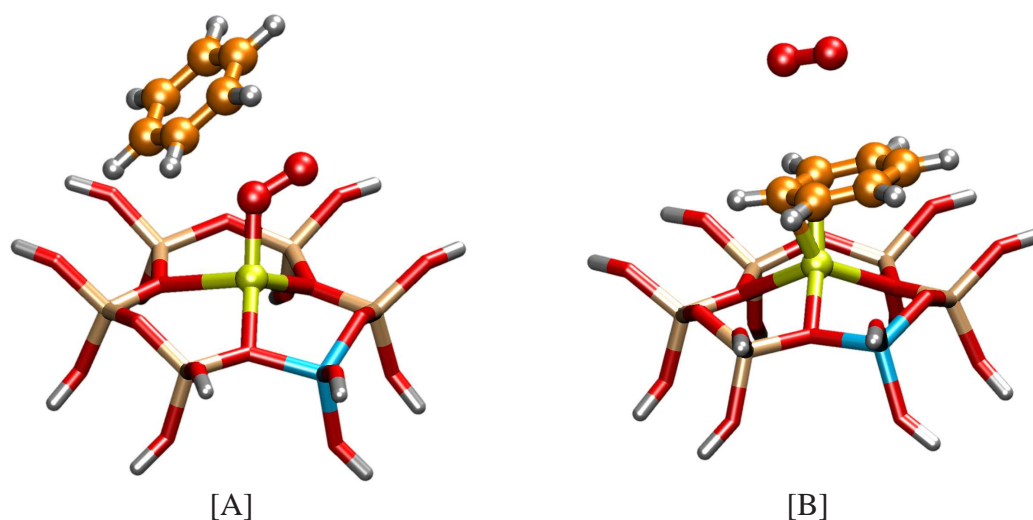


FIGURE 6.1: Quantum mechanically treated part of vdW complexes at site II (modelled by 6T cluster): [A] direct connection of O₂ to Cu, [B] direct connection of C₆H₆ to Cu. [B] is ~ 12 kcal mol⁻¹ lower in energy than [A].

It is evident from Table 6.1 that in both types of complexes, Cu(I) increases its coordination to zeolite-oxygen from two-fold in “lone” O₂ or C₆H₆ adsorption complexes to three-fold in vdW complexes. When O₂ is directly connected to the Cu center (see Fig. 6.1 [A]), the O'–O'' bond distance is similar to that of “lone” adsorption complex, and it still sustains its end-on bonding. In this case, the C₆H₆ behaves very much like a gas-phase entity. On the other hand when C₆H₆ is directly attached to Cu, benzene is coordinated with hapticity 2 (η^2 -C₆H₆). In this case, O₂ behaves as a free gas-phase

molecule (population analysis: the spin density on each O of O₂ is ~ 1 , see Table 6.2). In both types, the mutual distance between two molecules is $> 3.0 \text{ \AA}$.

The only notable difference between “*lone*” adsorption complexes and vdW “*simultaneous*” adsorption complexes is that Cu to oxygen (framework) coordination is two-fold in case of “*lone*” and three-fold in case of “*simultaneous*” adsorption. This may be an overestimation of the dispersive energy correction of the BP86-D functional. I performed single-point energy calculation at the BP86/TZVP level using the BP86-D/TZVP optimized geometries to estimate on the dispersive energy correction. I found that the $\Delta E(\text{BP86} - \text{BP86-D})$ values are 52.3, and 63.7 kcal mol⁻¹ for the [A], and [B] “*simultaneous*” adsorption complexes, respectively. This clearly tells that the dispersive energy correction can change the energy profile significantly.

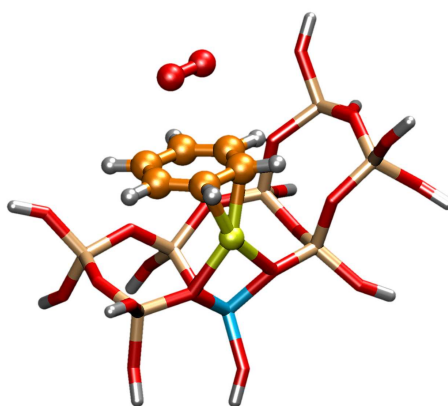


FIGURE 6.2: Quantum mechanically treated part of a vdW complex at site III (modelled by 8T cluster): direct connection of C₆H₆ to Cu.

Site III: In the vdW complex (cf. Fig. 6.2) formed at site III, C₆H₆ is directly connected to Cu, and O₂ remains on top of C₆H₆. The coordination number (see Table 6.1) with respect to the framework oxygen atoms is the same as in the case of “*lone*” O₂ or C₆H₆ adsorption complexes.

Population analysis results given in Table 6.2 do not show any significant change in comparison with “*lone*” adsorptions (Tables 5.7 & 5.14). All these findings show that the interaction between C₆H₆ and O₂ is rather small, *i.e.*, they are not able to activate each other. In this type of vdW complexes, instead of activating each other, the activity of one decreases in presence of another.

At site III, I do not find any vdW complex where O₂ shows a direct coordination to Cu and C₆H₆ resides over O₂.

TABLE 6.2: Population analysis results for different vdW adsorption complexes of sites II and III.

Adsorption site	Atom/molecule	Charges	Orbital	Population	Spin density
Bare Cu–complex					
II	Cu	0.85	4s	0.25	
			3d	9.89	
III	Cu	0.89	4s	0.17	
			3d	9.92	
O ₂ directly connected to Cu–complex					
II	Cu	1.09	4s	0.26	0.32
			3d	9.64	
	O'	-0.24	2s	1.81	0.67
			2p	4.42	
	O''	-0.04	2s	1.84	0.87
2p			4.20		
	C ₆ H ₆	0.02			
C ₆ H ₆ directly connected to Cu–complex					
II	Cu	0.96	4s	0.24	0.01
			3d	9.79	
	O'	-0.02	2s	1.83	0.97
			2p	4.18	
	O''	0.00	2s	1.83	0.99
2p			4.17		
	C ₆ H ₆	-0.10			
III	Cu	0.97	4s	0.28	0.02
			3d	9.74	
	O'	-0.02	2s	1.83	0.97
			2p	4.18	
	O''	-0.02	2s	1.83	0.97
2p			4.17		
	C ₆ H ₆	-0.08			

6.2.2 Co-adsorption of O₂ and C₆H₆ at the Same Cu⁺ Center

While either C₆H₆ or O₂ is directly attached to Cu⁺ in vdW complexes, there are complexes where both the adsorbates are connected to the same Cu center (Fig. 6.3), and energetically with higher relative stabilities.

Nomenclature of the “simultaneous” adsorption complexes of O_2 and C_6H_6 at the same Cu^+ center: When C_6H_6 is oriented towards (closest to) the zeolite framework, the complex is referred to as *endo*-complex, and when C_6H_6 is oriented away from (farthest to) the zeolite framework, the complex is referred to as *exo*-complex. For an illustration see Fig. 6.3, where each of the *endo*- and *exo*-complexes contains only 1 Al atom in its QM fragment.

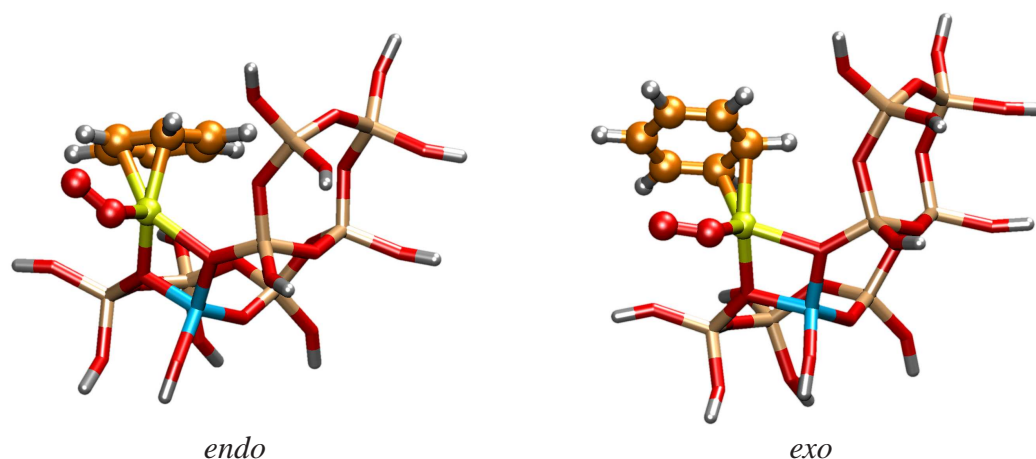


FIGURE 6.3: Quantum mechanically treated part of “simultaneous” adsorption complexes at site III (modelled by 8T cluster) of Cu–Y zeolite: *endo*, *exo*.

6.2.2.1 Endo-Complexes

Cu–O coordination number: Table 6.3 shows detailed information of the geometrical parameters concerning the *endo*-“simultaneous” adsorption complexes for the triplet cluster containing one and two Al atoms in the unit cell of Cu–exchanged Y zeolite. For comparison, the corresponding structural parameters of clusters with “lone” dioxygen or benzene can be seen from Tables 5.6 & 5.13. The Cu–O coordination number is two-fold. However, in O_2 “lone” adsorption complexes, two symmetric Cu–O bonds are observed (Table 5.6), and in the “simultaneous” adsorption complexes two asymmetric Cu–O bond lengths ($\sim 2.0 \text{ \AA}$ and $\sim 2.2 \text{ \AA}$) are observed. This is surprisingly similar to those of “lone” benzene adsorption complexes (Table 5.13).

Changes in O_2 : The most prominent change with respect to the cluster containing “lone” dioxygen as an adsorbate is the change of a side-on coordination in favor of an end-on coordination. Thus, O_2 in “simultaneous” adsorption environment behaves like end-on O_2 in “lone” adsorption complexes of site II (Table 5.5) only, the $O'-O''$

bond length in O₂ decreases as compared to the corresponding “*lone*” dioxygen adsorption complexes. Cu–O’ bond lengths are still equivalent to “*lone*” dioxygen adsorbed complexes at site III.

Changes in benzene: The bonding pattern of benzene is η^2 . In this case the Cu–C bond distance is longer when compared to “*lone*” benzene adsorbed complexes by ~ 0.2 Å. C1–C2 (the distance between the C atoms of benzene that are directly connected to Cu), σ (C–C), and π (C–C) are basically the same as in the case of complex with single adsorbed benzene.

6.2.2.2 *Exo-Complexes*

In this section the *exo*-“*simultaneous*” adsorption complexes are discussed (Fig. 6.3, Table 6.5). The *exo*-“*simultaneous*” adsorption complexes look quite similar to the *endo* ones. Here too, O₂ is end-on, and C₆H₆ is η^2 -coordinated to Cu⁺. There is probably *flipping* or *rotation* of the C₆H₆ ring either in the *endo*- or *exo*-complex, which causes the change in the topology of the C₆H₆ ring near the Cu center.

The two C atoms that are directly connected to Cu and the two C atoms that are far from the Cu center in the *endo*-complex exchange their positions in the *exo*-complex (Fig. 6.3 *endo* and *exo*). This is the only considerable difference between the *endo*- and the *exo*-“*simultaneous*” adsorption complexes.

The *exo*-“*simultaneous*” adsorption complexes behave like the *endo* ones considering the two-fold Cu–O coordination, end-on O₂ and η^2 -benzene binding pattern to Cu. However, there are some minute differences in bond lengths which are discussed below.

Cu–O Coordination number: Here Cu is two-fold coordinated to the framework oxygens. However, in contrast to O₂ “*lone*” adsorption complexes, two asymmetric Cu–O bond lengths are observed in various “*simultaneous*” adsorption complexes – with ranges 2.0 – 2.1 Å, and 2.2 – 2.3 Å. This situation is quite similar to those of *endo*-“*simultaneous*” adsorption complexes, and “*lone*” benzene adsorption complexes (Table 5.13).

TABLE 6.3: Selected geometrical parameters of *endo*-“*simultaneous*” adsorption complexes (with 1 Al and 2 Al atoms) of site III in triplet electronic state: bond lengths (Å) and bond angles.

Isomers	2 nd Al atom replaces	H atom is connected to	R _{Cu-O'}	R _{Cu-O''}	R _{O'-O''}	∠Cu - O' - O''	H ^c - O''	R _{Cu-O}
1 Al	–	–	1.978	2.882	1.262	124.1	2.618	O1 (2.053); O4(2.207)
A	Si2	O1a	1.980	2.872	1.258	123.5	2.829	O1 (1.983); O4(3.405)
B	Si2	O2a	1.989	2.887	1.260	123.8	2.591	O1 (2.071); O4(2.127)
C	Si3	O2a	1.966	2.865	1.264	123.6	2.652	O1 (2.044); O4(2.250)
D	Si3	O1b	2.043	2.932	1.255	123.7	2.609	O1 (2.047); O4(2.200)
E	Si4	O1b	1.966	2.871	1.263	124.0	2.613	O1 (2.054); O4(2.194)
F	Si4	O3a	1.965	2.860	1.262	123.4	2.750	O1 (2.021); O4(2.365)
G	Si4	O4b	2.013	2.904	1.258	123.6	2.573	O1 (2.111); O4(2.126)
H	Si6	O1c	1.996	2.894	1.261	123.8	2.607	O1 (2.030); O4(2.221)
I	Si6	O2b	1.985	2.885	1.260	124.0	2.649	O1 (2.137); O4(2.176)

Isomers	2 nd Al atom replaces	H atom is connected to	R _{C1-C2}	^a σ _{C-C}	^b π _{C-C}	Cu - C1	Cu - C2	C1 - O''	C2 - O''
1 Al	–	–	1.424	1.413	1.392	2.208	2.137	3.303	3.627
A	Si2	O1a	1.426	1.413	1.395	2.178	2.121	4.271	3.367
B	Si2	O2a	1.424	1.413	1.392	2.218	2.117	3.288	3.653
C	Si3	O2a	1.425	1.412	1.393	2.228	2.132	3.333	3.685
D	Si3	O1b	1.427	1.415	1.390	2.137	2.129	3.289	3.518
E	Si4	O1b	1.422	1.412	1.392	2.245	2.131	3.283	3.569
F	Si4	O3a	1.425	1.412	1.393	2.205	2.150	3.369	3.546
G	Si4	O4b	1.425	1.414	1.391	2.163	2.131	3.303	3.895
H	Si6	O1c	1.425	1.411	1.392	2.179	2.138	3.276	3.497
I	Si6	O2b	1.425	1.411	1.392	2.214	2.115	3.337	3.788

^a σ_{C-C} is the average bond length of R_{C2-C3}, R_{C4-C5}, R_{C6-C1}.

^b π_{C-C} is the average bond length of R_{C3-C4}, R_{C5-C6}.

^c this H atom of benzene is the nearest to the dioxygen.

Changes in O₂: Both the Cu–O' and Cu–O'' bonds are systematically shorter than in the *endo*-“*simultaneous*” adsorption complexes – with ranges 0.02 – 0.09 Å and 0.02 – 0.08 Å, respectively. End-on bonded O₂ has similar O'–O'' bond lengths in both *endo*- and *exo*-“*simultaneous*” adsorption complexes.

Changes in benzene: Benzene is bonded to Cu in η^2 -fashion. The Cu–C bond distance is longer as compared to the “*lone*” benzene adsorbed complexes by ~ 0.2 Å. The C1–C2 (the directly connected C atoms of benzene to Cu), σ (C-C), and π (C-C) distances are basically the same as in the singly benzene adsorbed complex.

TABLE 6.4: Population analysis for “*simultaneous*” adsorption complexes (*endo* & *exo*) containing 1 Al at site III compared with “*lone*” adsorption complexes.

Complex	Atom/ molecule	Charges	Occupation	Spin density
Bare	Cu	0.89	3d ^{9.92} 4s ^{0.17}	0.0
O ₂	Cu	1.20	3d ^{9.51} 4s ^{0.27}	0.53
	O'	-0.20	2s ^{1.86} 2p ^{4.33}	0.72
	O''	-0.20	2s ^{1.86} 2p ^{4.34}	0.70
C ₆ H ₆	Cu	0.96	3d ^{9.74} 4s ^{0.29}	
	C ₆ H ₆	-0.10		
<i>Endo</i> - complex	Cu	1.11	3d ^{9.61} 4s ^{0.25}	0.31
	O'	-0.17	2s ^{1.82} 2p ^{4.34}	0.74
	O''	-0.08	2s ^{1.84} 2p ^{4.24}	0.85
	C ₆ H ₆	0.00		
<i>Exo</i> - complex	Cu	1.10	3d ^{9.63} 4s ^{0.25}	0.29
	O'	-0.18	2s ^{1.82} 2p ^{4.35}	0.74
	O''	-0.05	2s ^{1.84} 2p ^{4.21}	0.87
	C ₆ H ₆	-0.01		

Population analysis (Table 6.4) shows in a net flow of electron density from Cu mainly to O₂ in the “*simultaneous*” adsorption process. The Cu 3d hole is larger than in the “*lone*” C₆H₆ adsorption complex, but smaller than in the “*lone*” O₂ case. The spill-out of spin density from 2p orbital of O₂ towards 3d orbital of Cu occurs. Population analyses of different isomers are given in Appendices C.6 & C.7.

TABLE 6.5: Selected geometrical parameters of *exo*-“*simultaneous*” adsorption complexes (with 1 Al and 2 Al atoms) of site III in triplet electronic state: bond lengths (Å) and bond angles.

Isomers	2 nd Al atom replaces	H atom is connected to	R _{Cu-O'}	R _{Cu-O''}	R _{O'-O''}	∠Cu - O' - O''	H ^c - O''	R _{Cu-O}
1 Al	–	–	1.962	2.855	1.259	123.4	3.688	O1 (2.052); O4(2.226)
A	Si2	O1a	1.950	2.827	1.258	122.1	3.445	O1 (1.983); O4(3.395)
B	Si2	O2a	1.960	2.865	1.259	124.3	3.682	O1 (2.053); O4(2.232)
C	Si3	O2a	1.949	2.842	1.260	123.2	3.619	O1 (2.045); O4(2.249)
D	Si3	O1b	1.954	2.848	1.258	123.4	3.701	O1 (2.023); O4(2.327)
E	Si4	O1b	1.953	2.856	1.260	124.1	3.669	O1 (2.045); O4(2.224)
F	Si4	O3a	1.954	2.845	1.259	123.1	3.660	O1 (2.036); O4(2.350)
G	Si4	O4b	1.964	2.873	1.258	124.7	3.552	O1 (2.096); O4(2.179)
H	Si6	O1c	1.929	2.826	1.263	123.2	3.671	O1 (2.014); O4(2.325)
I	Si6	O2b	1.952	2.858	1.259	123.4	3.641	O1 (2.107); O4(2.226)

Isomers	2 nd Al atom replaces	H atom is connected to	R _{C4-C5}	^a σ _{C-C}	^b π _{C-C}	Cu - C4	Cu - C5	C1 - O''	C2 - O''
1 Al	–	–	1.423	1.413	1.391	2.189	2.154	3.364	3.321
A	Si2	O1a	1.425	1.413	1.394	2.214	2.141	4.089	4.809
B	Si2	O2a	1.423	1.412	1.391	2.152	2.201	3.309	3.312
C	Si3	O2a	1.423	1.414	1.391	2.184	2.179	3.385	3.292
D	Si3	O1b	1.414	1.412	1.391	2.174	2.179	3.334	3.349
E	Si4	O1b	1.423	1.412	1.391	2.174	2.187	3.298	3.308
F	Si4	O3a	1.424	1.412	1.392	2.173	2.172	3.322	3.369
G	Si4	O4b	1.424	1.412	1.391	2.152	2.198	3.230	3.424
H	Si6	O1c	1.422	1.412	1.391	2.203	2.194	3.374	3.308
I	Si6	O2b	1.423	1.412	1.391	2.161	2.210	3.341	3.293

^a σ_{C-C} is the average bond length of R_{C1-C2}, R_{C3-C4}, R_{C5-C6}.

^b π_{C-C} is the average bond length of R_{C2-C3}, R_{C1-C6}.

^c this H atom of benzene is the nearest to the dioxygen.

All these data indicate that “*simultaneous*” adsorption complexes of both benzene and dioxygen molecules show much more similarities to the “*lone*” benzene adsorption complexes than to the “*lone*” dioxygen adsorption complexes (except the structural parameters which are related to dioxygen). Probably the most important finding is that the second Al atom does not bring dramatic changes into the adsorbate–adsorbent interaction.

6.3 Energies

6.3.1 Energies of the *Endo-Complexes*

Three sets of geometry optimizations are performed for the different electronic states such as triplet, closed-shell singlet and broken-symmetry singlet states. For each electronic state, the number and the position of aluminum atoms and of the corresponding charge-conserving protons are varied. This resulted in a total of 27 structures which are summarized in Table 6.6. Consequently, the most relevant structure of this study appears to be cluster C, in which the the additional proton is connected to an O2 type oxygen (cf. Table 6.6). Cluster H is still very close in energy (within 1 kcal mol⁻¹), while all other systems are off by at least 2.0 kcal mol⁻¹. These results appear to be independent of the electronic state: structure C is the minimum, which is the lowest in energy for the closed-shell and broken-symmetry singlet states.

The binding energy is computed according to Eq. 6.1. In all the cases, the binding energy of the clusters in the triplet state are significantly lower than the corresponding closed-shell singlet state species.

$$E_b^i(C_6H_6 + O_2) = E^i(\text{co-adsorption}) - E(\text{without adsorption}) \\ - E_{free}^{triplet}(O_2) - E_{free}^{singlet}(C_6H_6) \quad (6.1)$$

In Eq. 6.1 *i* refers to each electronic state: triplet, singlet and broken-symmetry singlet. The binding energy of the broken-symmetry singlet states is always close to the triplet states. A significant admixture of triplet contributions to the singlet states is observed. However, these results support the principal restriction to triplet states, and thus, further considerations focus exclusively on triplet state calculations. This is in line with the

high-level benchmark calculations (cf. Section 4.5) at the coupled-cluster and multi-reference configuration interaction level [2].

TABLE 6.6: Co-adsorption of O₂ and C₆H₆ at site III in Cu–Y zeolites (8T QM cluster model): relative stabilities (E_{rel}) of different adsorption complexes, and binding energies (E_b) of (C₆H₆+O₂) in *endo*-complexes. The result in the first line refers to the case of 1 Al–complex, and the others to the various isomers containing 2 Al atoms. All the quantities are given in kcal mol⁻¹.

Isomers	2 nd Al atom replaces	H atom is connected to	Triplet		BS Singlet		Singlet	
			E_{rel}	E_b	E_{rel}	E_b	E_{rel}	E_b
1 Al	-	-	-37.0		-31.0		-15.8	
A	Si2	O1a	5.9	-44.6	6.1	-38.6	5.3	-24.9
B	Si2	O2a	2.2	-35.6	2.5	-29.6	3.4	-14.0
C	Si3	O2a	0.0	-38.5	0.0	-32.7	0.0	-18.2
D	Si3	O1b	6.8	-36.6	7.3	-30.3	9.2	-13.9
E	Si4	O1b	9.6	-34.4	9.7	-28.6	10.1	-13.6
F	Si4	O3a	28.3	-38.3	28.3	-32.5	28.9	-17.3
G	Si4	O4b	10.9	-36.1	11.2	-29.9	12.4	-14.2
H	Si6	O1c	0.6	-36.7	0.7	-30.7	1.1	-15.7
I	Si6	O2b	2.0	-38.6	2.3	-32.5	3.6	-16.7

6.3.2 Energies of the *Exo*-Complexes

The *exo*-“*simultaneous*” adsorption complexes are also computed for the three electronic states – singlet, broken-symmetry singlet, and triplet states (Table 6.7). All these calculations were performed by following the same procedure as in the case of the *endo*-“*simultaneous*” adsorption complexes. The open-shell triplet states are always the lowest energy states, and the closed-shell singlet ones are the highest ones whereas the broken-symmetry singlet electronic states are again closely related to the triplet ones. Therefore, again the behavior of the *exo*-“*simultaneous*” adsorption complexes is found similar to the *endo* ones. The relative energies of different isomers vary in the same order as in case of “*lone*” dioxygen *or* benzene adsorption complexes. Considering the relative energies of the different isomers, the *exo*-“*simultaneous*” adsorption complexes differ very little from the *endo* ones. Here, the most stable complex is isomer H (it was C for *endo*). Although isomers B, C, H are again within 1.7 kcal mol⁻¹ – this situation is again in line with the observations made in the case of *endo*- “*simultaneous*” adsorption complexes.

Binding energies are calculated according to Eq. 6.1. The most stable “*simultaneous*” adsorption complex H has a binding energy of $-36 \text{ kcal mol}^{-1}$ in the triplet state.

Endo- vs. exo-“*simultaneous*” adsorption 1Al-complex: In the triplet (broken-symmetry singlet) state, the *exo*-“*simultaneous*” adsorption complex is 0.6 (0.9) kcal mol^{-1} higher in energy than the *endo*-complex. But, in the singlet state, the *endo*-“*simultaneous*” adsorption complex is 4.5 kcal mol^{-1} higher in energy than the *exo*-complex. In any case the triplet states are always the lowest energy states for both *endo*- and *exo*-complexes.

TABLE 6.7: Co-adsorption of O_2 and C_6H_6 at site III in Cu–Y zeolites (8T QM cluster model): relative stabilities (E_{rel}) of different adsorption complexes, and binding energies (E_b) of ($\text{C}_6\text{H}_6+\text{O}_2$) in *exo*-complexes. The result in the first line refers to the case of 1 Al-complex, and the others to the various isomers containing 2 Al atoms. All the quantities are given in kcal mol^{-1} .

Isomers	2 nd Al atom replaces	H atom is connected to	Triplet		BS Singlet		Singlet	
			E_{rel}	E_b	E_{rel}	E_b	E_{rel}	E_b
1 Al	-	-		-36.3		-30.2		-20.4
A	Si2	O1a	6.3	-43.4	8.1	-37.2	5.8	-27.5
B	Si2	O2a	0.8	-36.2	2.6	-30.0	1.1	-19.5
C	Si3	O2a	1.7	-36.1	3.4	-29.9	1.3	-20.0
D	Si3	O1b	6.7	-35.9	8.5	-29.7	4.5	-21.6
E	Si4	O1b	8.7	-34.6	10.4	-28.4	6.8	-20.1
F	Si4	O3a	16.8	-48.9	18.6	-42.8	28.3	-21.1
G	Si4	O4b	9.9	-36.3	11.7	-30.1	12.2	-17.5
H	Si6	O1c	0.0	-36.4	0.0	-32.0	0.0	-20.0
I	Si6	O2b	2.3	-37.6	4.0	-31.4	4.5	-18.9

6.4 Frequencies

6.4.1 Frequencies of the *Endo*-Complexes

Harmonic frequencies are calculated for the “*simultaneous*” adsorption complexes in the triplet state. In Table 6.8 the computed ν_{O-O} of O_2 and ν_{13} of benzene are tabulated. In the following section, the changes that occur in the O_2 stretching and C–C stretching (ν_{13}) vibrations due to the adsorption of both the adsorbates simultaneously to the same Cu^+ center at site III are discussed in detail.

TABLE 6.8: “Simultaneous” adsorption of C₆H₆ and O₂ at site III of Cu–Y zeolite: *endo*-complexes. Comparison of the experimental and calculated harmonic frequencies ν/cm^{-1} , frequency shifts $\Delta\nu/cm^{-1}$ of benzene and O₂ in gas-phase and adsorbed state. Geometries and analytic force constants are calculated at BP86/TZVP level; within the RI-*J* approximation. Scaling factors are 1.012 and 1.02 for C₆H₆ and O₂, respectively.

	C ₆ H ₆		O ₂	
	ν_{13} (C-C ring stretch)	$-\Delta\nu_{13}^a$	ν_{O-O} (O-O stretch)	$-\Delta\nu_{O-O}^c$
Exp/Free	1484 ^b		1556	
Calc/Free	1489		1556	
Site III				
Calc/Cu-1Al	1473/1471	16/18	1335	221
Calc/Cu-2Al				
A	1473/1469	16/20	1345	211
B	1473/1470	16/19	1341	215
C	1476/1473	13/16	1329	227
D	1473/1467	16/22	1359	197
E	1474/1471	15/18	1330	226
F	1474/1472	15/17	1334	222
G	1472/1468	17/21	1350	206
H	1472/1469	17/20	1337	219
I	1472/1471	17/18	1343	213

^a $\Delta\nu$ is the frequency shift of benzene from the gas-phase to the adsorbed state.

^b Taken from Ref. [137].

^c $\Delta\nu_{o-o}$ is the frequency shift of O₂ from the gas-phase to the adsorbed state.

O₂ stretching mode (ν_{O-O}): The value of the gas-phase O₂ stretching mode vibration is 1556 cm⁻¹ [119]. In the present case the O₂ stretching mode vibration lies in the range of 1330 to 1359 cm⁻¹ depending on the aluminum distribution patterns in all the “simultaneous” adsorption complexes. Thus a down-shift of 197 – 227 cm⁻¹ with respect to free dioxygen in the gas phase is obtained. In end-on “lone” O₂ adsorption complexes of site II, the down-shift lies between 232 – 296 cm⁻¹. This reveals that the interaction of O₂ with Cu⁺ in the “simultaneous” adsorption is slightly weaker than in the case of “lone” O₂ adsorption where end-on coordination of O₂ is observed.

C–C stretching mode (ν_{13}): In free benzene, the computed value of the degenerate ν_{13} mode is at 1489 cm⁻¹. The degeneracy of this IR inactive mode is lifted by the symmetry-breaking due to the adsorption process, which should result in certain IR activity. Consequently, symmetry splitting of the degenerate ring stretching mode may arise, which should be seen in calculations. Indeed, the calculated values (cf. Table

6.8) show a pair of transitions for the ν_{13} mode (see Table 6.8). One ranges from 1472 to 1476 cm^{-1} and the other from 1467 to 1472 cm^{-1} , thereby causing a down-shift of 13 – 17 cm^{-1} (for the other one from 16 – 22 cm^{-1}) with respect to the calculated gas-phase value. All these results show that frequency shifts in benzene are lowered in the case of “*simultaneous*” adsorption than in the case of “*lone*” C_6H_6 adsorption [1]. Even the maximum splitting of this degenerate mode is only 6 cm^{-1} (for isomer D), and the minimum is 1 cm^{-1} (for isomer I) – which are lower than that of “*lone*” C_6H_6 adsorption.

All these facts indicate that both the molecules are activated in the “*simultaneous*” adsorption environment although not as strong as in the case of “*lone*” adsorption. Nevertheless, one would expect so. Since now two molecules simultaneously have to be bonded to the same Cu center overcoming the steric and electronic effects; even the size of the pore matters whether the reactant selectivity criterion (see Section 3.1) has been satisfied or not. However, in these “*simultaneous*” adsorption complexes, the O_2 stretching mode is more sensitive than the C–C stretching mode of benzene with respect to the topology around the Cu center.

6.4.2 Frequencies of the *Exo*-Complexes

The harmonic frequencies of the *exo*-complexes are calculated for the optimized geometries of the “*simultaneous*” adsorption complexes in the triplet state, as in the case of the *endo*-complexes. Table 6.9 shows the values of computed $\nu_{\text{O}-\text{O}}$ mode of O_2 and the C–C ring stretching ν_{13} mode of benzene. The fact that the geometrical and energetic parameters of the *exo*-“*simultaneous*” adsorption complexes do not differ much from the *endo* ones is reflected in the harmonic frequencies. Consequently, harmonic frequencies do not deviate much. Here the focus is on the comparison of the O_2 and C–C stretching vibrations of benzene in the *exo*- and *endo*-complexes.

O_2 stretching mode ($\nu_{\text{O}-\text{O}}$): Here the most stable “*simultaneous*” adsorption complex is isomer H which shows an O_2 stretching mode at 1330 cm^{-1} , which is quite similar to the most stable “*simultaneous*” adsorption complex (isomer C) of the *endo* type. In other cases, O_2 stretching modes show up at 1341 – 1348 cm^{-1} . Table 6.9 results show a down-shift of 208 – 226 cm^{-1} in O_2 stretching vibration in various “*simultaneous*” adsorption complexes with respect to free dioxygen in the gas phase which are even, much less down-shifted than the “*lone*” adsorption case of O_2 . The major difference

TABLE 6.9: “Simultaneous” adsorption of C_6H_6 and O_2 at site III of Cu–Y zeolite: *exo*-complexes. Comparison of the experimental and calculated harmonic frequencies ν/cm^{-1} , frequency shifts $\Delta\nu/cm^{-1}$ of benzene and O_2 in gas-phase and adsorbed state. Geometries and analytic force constants are calculated at BP86/TZVP level; within the RI-*J* approximation. Scaling factors are 1.012 and 1.02 for C_6H_6 and O_2 , respectively.

	C_6H_6		O_2	
	ν_{13} (C-C ring stretch)	$-\Delta\nu_{13}^a$	ν_{O-O} (O-O stretch)	$-\Delta\nu_{O-O}^c$
Exp/Free	1484 ^b		1556	
Calc/Free	1489		1556	
Site III				
Calc/Cu-1Al	1475/1471	14/18	1346	210
Calc/Cu-2Al				
A	1477/1472	12/17	1346	210
B	1477/1473	12/16	1345	211
C	1477/1473	12/16	1341	215
D	1475/1474	14/15	1348	208
E	1474/1473	15/16	1342	214
F	1476/1473	13/16	1348	208
G	1475/1472	14/17	1348	208
H	1475/1475	14/14	1330	226
I	1481/1474	8/15	1345	211

^a $\Delta\nu$ is the frequency shift of benzene from the gas-phase to the adsorbed state.

^b Taken from Ref. [137].

^c $\Delta\nu_{o-o}$ is the frequency shift of O_2 from the gas-phase to the adsorbed state.

in O_2 stretching vibrations between the *endo*- and *exo*-“simultaneous” adsorption complexes is that, most of the complexes (1 Al-complex, isomers B, C, E, F, I) in the latter case show less down-shifted ν_{O-O} than the *endo* ones which indicates that, the dioxygen molecules in *exo*-“simultaneous” adsorption complexes are less activated than the *endo* ones.

C–C stretching (ν_{13}): The symmetry-breaking of the degenerate ν_{13} mode due to the adsorption process, is also observed for the *exo*-complexes. Table 6.9 shows a pair of transitions for ν_{13} mode for each isomer. One varies from 1474 – 1481 cm^{-1} and the other one from 1471 – 1475 cm^{-1} thereby causing a down-shift of 8 – 15 cm^{-1} (for the other one from 14 – 18 cm^{-1}) with respect to the calculated gas-phase value of ν_{13} mode. All these show that frequency shifts in benzene are lowered in case of “simultaneous” adsorption complexes in comparison to “lone” C_6H_6 adsorption complexes [1]. The maximum splitting of this degenerate mode is only 7 cm^{-1} (for isomer D), and even

the most stable adsorption complex does not show any splitting. The frequency downshift values of ν_{13} decreases here in comparison to the *endo*-“*simultaneous*” adsorption complexes.

Thus all the findings indicate that the activation of both the molecules is quite similar for the *endo*- and *exo*-“*simultaneous*” adsorption complexes. However, which one of them will behave better as reactant complex/precursor complex *or* which one would be effective in predicting the low-barrier reaction pathways in comparison to other is to be addressed in next chapter.

Chapter 7

A Possible Mechanism for the Oxidation of Benzene to Phenol

In the heterogeneous catalysis making use of transition metal ion exchanged zeolites, one of the most widely studied reactions is selective oxidation of hydrocarbons. Such a catalyst has to perform a dual function: on one hand it has to activate the dioxygen and generate a reactive catalyst-bound oxygen species, and on the other hand it has to activate the organic molecule to form the product. In the present study of the oxidation of benzene in Cu–Y zeolite, such an activation is desired, *i.e.*, Cu–Y zeolite has to activate O₂ and C₆H₆ simultaneously. Such types of reactant/precursor complexes which are thought to be the initial activated species have been characterized in the previous chapter. In this chapter, a possible pathway for phenol production will be discussed based on these precursor complexes.

The potential energy surface (PES) of a chemical reaction provides key information about electronic energies and structures of reactants, products, and transition states (TSs). Therefore the determination of the PES of the reaction of interest is needed. The structural parameters of the precursor complexes can be seen from Tables 6.3 & 6.5. The next question would be, how to activate the benzene molecule, in particular the activation of one of the C–H bonds of benzene by the CuO₂⁺ adduct? Most of the transition metal exchanged catalysts produce an oxygen species that carries a negative charge *e.g.* O[−], O^{2−}, O₂[−] and oxidize benzene via an electrophilic reaction mechanism [154]. It is most likely that one of the oxygen atoms in the adsorbed dioxygen will bind

to the nearest C atom of benzene (which is also adsorbed in zeolite to the same Cu center¹ where O₂ is adsorbed). Such an *oxygen-insertion* into the C–H bond of benzene forms a σ -complex, which involves a synchronous O–H bond formation and C–H bond breaking; consequently a phenol-complex is generated. A σ -complex formation for the gas-phase hydroxylation of benzene by bare FeO⁺ was demonstrated by Schröder and Schwarz [155], too. The present investigation conducts a possible mechanistic pathway for the catalytic oxidation of benzene using O₂ over Cu–exchanged Y zeolite.

7.1 QM/MM Partitioning

The *endo*- and *exo-simultaneous* adsorption complexes mentioned in the previous chapter are renamed here, *old* precursor 1 and *old* precursor 2, respectively. Although, the characterization of these precursors has been done in the previous chapter, for performing the QM/MM calculations regarding reaction pathways, a small change has been introduced in the QM cluster. The 2 Si and 5 O atoms (shown in Fig. 7.1/*old* by arrows), which were QM-atoms in the *old* setup, are now treated as MM-atoms, while 2 different Si atoms and 5 different O atoms (shown in Fig. 7.1/*new* by arrows) are now added to the QM part. This leads to a more symmetric environment of the Al atom.

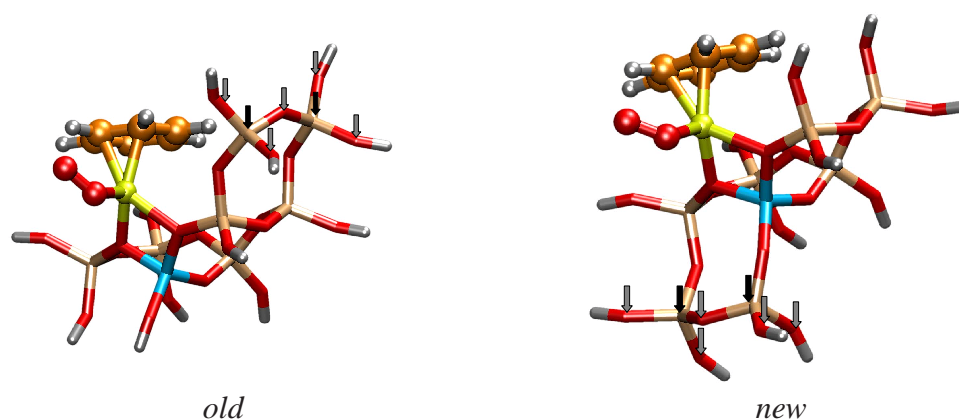


FIGURE 7.1: *old* and *new* QM cluster of precursor complex 1: showing the increment of the cluster size around the AlO₄ tetrahedra.

The geometry and the energetics of the *old* precursor 1 and the *new* precursor 1 are compared in Table 7.1. Both the *old* precursor 1, and the *new* contain the same 8T cluster as the QM cluster for QM/MM computations. The selected structural parameters

¹Benzene and dioxygen may get adsorbed at different active Cu–sites of the zeolite also, as long as they are able to interact with each other.

(See Table 7.1) of both the precursors agree quite satisfactorily with each other. In the present study the active catalytic center is the cuprous ion which is located at the ion-exchangeable Al site (the so-called Brønsted acid site). The *new* QM cluster is symmetric with respect to the Al site. Therefore, the *new* QM cluster will introduce a smaller error due to the truncation of the cluster for the QM/MM embedding, and include all the short range interactions symmetrically between the adsorbed molecules (onto the Cu center) and the zeolite within the inner part. Therefore the *new* QM cluster is considered in the following.

TABLE 7.1: Geometrical parameters (bond distances/Å and angles/°) of the *old* and *new* 8T QM clusters of 1 Al containing precursor complex 1 found at site III; relative energies (E_{rel}), binding energies (E_b) of ($C_6H_6 + O_2$) in kcal mol⁻¹; C1, C2 carbon atoms are directly connected to the Cu center; O' is the terminal oxygen of O₂ and O' is directly coordinated to Cu.

Parameters	<i>Old</i> precursor 1	<i>New</i> precursor 1
R_{Cu-O}	O1 (2.053); O4(2.207)	O1 (2.063); O4(2.192)
$R_{Cu-O'}$	1.978	1.984
$R_{Cu-O''}$	2.882	2.881
$R_{O'-O''}$	1.262	1.260
$\angle Cu - O' - O''$	124.1	123.7
R_{C1-C2}	1.424	1.425
σ_{C-C}	1.413	1.413
π_{C-C}	1.392	1.392
$Cu - C1$	2.208	2.197
$Cu - C2$	2.137	2.129
$C1 - O''$	3.303	3.337
$C2 - O''$	3.627	3.725
$H - O''$	2.618	2.650
E_{rel}	0.0	0.9 ^a
E_b	-37.0	-37.7

^a The relative energy of the *new* precursor 1 is calculated with respect to the *old* precursor 1.

7.2 Optimization and Transition State Search

The QM/MM calculations consist of geometry optimizations for the local minima (intermediates) and saddle points (transition states) along the reaction path for triplet, singlet,

broken-symmetry singlet potential energy surfaces. After each optimization, a vibrational analysis has been performed to confirm the minimum (no imaginary frequency) or the transition state (single imaginary frequency). For transition states, IRC (Intrinsic Reaction Coordinate) calculations were also done in order to verify that the transition states really connect the desired minima (corresponding reactants and products).

Constrained TS search: The conversion of one minimum-energy structure into another may sometimes occur primarily along just one or two coordinates. In such cases, an approximation to the reaction pathway can be obtained by gradually varying the coordinate(s), allowing the system to relax at each step using minimisation while keeping the chosen coordinate(s) fixed. The point of highest energy on the path is an approximation to the saddle point and the structures generated during the course of the calculation can be considered to represent a sequence of points on the interconversion pathway [33]. This approach for locating a transition state on the potential energy surface is known as *constrained* TS search.

In the present study of the oxidation reaction between benzene and dioxygen – as the first step in finding a TS – a *constrained* TS search approach is used. According to the assumption regarding the reaction mechanism stated above, an apparently obvious reaction coordinate would be the distance between the O'' of O₂ and C1 (nearest to O₂) of C₆H₆. The C1–O distance is 3.3 Å in the precursor 1 (Fig. 7.2). Therefore, the C1–O distance was decreased with a step size of ~ 0.1 Å until a region for the formation of the phenol-zeolite complex (Fig. 7.2) was found. For each value of the C1–O distance, an energy minimization is performed by relaxing all the others degrees of freedom. Thus, an energy profile for the constrained search calculation as a function of the reaction coordinate C1–O is obtained (see Fig. 7.3).

TS optimization: The geometries corresponding to the maximum energy region which is marked by a rectangle in Fig. 7.3 are considered for the approximate TS structures. The force constant matrices are computed for these particular structures without any constraints. Then a TS search is performed for each of these geometries by relaxing all the coordinates, using the pre-calculated Hessian matrix following the transition vector (with negative eigenvalue) – the so-called *eigenvector following* method. Among these three geometries, the one which show a C1–O bond length of 1.8 Å finally leads to a TS (TS1 in Fig. 7.5).

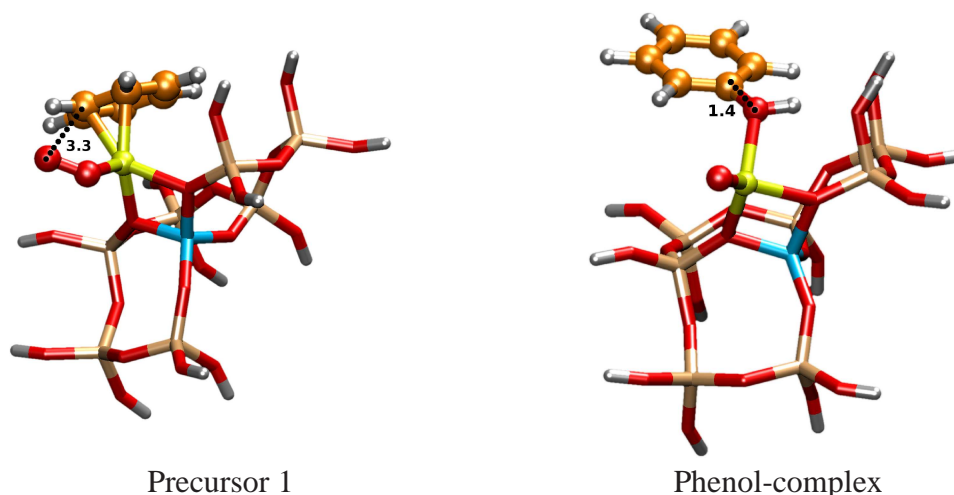
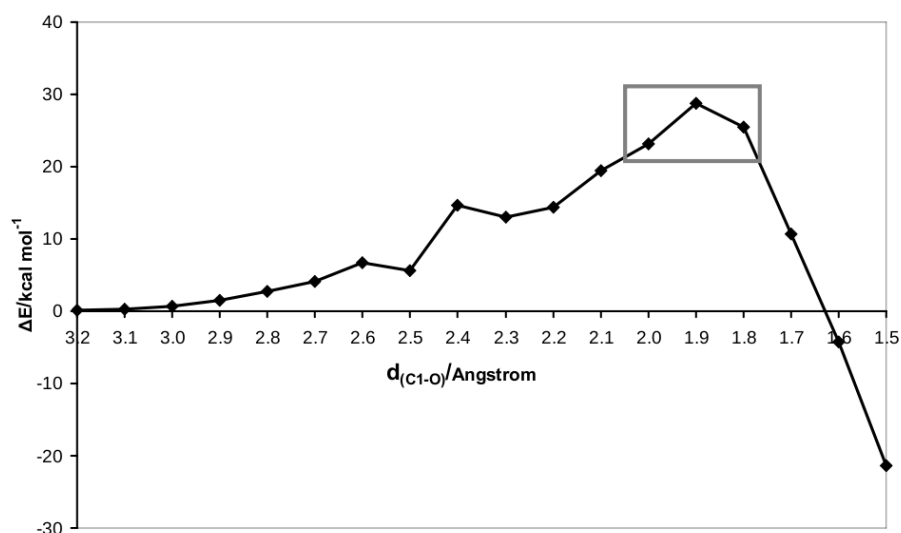


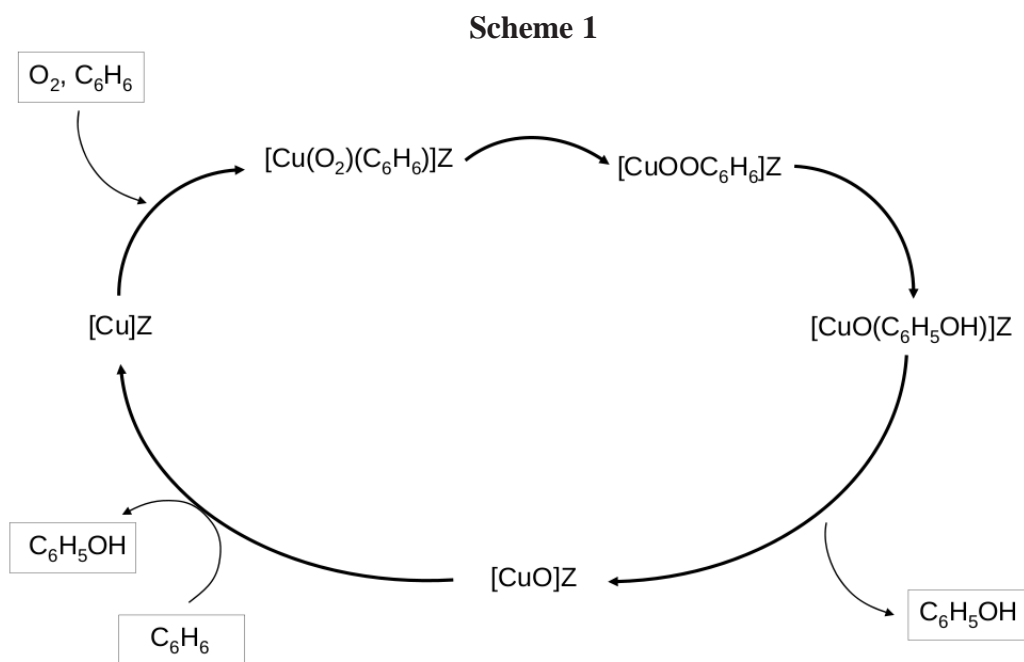
FIGURE 7.2: Precursor 1 and phenol-complex: showing the C1–O bond distance.

FIGURE 7.3: Energy profile as a function of C1–O bond distance for the *constrained* TS search.

Intrinsic reaction coordinate (IRC) calculations have been performed from the TS towards each minima, such as precursor 1 and phenol-complex (see Fig. 7.2). Surprisingly backward IRC calculation leads to another precursor complex (Precursor complex in Fig. 7.5) instead of precursor 1, and forward IRC calculation results in another intermediate (which is found out later as σ -complex in Fig. 7.5) instead of phenol-complex. However, the *constrained* search was started from the precursor 1 and the phenol-complex was obtained too. This indicates that there must be, at least another transition state which will end up with the formation of the phenol-complex. In fact, a TS for the phenol-complex formation has been traced along the pathway (see TS2 in

Fig. 7.5).

7.3 Reaction Mechanism



Z	structure of the ion-exchangable Al site in Y zeolite
$[\text{Cu}(\text{O}_2)(\text{C}_6\text{H}_6)]\text{Z}$	precursor complex
$[\text{CuOOC}_6\text{H}_6]\text{Z}$	σ -complex
$[\text{CuO}(\text{C}_6\text{H}_5\text{OH})]\text{Z}$	phenol-complex
$[\text{CuO}]\text{Z}$	CuO^+ complex

Although several theoretical investigations were carried out concerning the hydroxylation of benzene by various iron-oxo species [17, 155–158], the mechanism of the aerobic oxidation of benzene to phenol in Cu–Y zeolite is still unknown. Therefore, a plausible mechanistic pathway is proposed in the present work. The present mechanistic model for Cu–Y zeolite catalyzed oxidation of benzene at the molecular level is depicted in Scheme 1. In this mechanism, the *simultaneous* adsorption of molecular oxygen and benzene leads to formation of the precursor complex. O-atom insertion from copper-di-oxo species results in the σ -complex which undergoes simultaneous C–H bond cleavage and O–H bond formation to the phenol-complex. The release of

phenol produces the copper-oxo complex². To complete the catalytic cycle a second benzene molecule is added, and eventually the Cu-exchanged Y zeolite is regenerated by the production of phenol.

For the CuO_2^+ moiety the possible electronic states are triplet and singlet states. The broken-symmetry singlet calculations are also performed in order to account for the small singlet-triplet energy separation. The computation of potential energy surfaces for triplet, singlet and broken-symmetry singlet states is a time demanding task for the quantum mechanical calculation within a QM/MM methodology.

7.3.1 Reaction Intermediates and Transition States

The four reaction intermediates and three transition states along the reaction pathways on the triplet potential energy surface are shown in Fig. 7.5. The geometries of the reaction intermediates and the transition states are quite similar for the triplet- and the broken-symmetry singlet spin states.

TABLE 7.2: Geometrical parameters for precursor complex; H atom is the nearest to the terminal oxygen (O'') of O_2 .

	$R_{\text{Cu}-\text{O}'}$	$R_{\text{O}'-\text{O}''}$	$\text{C1}-\text{O}''$	$\text{O}''-\text{H}$	$\angle\text{Cu}-\text{O}'-\text{O}''$
Precursor					
Triplet	1.963	1.257	3.284	3.638	123.9
Bs-singlet	1.933	1.265	3.630	3.270	122.7
Singlet	1.830	1.299	2.344	2.678	123.6

- 1. Precursor complex:** In the computed geometry of the precursor complex, O_2 and C_6H_6 are simultaneously adsorbed to the same Cu center. The precursor complex has η^2 -coordinated benzene to Cu, and the total coordination number around the Cu center is 5 including three copper–oxygen coordinations – one coming from the dioxygen, and the other two from zeolite framework oxygen atoms (see precursor complex in Fig. 7.5). The directly connected carbon atoms of the benzene ring to Cu are denoted as C1 and C2. The two Cu–C1 and Cu–C2 bond lengths are 2.143 and 2.198 Å (2.160 and 2.216 Å) in the triplet state (broken-symmetry singlet state). In the singlet state, only one carbon atom is directly

²The experimental bond dissociation energy value of CuO^+ is $37 \pm 3 \text{ kcal mol}^{-1}$ [155].

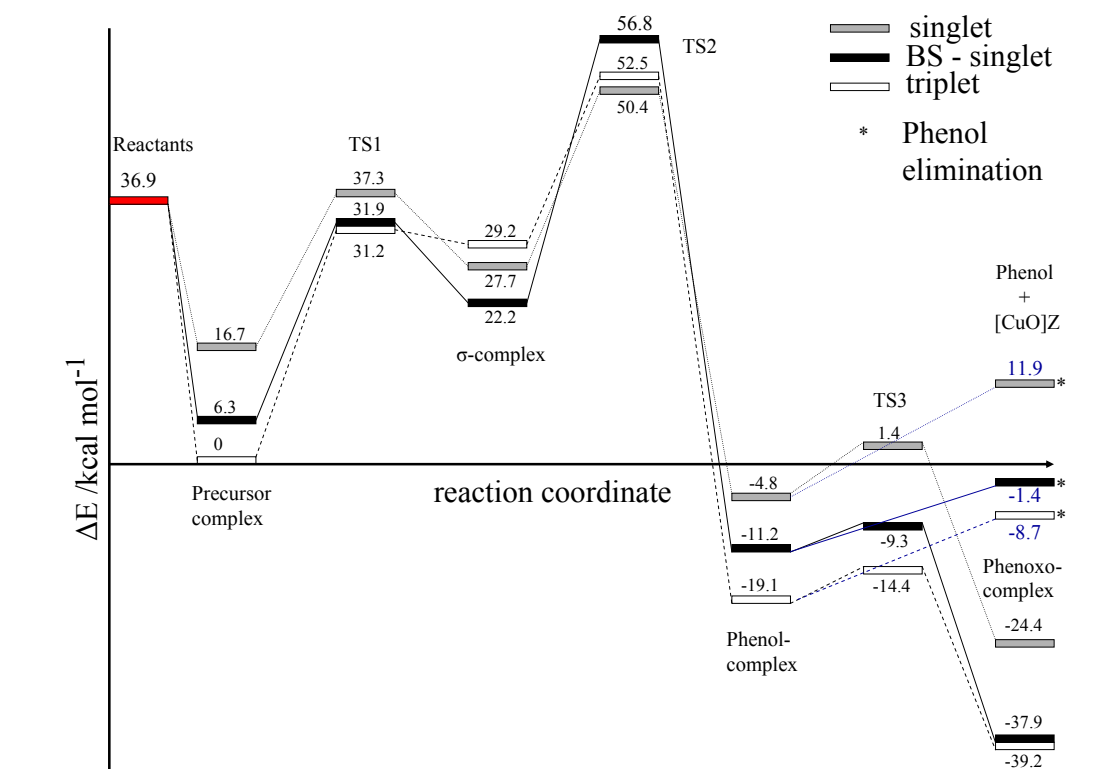


FIGURE 7.4: Potential energy diagrams for the oxidation of benzene to phenol by dioxygen in Cu–Y zeolite in the triplet, singlet, and broken-symmetry singlet states. Relative energies are given in kcal mol⁻¹. Reactants are Cu–Y zeolite (singlet), O₂ (triplet), and C₆H₆ (singlet).

connected to Cu ($R_{Cu-C1} = 2.122 \text{ \AA}$). In the precursor complex, the benzene ring remains nearly planar. The O'–O'' bond distance is about 1.3 \AA (Table 7.2) for the different potential energy surfaces.

2. **TS1:** The first transition state, which connects the precursor complex and the σ -complex, exhibits an imaginary frequency of $132i$, $180i$ and $323i \text{ cm}^{-1}$ in the triplet, broken-symmetry singlet and singlet states, respectively. In TS1 a strong bond formation occurs between the terminal oxygen atom (O'') of O₂ and a single carbon atom of C₆H₆. For the geometrical parameters of TS1 refer to Table 7.3. The C1–O'' bond distance is 1.584 \AA (1.620 \AA) in the triplet (broken-symmetry singlet), and 1.70 \AA in the singlet state, resulting in a decrease in Cu–O' bond distance by $\sim 0.1 \text{ \AA}$, and increase in the O'–O'' bond distance by $\sim 0.1 \text{ \AA}$. The O'–O'' bond length is about 1.37 \AA , which is still shorter than an O–O single bond³. The $\angle \text{H–C–O''}$ angle is in the range of $\sim 88^\circ - 94^\circ$, thus indicating a tilted C–H bond from the plane of the benzene ring and the presence of a

³The O–O bond length in H₂O₂ which is a measure of a typical O–O single bond, is $R_{(O-O)} = 1.475 \text{ \AA}$ [159].

TABLE 7.3: Geometrical parameters for TS1, the σ -complex, and TS2; H and C1 atoms are the nearest ones to the terminal oxygen (O'') of O₂.

	R _{Cu-O'}	R _{O'-O''}	C1-O''	C1-H	O''-H	∠ H-C-O''
TS1						
Triplet	1.813	1.377	1.584	1.105	1.995	94.1
Bs-singlet	1.812	1.369	1.620	1.102	2.011	93.3
Singlet	1.799	1.374	1.700	1.104	1.991	87.7
σ -complex						
Triplet	1.903	1.370	1.554	1.104	2.027	98.0
Bs-singlet	1.826	1.484	1.408	1.116	2.015	105.4
Singlet	1.823	1.462	1.428	1.123	2.081	108.7
TS2						
Triplet	1.731	1.957	1.399	1.210	1.442	66.7
Bs-singlet	1.731	1.902	1.403	1.240	1.388	63.0
Singlet	1.818	1.441	1.588	1.289	1.299	52.4

tetrahedral carbon. Therefore, the oxygen atom insertion into the C–H bond of benzene leads to a deformation of the benzene ring from a plane, and forms an activated C–H bond.

3. **σ -complex:** The σ -complex is likely to play an important role in the reaction pathway for the benzene to phenol conversion. The population analysis results of the precursor complex, TS1, and the σ -complex (cf. Tables 7.4, 7.5, 7.6) show a net charge flow from benzene \rightarrow dioxygen \rightarrow Cu center making the benzene ring more positive, and the O''/O' atoms more negative. The Cu 3*d* hole is increased from the precursor complex to TS1 and is further increased in the σ -complex indicating a π -back-donation from the Cu 3*d* orbital.
4. **TS2:** The second transition state is a three-centered transition state in which C–H bond breaking and O–H bond formation occur simultaneously to form the phenol-complex. It exhibits an imaginary frequency of 1150*i*, 1294*i* and 1390*i* cm⁻¹ in the triplet, broken-symmetry singlet and singlet states, respectively. The high frequency of this vibrational mode is a direct consequence of the C–H bond cleavage and the O–H bond formation, and the high energy barrier (cf. Fig. 7.4). In the triplet and the broken symmetry singlet states the O'–O'' bond lengths in TS2 are 1.957 Å and 1.902 Å (cf. Table 7.3), which are longer than a O–O single bond distance. In the singlet PES the O'–O'' bond length in TS2 is slightly shorter: 1.441 Å. The C–H and O''–H bond lengths are in the range of \sim 1.2

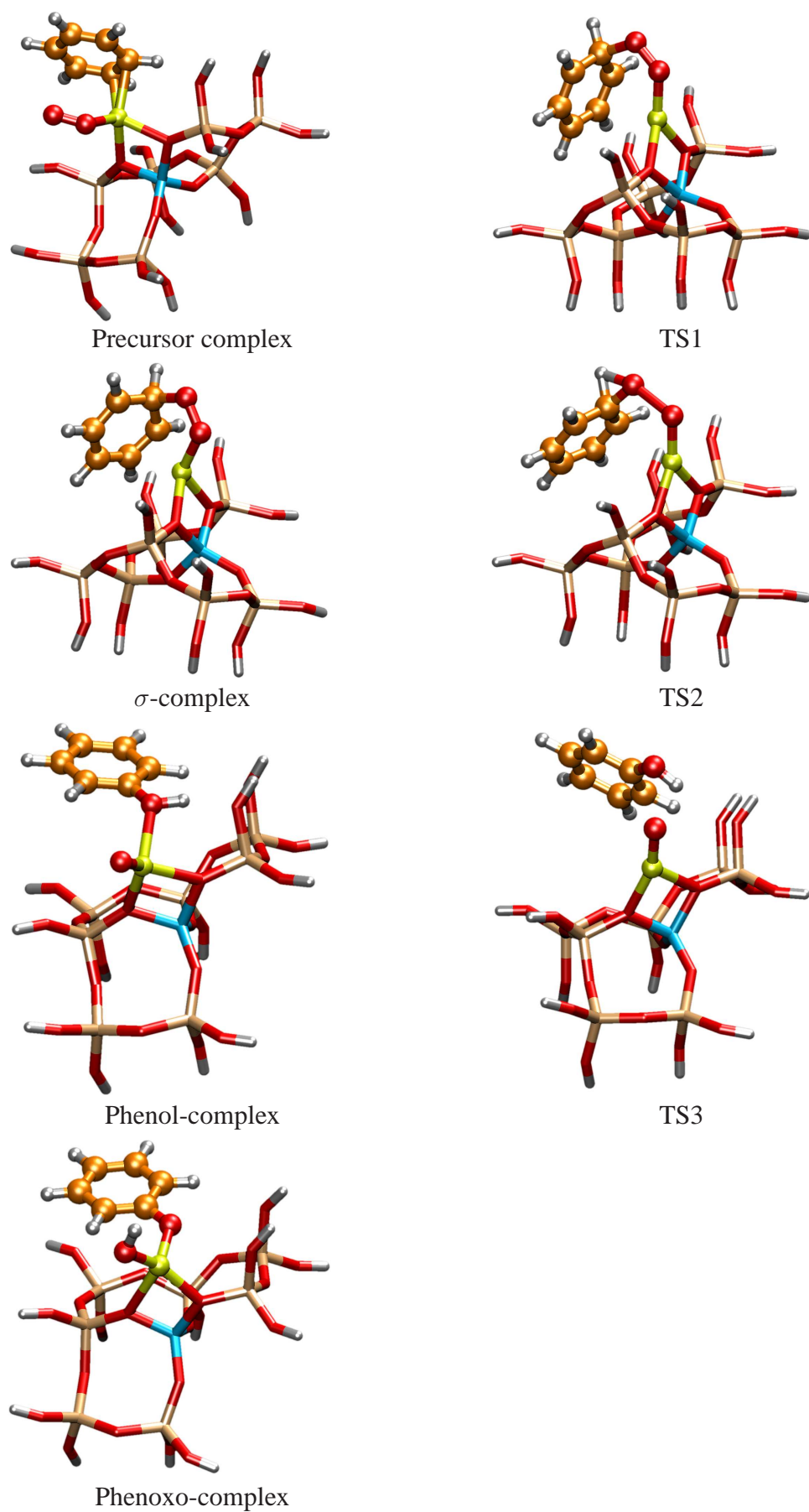


FIGURE 7.5: Reaction intermediates and transition states for the oxidation reaction of benzene to phenol using dioxygen in Cu–Y zeolite in the triplet state.

TABLE 7.4: Population analysis results for the precursor complex. C1, C2 carbon atoms are directly connected to Cu center and H1, H2 are hydrogen atoms of benzene ring forming C1–H1, C2–H2 bonds respectively.

	Atom/molecule	Charges	Occupation	Spin density
Triplet				
	Cu	1.10	3d ^{9.63} 4s ^{0.25}	0.28
	O'	-0.18	2s ^{1.82} 2p ^{4.35}	0.74
	O''	-0.04	2s ^{1.84} 2p ^{4.20}	0.88
	C1	-0.32		
	C2	-0.35		
	H1	0.28		
	H2	0.26		
	C ₆ H ₆	-0.01		
Broken Symmetry Singlet				
	Cu	1.12	3d ^{9.61} 4s ^{0.25}	-0.12
	O'	-0.20	2s ^{1.82} 2p ^{4.37}	0.10
	O''	-0.07	2s ^{1.84} 2p ^{4.22}	0.10
	C1	-0.32		
	C2	-0.35		
	H1	0.28		
	H2	0.26		
	C ₆ H ₆	0.01		
Singlet				
	Cu	1.10	3d ^{9.56} 4s ^{0.32}	
	O'	-0.32	2s ^{1.81} 2p ^{4.51}	
	O''	-0.16	2s ^{1.85} 2p ^{4.30}	
	C1	-0.36		
	H1	0.27		
	C ₆ H ₆	0.23		

– 1.3 Å, and $\sim 1.3 - 1.4$ Å. Nevertheless, these are quite reasonable for bond cleavage and bond formation situations.

- Phenol-complex:** The phenol-complexes have almost equal Cu–O' bond lengths (about 1.7 Å, see Table 7.7) on all three PESs. In the triplet and broken-symmetry singlet PESs, the O'–O'' bond is broken, although the singlet PES has an O'–O'' bond length of 1.846 Å.
- TS3:** The transition state TS3 is responsible for the migration of the phenolic H atom to the oxygen (O') of the Cu–O' moiety. In TS3, the O'–O'' bond length decreases to ~ 2.6 Å on the triplet and broken-symmetry singlet PESs (Table

TABLE 7.5: Population analysis results for TS1. The C1 carbon atom directly forms the C1–O bond and the H1 hydrogen atom is attached to the C1 carbon of the benzene ring.

	Atom/molecule	Charges	Occupation	Spin density
Triplet				
	Cu	1.10	3d ^{9.57} 4s ^{0.32}	0.42
	O'	-0.42	2s ^{1.83} 2p ^{4.58}	0.34
	O''	-0.13	2s ^{1.77} 2p ^{4.36}	0.33
	C1	-0.10		
	H1	0.23		
	C ₆ H ₆	0.29		
Broken Symmetry				
Singlet				
	Cu	1.10	3d ^{9.57} 4s ^{0.32}	0.36
	O'	-0.41	2s ^{1.83} 2p ^{4.58}	0.35
	O''	-0.14	2s ^{1.78} 2p ^{4.35}	0.10
	C1	-0.10		
	H1	0.23		
	C ₆ H ₆	0.29		
Singlet				
	Cu	0.89	3d ^{9.61} 4s ^{0.48}	
	O'	-0.43	2s ^{1.83} 2p ^{4.59}	
	O''	-0.17	2s ^{1.81} 2p ^{4.36}	
	C1	-0.14		
	H1	0.28		
	C ₆ H ₆	0.57		

7.7), which makes it easier to move the H atom from the phenolic oxygen to the Cu–O'–zeolite moiety. It has an imaginary frequency of $88i$, $145i$ and $355i$ cm⁻¹ in triplet, broken-symmetry singlet and singlet states, respectively. The vibrational mode of TS3 shows, a *rocking motion* of O–H bond which is responsible for this process and the low frequency.

7. **Phenoxo-complex:** The phenoxo-complex is the most stable intermediate in the proposed mechanistic pathway. In this phenoxo-intermediate the Cu–O' bond distance is around 1.8 Å on all three PESs.

TABLE 7.6: Population analysis results for σ -complex. The C1 carbon atom directly forms the C1–O bond and the H1 hydrogen atom is attached to the C1 carbon of the benzene ring.

	Atom/molecule	Charges	Occupation	Spin density
Triplet				
	Cu	1.15	3d ^{9.55} 4s ^{0.28}	0.43
	O'	-0.34	2s ^{1.85} 2p ^{4.49}	0.42
	O''	-0.11	2s ^{1.75} 2p ^{4.35}	0.35
	C1	-0.07		
	H1	0.23		
	C ₆ H ₆	0.14		
Broken Symmetry				
Singlet				
	Cu	1.18	3d ^{9.48} 4s ^{0.31}	
	O'	-0.50	2s ^{1.88} 2p ^{4.61}	
	O''	-0.23	2s ^{1.72} 2p ^{4.51}	
	C1	-0.04		
	H1	0.23		
	C ₆ H ₆	0.35		
Singlet				
	Cu	1.07	3d ^{9.53} 4s ^{0.39}	
	O'	-0.50	2s ^{1.87} 2p ^{4.63}	
	O''	-0.22	2s ^{1.72} 2p ^{4.49}	
	C1	-0.07		
	H1	0.26		
	C ₆ H ₆	0.49		

7.3.2 Energetics of the Reaction Pathway

The computed energy of the precursor complex in the triplet state is taken as the reference energy and in the following only the relative energies of all the intermediates and transition states in the different electronic states are discussed with respect to this reference energy.

Step 1: Fig. 7.4 shows the computed triplet, broken-symmetry singlet and singlet potential energy diagrams along the proposed pathway of benzene to phenol formation using dioxygen as the oxidant and Cu–Y zeolite as the catalyst.

The terminal oxygen (O'') of the precursor complex is directly forming a C–O bond via the transition state (TS1), and leads to the σ -complex. The singlet state of the precursor complex is 16.7 kcal mol⁻¹ above the triplet electronic state. The broken symmetry

TABLE 7.7: Geometrical parameters for the phenol-complex, TS3, and the phenoxo-complex; H and C1 atoms are the nearest ones to the terminal oxygen (O'') of O₂.

	R _{Cu-O'}	R _{O'-O''}	C1-O''	O''-H	∠ H-C-O''	Cu-O''
Phenol-complex						
Triplet	1.721	3.180	1.391	1.004	113.0	2.153
Bs-singlet	1.717	3.177	1.385	1.006	112.9	2.179
Singlet	1.732	1.846	1.378	1.043	112.9	non-bonded ^a
TS3						
Triplet	1.711	2.614	1.364	0.981	110.6	
Bs-singlet	1.709	2.599	1.358	0.985	111.4	
Singlet	1.712	2.095	1.356	0.997	113.6	
	R _{Cu-O'}	R _{O'-O''}	C1-O''	O'-H	Cu-O''	
Phenoxo-complex						
Triplet	1.791	3.114	1.296	0.975	1.905	
Bs-singlet	1.793	3.112	1.291	0.975	1.920	
Singlet	1.778	2.154	1.278	0.977	non-bonded ^a	

^a The phenoxide moiety is not coordinated to the Cu atom.

solution lies between singlet and triplet states. The trend of these three potential energy surfaces is conserved in the vicinity of TS1. The relative energies for TS1 in the triplet, broken-symmetry singlet, and singlet states are 31.2, 31.9, and 37.3 kcal mol⁻¹, respectively. For the individual spin states (triplet, broken-symmetry singlet, and singlet), the activation energies of TS1 are 31.2, 25.6, and 20.6 kcal mol⁻¹. It indicates that TS1 on the low-spin surface has a low energy barrier. The σ -complex in the triplet, singlet and broken-symmetry singlet states lie 29.2, 27.7, and 22.2 kcal mol⁻¹, respectively, above the precursor complex in the triplet state. This indicates a spin inversion between different electronic states in a crossing region of the potential energy surfaces (Fig. 7.4). *Indeed, the facile interconversion of various electronic states is quite probably the most crucial issue for the particular reactivity of transition-metal compounds* [155].

Step 2: The σ -complex rearranges to a phenol-complex by breaking the activated C-H bond and forming the O-H bond via TS2. The relative energies of TS2 lie at 50.4, 52.5 and 56.8 kcal mol⁻¹ in the singlet, triplet and the broken-symmetry singlet with respect to the precursor complex in the triplet state. The activation energy for TS2 is 22.7 kcal mol⁻¹ in the singlet state, whereas it is 23.3 kcal mol⁻¹ in the triplet state and the broken-symmetry singlet has the highest activation energy for TS2: 34.6 kcal mol⁻¹. The singlet (broken-symmetry singlet) potential energy surface is 32.5 (33.4) kcal mol⁻¹ exothermic, while the triplet one is 48.3 kcal mol⁻¹ exothermic in this step.

Step 3: The phenolic-H atom of the phenol-complex is migrated to the oxygen atom (O') of the O–Cu zeolite moiety via TS3 and a phenoxo-intermediate is formed. This process is a low-barrier one compared to the others. The activation energy for TS3 in the singlet state is 6.3 kcal mol⁻¹, and in the triplet state it is 4.7 kcal mol⁻¹, and 1.9 kcal mol⁻¹ in the broken-symmetry singlet surface. This process is 19.5 kcal mol⁻¹ exothermic in the singlet potential energy surface, and 26.7 (20.1) kcal mol⁻¹ for the broken-symmetry singlet (triplet) state.

The dissociation energy of the phenol-complex in the singlet state is 11.9 kcal mol⁻¹ with respect to the precursor complex in the triplet state, whereas for the triplet state the dissociation energy of the phenol-complex is 8.7 kcal mol⁻¹ below the reference energy. In any case, dissociation energies of the phenol-complexes are always higher than the activation energies of the formation of the phenoxo-complex. Therefore, the formation of the phenoxo-complex is preferred over the formation of phenol as the product. The phenoxo-complex is the most stable complex in the above mentioned reaction pathway.

The phenoxide moiety in the phenoxo-intermediate again gains the close proximity of the active Cu center keeping a Cu–O'' distance of about 1.9 Å on the triplet and the broken-symmetry singlet PESs. Therefore, one could think further of a transition state which would again form a different phenol-complex other than the presently found one. The favorable phenol-zeolite complex should have a different topology in the minimum of the PES that will prefer elimination of phenol rather than moving to the phenoxo-complex. In that case, elimination of phenol will result in a copper-oxo-zeolite complex, and possibly another benzene molecule will be needed to complete the catalytic cycle of benzene to phenol conversion.

7.3.3 Single-Point *ab initio* Calculations

The single-point QM calculations were performed employing only the QM region⁴ of the BP86(TZVP)/GULP optimized geometries of the reaction intermediates and the transition states of the closed-shell singlet PES. Given the size of the QM region (57 atoms) in Cu–Y zeolite, high-level correlated *ab initio* QM calculations are only possible with local correlation methods (see Section 2.1.10) in a reasonable computation time. All the *ab initio* wave function based single-point energies are calculated with

⁴In the QM/MM scheme of the QMPOT program, each (QM or MM) energy computation is independent of others. Therefore, the single-point energies of the QM fragment at different theoretical levels can be compared.

the MOLPRO quantum chemistry program [160]. The Table 7.8 shows the calculated relative energies of all the intermediates and the transition states at the following QM methods: BP86, Hartree-Fock (HF), local MP2 (LMP2), local coupled cluster variants (LCCSD, LCCSD(T0)), and B3LYP.

TABLE 7.8: The relative energies (w.r.t. precursor complex) in kcal mol⁻¹ of all the intermediates and the transition states at different levels of theory. Density fitting approximations are used throughout.

Structures	BP86 ^b	HF ^a	LMP2 ^a	LCCSD ^a	LCCSD(T0) ^a	B3LYP ^b
TS1	19.9	-0.6	45.0	19.4	29.0	18.8
σ -complex	9.5	-9.7	19.5	-1.8	1.4	7.4
TS2	32.8	10.1	45.5	24.8	33.0	30.2
Phenol-complex	-24.4	-51.1	2.5	-28.5	-23.2	-28.4
TS3	-18.2	-30.0	17.6	-11.8	-14.9	-18.8
Phenoxy-complex	-42.2	-53.4	-22.9	-34.3	-30.0	-45.7

^a AO basis: cc-pVTZ for Al, Si, framework O, link H, H_{benzene} except nearest to dioxygen; aug-cc-pVTZ for Cu, H_{benzene}(nearest to dioxygen), C, dioxygen

^b For basis sets, refer to Section 4.1.

The BP86/TZVP results in Table 7.8 should be taken as the reference, and those are supported by the high-level electron correlation methods. The LMP2 results show that the transition states and the reaction intermediates are substantially destabilized. Because, usually LMP2 overestimates the long-range correlation effects. The triple correction to the LCCSD result lowers the barrier height by ~ 3 kcal mol⁻¹ for TS3, however, increases the barrier height by ~ 10 kcal mol⁻¹ for TS1, and TS2. The reaction intermediates are destabilized at about 5 kcal mol⁻¹ by the triple correction to the LCCSD result. The B3LYP results are fairly close to the BP86 values. Mata and Werner [161] reported that calculations of the smooth PESs using the local approximations are challenging tasks. The accuracy of the local electron correlation methods strongly depend on the heart of the domain and the pair approximations on the model system to be investigated [162]. The situation can be more complicated, if the electronic structures of the reactants, products, and the transition states are quite different from each other. The domain sizes can be very different, and this can lead to unbalanced results. The local electron correlation results presented here are preliminary ones, therefore yet to be refined and determined in future.

Chapter 8

Summary

The aim of this investigation was to study the oxidation reaction of benzene using molecular oxygen as an oxidant and Cu-exchanged Y zeolite as a catalyst to form phenol as the product. Phenol is a versatile chemical which is used in the synthesis of petrochemicals, agrochemicals, and plastics. Most of the worldwide production of phenol is based on the cumene process which is a three-step process. The main advantage of the cumene process is the conversion of two relatively inexpensive starting materials, benzene and propylene into the chemicals such as phenol and acetone. However, the cumene process has certain disadvantages such as the production of an explosive intermediate (cumene hydroperoxide), the formation of acetone as a byproduct with 1:1 stoichiometry. Therefore, in spite of the great success of the cumene process, an environment-friendly alternative process is sought for. For producing phenol, a new route based on the aerobic oxidation of benzene in zeolites as catalysts is a well discussed area of current research. Mainly zeolites containing transition metals are used as heterogeneous catalysts, in particular Cu-containing Y zeolites are one of the prime concerns in that direction. The Cu centers are the most probable active sites in the Y zeolite. Certainly, all these facts support the motivation of the present work.

This thesis presents a theoretical study for understanding the adsorption processes in Cu-Y zeolite, which in turn give important information about the reaction between benzene and molecular oxygen in zeolites. Model calculations are performed using the QM/MM approach, a computationally efficient method which treats the active part of a system at the QM level and the remainder at the MM level. Within the QM/MM framework, the QM and MM calculations are performed using the BP86 and B3LYP density functionals, and a polarizable ion-pair shell-model potential, respectively. In the

QM calculations, triple zeta quality basis sets are employed. High-level benchmark *ab initio* (MRCI, CCSD(T)) calculations are performed for a simple CuO_2^+ model complex in order to evaluate the chosen BP86 functional. Satisfying agreement is found between the DFT results and the more accurate *ab initio* methods.

One of the major objectives of this thesis is to investigate the lone adsorption processes of dioxygen, benzene and the co-adsorption of both, dioxygen and benzene, in Cu–Y zeolites. Y zeolite has a large cavity (7.4 Å), called supercage, consisting of sodalite cages and hexagonal prisms. Among the 6 different well known cationic sites of a Y zeolite, sites II and III are chosen to host the cuprous ion. Sites II and III are situated on the plane of a 6-membered ring and at the edge of a 4-membered ring of a supercage, respectively. Adsorption processes are studied using different model zeolites containing one or two Al atoms and their different substitution patterns. In Cu–exchanged Y zeolite, the copper ion shows three-fold and two-fold coordinations with respect to the framework oxygens at sites II and III, respectively.

Adsorption of O_2 to Cu–Y zeolite shows mainly end-on coordination of O_2 to Cu at site II whereas site III shows side-on coordination of O_2 . Molecular oxygen is bound stronger to Cu at site III than at site II. Triplet states are the lowest-lying states as confirmed by high-level *ab initio* benchmark calculations for the model system. In all the adsorption complexes of site III, O_2 stretching vibrations are spread over a narrow range of $\sim 40 \text{ cm}^{-1}$, which supports the fact that site III adsorption complexes show solely side-on coordination of O_2 . In contrast to that, the O_2 stretching modes for site II adsorption complexes scatter over a range of more than 100 cm^{-1} , because site II adsorption complexes show both, end-on and side-on coordination of O_2 . The calculated harmonic frequency of dioxygen adsorbed at site III agrees quite nicely with the experimental IR result. Calculated O_2 stretching frequencies show a strong coupling with framework vibrations which make their assignment difficult.

Adsorption of benzene onto Cu in Y zeolite shows an η^2 -coordination of benzene to Cu in all adsorption complexes containing one or two Al atoms. The benzene–Cu–zeolite interaction is stronger for site III than for site II. The benzene–copper complexes show higher binding energies than the O_2 complexes. The ν_{13} C–C ring stretching mode of benzene is selected for the comparison between experimental IR results and calculated harmonic frequencies, and a reasonable agreement is found. The calculated splitting of the ν_{13} mode is not observed in the FTIR spectrum of adsorbed benzene to Cu–Y zeolites. In the adsorbed state, frequency shifts are found to be much smaller for benzene than dioxygen.

In the co-adsorption processes of O_2 and C_6H_6 , at site II, no complexes where both the adsorbates are connected simultaneously at the same Cu center are identified, instead some van der Waals complexes have been determined. Therefore, the main focus was at site III as far as the activation of both the adsorbates is concerned. Both O_2 and C_6H_6 are coordinated to the same Cu(I) center at site III. O_2 changes its bonding pattern from side-on in the single adsorption to end-on in the co-adsorption process, whereas C_6H_6 binds to Cu as η^2 as in the case of single adsorption.

A three-step reaction mechanism is found for benzene to phenol conversion using dioxygen as oxidant and Cu–Y zeolite as catalyst. The catalytic reaction has been investigated on the triplet, broken-symmetry singlet, and singlet potential energy surfaces. Oxygen is inserted to the benzene ring, and a C–O bond is formed. A phenol-zeolite complex is formed by breaking the activated C–H bond of benzene and by forming the phenolic O–H bond. Instead of phenol elimination, a phenoxo-zeolite complex is found to be the most stable complex in the whole catalytic cycle.

Overall, this thesis presents a contribution to understand the fundamental aspects of adsorbate-Cu-zeolite interactions, and a possible reaction pathway for catalytic conversion of benzene to phenol.

Chapter 9

Zusammenfassung

Das Ziel dieser Studie war die Untersuchung der katalytischen Oxidationsreaktion von Benzol zu Phenol mit molekularem Sauerstoff in Kupfer-dotierten Zeolithen. Phenol findet als Ausgangsstoff in der Polymerchemie, der petrochemischen Industrie und der Synthese von Herbiziden vielseitige Anwendungsbereiche. Der Großteil der weltweiten Produktion von Phenol basiert auf dem dreistufigen Cumol-Prozess. Ein erheblicher Vorteil dieses Prozesses liegt in der Verwendung der beiden verhältnismäßig günstigen Ausgangsstoffe Benzol und Propen, welche in Phenol und Aceton umgewandelt werden. Die Entstehung des explosiven Intermediates, Cumolhydroperoxid und die Bildung des Nebenproduktes Aceton machen diesen Prozess nicht optimal. Deshalb wird trotz des großen Erfolges des Cumol-Prozesses an der Entwicklung einer umweltfreundlicheren Darstellungsmethode gearbeitet. In der aktuellen Forschung wird ein neues Verfahren zur Phenolgewinnung, basierend auf der Oxidation von Benzol in Anwesenheit von Luftsauerstoff mittels eines Zeolithkatalysators diskutiert. Hier werden zumeist Übergangsmetallzeolithe, insbesondere Kupfer-dotierte Y-Zeolithe als heterogene Katalysatoren eingesetzt. Die Kupferzentren sind die aktiven Plätze des Y-Zeoliths.

Diese Arbeit legt eine theoretische Studie zum Verständnis des Adsorptionsvorgangs in CuY-Zeolithen dar, welche wichtige Informationen über die Reaktion zwischen Benzol und molekularem Sauerstoff in Zeolithen gibt. Die Modellrechnungen wurden mit einer rechenstechnisch effizienten Methode, dem QM/MM-Ansatz durchgeführt, wobei der reaktive Bereich des Systems auf QM und die Umgebung auf MM Niveau berechnet wurde. Die QM und MM Rechnungen wurden mit den Dichtefunktionalen BP86 und B3LYP sowie einem polarisierbaren Ionen-Paarpotential (shell-model) durchgeführt.

Für die QM Rechnungen wurden *triple zeta quality* Basissätze verwendet. Aufgrund der befriedigenden Übereinstimmung der sehr genauen *Benchmark ab initio* Rechnungen (MRCI, CCSD(T)) an einem einfachen CuO_2^+ Modellkomplex mit den DFT Ergebnissen wurde das BP86 Funktional ausgewählt.

Ein Schwerpunkt dieser Arbeit stellt die Untersuchung der alleinigen Adsorption von O_2 oder Benzol bzw. die gleichzeitige Adsorption von O_2 und Benzol an Cu–Y-Zeolithe dar. Y-Zeolithe besitzen mit 7.4 Å einen verhältnismäßig großen Porendurchmesser. Dieser sogenannte Zeolith-Supercage besteht aus Natrium Käfigen und hexagonalen Prismen. Das Cu Ion kann an sechs verschiedenen kationischen Adsorptionsplätzen des Y-Zeolithen koordinieren, es sind aber nur die Adsorptionsplätze SII und SIII von wesentlichem Interesse. Die Koordination des Kupfer Ions erfolgt bei dem Adsorptionsplatz SII über die Fläche eines 6-Ringes und bei SIII über die Ecken eines 4-Ringes eines Zeolith-Supercages. Zur Studie des Adsorptionsprozesses wurden Zeolithe mit ein und zwei Aluminiumatomen sowie deren Isomere untersucht. In Kupferdotierten Y-Zeolithen lagert das Kupfer Ion mit der Koordinationszahl $\text{KN}=2$ am Adsorptionsplatz SIII und mit $\text{KN}=3$ an SII an den Sauerstoffatomen des Zeolithgerüsts an.

Die Adsorption von O_2 an den Cu–Y-Zeolith erfolgt zumeist in einer end-on Koordination von O_2 an Cu an SII und einer side-on Koordination an SIII, wobei molekularer Sauerstoff am Adsorptionsplatz SIII im Vergleich zu SII eine stärkere Bindung zu Kupfer aufweist. Anhand von zuverlässigen *ab initio Benchmark* Rechnungen für das Modellsystem konnte bestätigt werden, dass Triplettzustände die am tiefst liegenden Zustände sind. Bei allen SIII Adsorptionskomplexen liegt die O_2 Streckschwingung innerhalb eines engen Bereiches von $\sim 40 \text{ cm}^{-1}$; diese Komplexe koordinieren nur side-on an O_2 . Im Gegensatz hierzu sind die O_2 Streckschwingungen der Adsorption an SII über einen weiten Bereich von 100 cm^{-1} verteilt. Demzufolge liegen bei Adsorptionskomplexen am Adsorptionsplatz SII sowohl side-on als auch end-on Koordinationen des O_2 vor. Es liegt eine gute Übereinstimmung der berechneten harmonischen Frequenz der O_2 Adsorption an SIII mit der IR spektroskopisch ermittelten Bande vor. Wegen der starken Kopplung der berechneten O_2 Streckschwingungen mit dem Zeolithgerüst ist eine Zuordnung der Schwingungsmoden vergleichsweise schwierig.

Sowohl CuY-Zeolithe mit ein als auch mit zwei Aluminiumatomen adsorbieren das Benzol über eine η^2 -Koordination an das Kupfer. Die Benzol-Kupfer-Zeolith Wechselwirkung ist am Adsorptionsplatz SIII stärker ausgeprägt. Die Bindungsenergie liegt bei Benzol-Kupfer Komplexen höher als bei den entsprechenden Sauerstoff Komplexen.

Für den Vergleich der experimentellen IR Ergebnisse mit den berechneten harmonischen Frequenzen wurde die ν_{13} C–C Ringstrettschwingung von Benzol herangezogen, hierbei konnte eine vernünftige Übereinstimmung festgestellt werden. Die bei der Berechnung auftretende Aufspaltung der ν_{13} Mode konnte im FTIR Spektrum von adsorbierten Benzol an CuY-Zeolithe nicht beobachtet werden.

Im adsorbierten Zustand liegen die Frequenzen des Benzols im Vergleich zum Sauerstoff bei niedrigeren Wellenzahlen. Die gleichzeitige Adsorption des Sauerstoffs und Benzols an SII führte nicht zu Coadsorptionskomplexen, stattdessen konnte ein van der Waals Komplex, bei dem beide Adsorbate am gleichen Kupferzentrum koordiniert sind, identifiziert werden. Aus diesem Grund wurde bezüglich der Aktivierung beider Adsorbate das Hauptaugenmerk auf den Adsorptionsplatz SIII gelegt, sowohl O_2 als auch C_6H_6 koordinieren hier an demselben Kupferzentrum. Sauerstoff ändert seine Bindung von side-on bei einer Einfachadsorption zu end-on in einem Coadsorptions-Prozess, wohingegen C_6H_6 bei einer Einfachadsorption über η^2 an Kupfer bindet.

Es konnte ein dreistufiger Reaktionsmechanismus für die Umwandlung des Benzols zu Phenol mit Hilfe des Oxidationsmittels O_2 und des CuY-Zeolith Katalysators gefunden werden. Die katalytische Reaktion wurde anhand von Triplett, symmetriegebrochenen Singulett und Singulett Potentialhyperflächen durchgeführt. Ein Phenol-Zeolith Komplex entsteht bei dem Bruch der aktivierten C–H Bindung von Benzol und der anschließenden Bildung der OH-Bindung des Phenols. Anstatt einer Phenoleliminierung wird ein sehr stabiler Phenoxy-Zeolithkomplex gebildet.

Diese Arbeit leistet einen Beitrag zum Verständnis der grundlegenden Gesichtspunkte der Wechselwirkungen von adsorbierten Kupferzeolithen sowie eines möglichen Reaktionspfades für die katalytische Umwandlung von Benzol zu Phenol.

Appendix A

Basis Set Studies on Various Model Complexes of Y Zeolites

TABLE A.1: Basis set dependence of some selected geometrical parameters of various bare Cu–Y model complexes (6T QM cluster) containing 2 Al atoms at site II. Bond lengths are given in Å. For the numbering of the atoms see Fig. 5.1.

Isomer A		
Parameters	SVP	TZVP
Cu-Al1	3.267	3.253
Cu-Al2	3.646	3.666
Cu-O4a	3.545	3.518
Cu-O2a	2.661	2.701
Cu-O2b	1.919	1.920
Cu-O2c	1.883	1.884

Isomer B		
Parameters	SVP	TZVP
Cu-Al1	2.856	2.851
Cu-Al2	3.193	3.195
Cu-O4a	2.790	2.805
Cu-O2a	1.898	1.899
Cu-O2b	2.460	2.479
Cu-O2c	1.895	1.895

Isomer C		
Parameters	SVP	TZVP
Cu-Al1	3.056	3.063
Cu-Al2	3.120	3.125
Cu-O4a	2.879	2.916
Cu-O2a	2.087	2.096
Cu-O2b	2.006	2.008
Cu-O2c	1.985	1.987

Isomer D		
Parameters	SVP	TZVP
Cu-Al1	2.711	2.723
Cu-Al2	3.676	3.669
Cu-O4a	2.573	2.575
Cu-O2a	1.909	1.912
Cu-O2b	2.762	2.759
Cu-O2c	1.879	1.880

Isomer E		
Parameters	SVP	TZVP
Cu-Al1	2.711	2.725
Cu-Al2	3.751	3.733
Cu-O4a	2.560	2.556
Cu-O2a	1.920	1.920
Cu-O2b	2.763	2.762
Cu-O2c	1.859	1.861

Isomer F		
Parameters	SVP	TZVP
Cu-Al1	3.061	3.066
Cu-Al2	3.169	3.157
Cu-O4a	2.874	2.911
Cu-O2a	2.069	2.079
Cu-O2b	2.011	2.012
Cu-O2c	1.991	1.993

Appendix B

QM-Pot Machinery

B.1 Convergence Criteria Used Throughout QM/MM Calculations

energy change	1.0e-5 eV
maximum gradient	1.0e-2 eV/Å
maximum step	1.0e-3 Å
rms gradient	1.0e-2 eV/Å
rms step	1.0e-2 Å

B.2 QM-Pot Optimizer

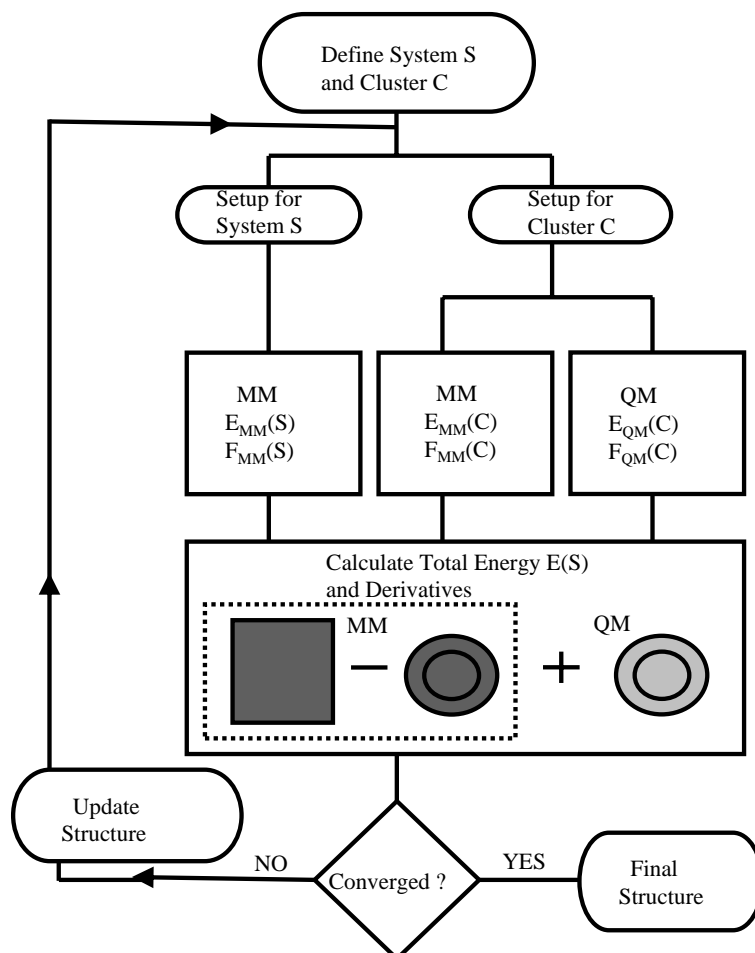


FIGURE B.1: A flow chart of the implementation of the embedding scheme used in the QM-Pot program, adapted from Ref. [40].

B.3 MM Parameters

TABLE B.1: Parameters of the DFT B3LYP derived shell-model potential^d.

groups ^a	charges / e	
	core	shell
Si	4.0 ^c	-
Al	3.0 ^c	-
O	1.228 58	-3.228 58
O _b	0.817 53	-2.817 53
H _b	1.0 ^c	-
H _t	1.0 ^c	-
short-range repulsion		
	<i>A</i> / eV	ρ / Å
Si-O	1612.459 20	0.299 55
Si-O _b	997.880 97	0.332 12
Al-O	1395.774 63	0.304 49
Al-O _b	1644.881 77	0.291 39
O _b -H _b	368.648 03	0.225 11
O-H _b	7614.580 03	0.199 13
O-H _t	772.068 14	0.185 24
core-shell interaction		
	<i>k</i> / eV Å ⁻²	
O	122.478 53	
O _b	70.151 23	
three-body interaction		
	<i>k_b</i> / eV rad ⁻²	Θ_0 / rad
O-Si-O	0.144 703	109.47 ^c
O _b -Si-O	0.384 711	109.47 ^c
O-Al-O	0.893 930	109.47 ^c
O _b -Al-O	0.686 678	109.47 ^c

^a Subscript definitions: *b* \equiv bridging, *t* \equiv terminal

^c Not adjusted in the fitting procedure.

^d Taken from Ref. [43]

Lennard-Jones 6-12 potential parameters:

	ϵ/k_B	σ
	(°K)	(Å)
O ₂ ^e	117.5	3.58
C ₆ H ₆ ^e	440.0	5.27

^e Taken from Ref. [101, pages 1111 & 1112]

Appendix C

Population Analyses

TABLE C.1: Population analysis results for Cu in bare–Cu and O₂ adsorption complexes containing 2 Al atoms at site II.

Isomers	Bare 2 Al-Complex		O ₂ 2 Al-Complex		
	Charges	Occupation	Charges	Occupation	Spin
A	0.83	3d ^{9.84} 4s ^{0.32}	1.16	3d ^{9.58} 4s ^{0.25}	0.43
N1	0.85	3d ^{9.88} 4s ^{0.26}	1.14	3d ^{9.61} 4s ^{0.24}	0.38
B	0.83	3d ^{9.83} 4s ^{0.33}	1.16	3d ^{9.57} 4s ^{0.26}	0.42
C	0.86	3d ^{9.89} 4s ^{0.23}	1.15	3d ^{9.57} 4s ^{0.27}	0.40
N2	0.86	3d ^{9.89} 4s ^{0.24}	1.12	3d ^{9.63} 4s ^{0.24}	0.36
D	0.84	3d ^{9.75} 4s ^{0.40}	1.14	3d ^{9.54} 4s ^{0.29}	0.48
E	0.87	3d ^{9.92} 4s ^{0.19}	1.08	3d ^{9.59} 4s ^{0.31}	0.33
E'			1.15	3d ^{9.53} 4s ^{0.30}	0.50
N3	0.86	3d ^{9.89} 4s ^{0.24}	1.18	3d ^{9.52} 4s ^{0.28}	0.52
F	0.86	3d ^{9.90} 4s ^{0.23}	1.12	3d ^{9.65} 4s ^{0.22}	0.36

TABLE C.2: Population analysis results for O₂ adsorption complexes containing 2 Al atoms at site II.

Isomers	O'			O''		
	Charges	Occupation	Spin	Charges	Occupation	Spin
A	-0.20	2s ^{1.82} 2p ^{4.37}	0.69	-0.13	2s ^{1.84} 2p ^{4.29}	0.76
N1	-0.22	2s ^{1.82} 2p ^{4.40}	0.67	-0.09	2s ^{1.84} 2p ^{4.25}	0.83
B	-0.30	2s ^{1.82} 2p ^{4.47}	0.58	-0.08	2s ^{1.85} 2p ^{4.22}	0.85
C	-0.30	2s ^{1.82} 2p ^{4.47}	0.58	-0.07	2s ^{1.85} 2p ^{4.21}	0.86
N2	-0.25	2s ^{1.82} 2p ^{4.42}	0.65	-0.05	2s ^{1.84} 2p ^{4.20}	0.87
D	-0.20	2s ^{1.85} 2p ^{4.34}	0.69	-0.15	2s ^{1.85} 2p ^{4.29}	0.77
E	-0.25	2s ^{1.80} 2p ^{4.44}	0.61	-0.03	2s ^{1.85} 2p ^{4.18}	0.89
E'	-0.18	2s ^{1.85} 2p ^{4.32}	0.72	-0.19	2s ^{1.85} 2p ^{4.33}	0.71
N3	-0.20	2s ^{1.85} 2p ^{4.34}	0.71	-0.20	2s ^{1.85} 2p ^{4.34}	0.69
F	-0.24	2s ^{1.82} 2p ^{4.41}	0.67	-0.05	2s ^{1.84} 2p ^{4.20}	0.88

TABLE C.3: Population analysis results for Cu in bare-Cu and O₂ adsorption complexes containing 2 Al atoms at site III.

Isomers	Bare 2 Al-Complex		O ₂ 2 Al-Complex		
	Charges	Occupation	Charges	Occupation	Spin
A	0.89	3d ^{9.92} 4s ^{0.17}	1.18	3d ^{9.51} 4s ^{0.28}	0.52
B	0.89	3d ^{9.92} 4s ^{0.17}	1.20	3d ^{9.51} 4s ^{0.28}	0.53
C	0.89	3d ^{9.92} 4s ^{0.17}	1.20	3d ^{9.51} 4s ^{0.27}	0.54
D	0.90	3d ^{9.92} 4s ^{0.17}	1.19	3d ^{9.52} 4s ^{0.27}	0.52
E	0.89	3d ^{9.92} 4s ^{0.18}	1.20	3d ^{9.50} 4s ^{0.28}	0.54
F	0.89	3d ^{9.92} 4s ^{0.17}	1.19	3d ^{9.51} 4s ^{0.28}	0.52
G	0.89	3d ^{9.92} 4s ^{0.17}	1.19	3d ^{9.51} 4s ^{0.28}	0.53
H	0.88	3d ^{9.92} 4s ^{0.18}	1.19	3d ^{9.51} 4s ^{0.28}	0.53
I	0.90	3d ^{9.93} 4s ^{0.16}	1.19	3d ^{9.52} 4s ^{0.27}	0.52

TABLE C.4: Population analysis results for O₂ adsorption complexes containing 2 Al atoms at site III.

Isomers	O'			O''		
	Charges	Occupation	Spin	Charges	Occupation	Spin
A	-0.17	2s ^{1.86} 2p ^{4.31}	0.74	-0.24	2s ^{1.85} 2p ^{4.38}	0.66
B	-0.21	2s ^{1.86} 2p ^{4.35}	0.70	-0.19	2s ^{1.86} 2p ^{4.33}	0.71
C	-0.19	2s ^{1.86} 2p ^{4.33}	0.72	-0.21	2s ^{1.85} 2p ^{4.35}	0.69
D	-0.19	2s ^{1.86} 2p ^{4.33}	0.72	-0.19	2s ^{1.86} 2p ^{4.33}	0.70
E	-0.20	2s ^{1.86} 2p ^{4.34}	0.71	-0.20	2s ^{1.86} 2p ^{4.34}	0.69
F	-0.18	2s ^{1.86} 2p ^{4.32}	0.73	-0.21	2s ^{1.85} 2p ^{4.35}	0.68
G	-0.21	2s ^{1.86} 2p ^{4.35}	0.69	-0.18	2s ^{1.86} 2p ^{4.32}	0.72
H	-0.19	2s ^{1.86} 2p ^{4.32}	0.73	-0.21	2s ^{1.85} 2p ^{4.35}	0.68
I	-0.21	2s ^{1.85} 2p ^{4.35}	0.70	-0.17	2s ^{1.86} 2p ^{4.31}	0.73

TABLE C.5: Population analysis results for benzene adsorption complexes containing 2 Al atoms at site II and III.

Isomers	site II			Isomers	site III		
	Charges		Occupation of Cu		Charges		Occupation of Cu
	Cu	C ₆ H ₆			Cu	C ₆ H ₆	
A	0.85	0.01	3d ^{9.77} 4s ^{0.36}	A	0.88	-0.01	3d ^{9.76} 4s ^{0.35}
B	0.98	-0.15	3d ^{9.74} 4s ^{0.27}	B	0.97	-0.11	3d ^{9.74} 4s ^{0.28}
C	0.97	-0.13	3d ^{9.73} 4s ^{0.29}	C	0.95	-0.09	3d ^{9.75} 4s ^{0.29}
D	0.87	0.00	3d ^{9.75} 4s ^{0.37}	D	0.96	0.20	3d ^{9.74} 4s ^{0.29}
E	0.94	-0.10	3d ^{9.74} 4s ^{0.31}	E	0.98	-0.13	3d ^{9.72} 4s ^{0.29}
F	0.95	-0.10	3d ^{9.75} 4s ^{0.29}	F	0.94	-0.07	3d ^{9.75} 4s ^{0.30}
				G	0.97	-0.12	3d ^{9.73} 4s ^{0.29}
				H	0.96	-0.11	3d ^{9.73} 4s ^{0.30}
				I	0.95	-0.09	3d ^{9.75} 4s ^{0.28}

TABLE C.6: Population analysis results for *endo*-“*simultaneous*” adsorption complexes containing 2 Al atoms at site III.

Isomers	Atom/molecule	Charges	Occupation	Spin density
A	Cu	1.06	$3d^{9.64}4s^{0.29}$	0.26
	O'	-0.17	$2s^{1.82}2p^{4.34}$	0.73
	O''	-0.04	$2s^{1.84}2p^{4.20}$	0.89
	C ₆ H ₆	0.03		
B	Cu	1.11	$3d^{9.62}4s^{0.25}$	0.30
	O'	-0.16	$2s^{1.82}2p^{4.33}$	0.75
	O''	-0.08	$2s^{1.84}2p^{4.23}$	0.85
	C ₆ H ₆	-0.01		
C	Cu	1.12	$3d^{9.61}4s^{0.26}$	0.32
	O'	-0.18	$2s^{1.82}2p^{4.35}$	0.73
	O''	-0.08	$2s^{1.84}2p^{4.24}$	0.84
	C ₆ H ₆	0.01		
D	Cu	1.09	$3d^{9.63}4s^{0.26}$	0.26
	O'	-0.14	$2s^{1.83}2p^{4.31}$	0.78
	O''	-0.07	$2s^{1.84}2p^{4.22}$	0.87
	C ₆ H ₆	-0.02		
E	Cu	1.12	$3d^{9.61}4s^{0.25}$	0.31
	O'	-0.18	$2s^{1.82}2p^{4.35}$	0.73
	O''	-0.09	$2s^{1.84}2p^{4.24}$	0.84
	C ₆ H ₆	-0.01		
F	Cu	1.10	$3d^{9.62}4s^{0.26}$	0.31
	O'	-0.18	$2s^{1.82}2p^{4.35}$	0.73
	O''	-0.08	$2s^{1.84}2p^{4.23}$	0.85
	C ₆ H ₆	0.02		
G	Cu	1.10	$3d^{9.62}4s^{0.26}$	0.28
	O'	-0.15	$2s^{1.83}2p^{4.32}$	0.75
	O''	-0.07	$2s^{1.84}2p^{4.23}$	0.87
	C ₆ H ₆	-0.02		
H	Cu	1.11	$3d^{9.61}4s^{0.26}$	0.30
	O'	-0.17	$2s^{1.83}2p^{4.34}$	0.74
	O''	-0.08	$2s^{1.84}2p^{4.24}$	0.85
	C ₆ H ₆	-0.01		
I	Cu	1.09	$3d^{9.63}4s^{0.26}$	0.29
	O'	-0.17	$2s^{1.82}2p^{4.34}$	0.74
	O''	-0.07	$2s^{1.84}2p^{4.23}$	0.86
	C ₆ H ₆	0.01		

TABLE C.7: Population analysis results for *exo*-“*simultaneous*” adsorption complexes containing 2 Al atoms at site III.

Isomers	Atom/molecule	Charges	Occupation	Spin density
A	Cu	1.06	$3d^{9.64}4s^{0.28}$	0.26
	O'	-0.18	$2s^{1.82}2p^{4.35}$	0.73
	O''	-0.04	$2s^{1.84}2p^{4.19}$	0.89
	C ₆ H ₆	0.02		
B	Cu	1.10	$3d^{9.63}4s^{0.25}$	0.29
	O'	-0.18	$2s^{1.82}2p^{4.36}$	0.74
	O''	-0.05	$2s^{1.84}2p^{4.21}$	0.87
	C ₆ H ₆	-0.01		
C	Cu	1.10	$3d^{9.62}4s^{0.26}$	0.29
	O'	-0.18	$2s^{1.82}2p^{4.36}$	0.73
	O''	-0.05	$2s^{1.84}2p^{4.21}$	0.87
	C ₆ H ₆	-0.01		
D	Cu	1.10	$3d^{9.63}4s^{0.26}$	0.28
	O'	-0.18	$2s^{1.82}2p^{4.36}$	0.73
	O''	-0.05	$2s^{1.84}2p^{4.20}$	0.88
	C ₆ H ₆	0.00		
E	Cu	1.11	$3d^{9.62}4s^{0.25}$	0.29
	O'	-0.18	$2s^{1.82}2p^{4.36}$	0.73
	O''	-0.06	$2s^{1.84}2p^{4.21}$	0.87
	C ₆ H ₆	-0.02		
F	Cu	1.09	$3d^{9.64}4s^{0.26}$	0.28
	O'	-0.18	$2s^{1.82}2p^{4.36}$	0.73
	O''	-0.04	$2s^{1.84}2p^{4.20}$	0.88
	C ₆ H ₆	0.01		
G	Cu	1.10	$3d^{9.63}4s^{0.25}$	0.28
	O'	-0.18	$2s^{1.82}2p^{4.35}$	0.73
	O''	-0.05	$2s^{1.84}2p^{4.21}$	0.88
	C ₆ H ₆	-0.01		
H	Cu	1.11	$3d^{9.62}4s^{0.26}$	0.31
	O'	-0.20	$2s^{1.82}2p^{4.38}$	0.71
	O''	-0.06	$2s^{1.84}2p^{4.21}$	0.86
	C ₆ H ₆	0.00		
I	Cu	1.09	$3d^{9.64}4s^{0.26}$	0.29
	O'	-0.18	$2s^{1.82}2p^{4.36}$	0.73
	O''	-0.05	$2s^{1.82}2p^{4.36}$	0.87
	C ₆ H ₆	0.01		

Appendix D

Cu(II)–Y Zeolite Modelling

Palomino et al. [74] reports that “*In fact, several reaction mechanisms have been hypothesized, but none of them satisfactorily takes into account the high activity of Cu–ZSM-5 and Cu–mordenite compared to Cu–Y, where the copper concentration is about 1 order of magnitude larger. This means that the knowledge of the exact location of Cu^I and/or Cu^{II} cations in different zeolitic frameworks and of their local environment in a vacuum and in the presence of adsorbates is likely a key point in understanding the reaction mechanism.*”

Several groups of researchers have been trying to characterize these materials not only by experimental works but also, by modelling their structures using theoretical tools. The present thesis mainly focuses on adsorption processes in Cu(I)–Y zeolite as well as the aerobic oxidation reaction of benzene to phenol in Cu(I)–Y zeolite.

The adsorption properties of Cu(II)–Y zeolite have also been studied in a similar fashion as it is done in case of Cu(I)–Y. In this appendix, some of the results from Cu(II)–Y zeolite are presented briefly.

The adsorption processes of O₂ and C₆H₆ in Cu(II)–Y zeolite have been studied at site II. The charge compensation is taken care of keeping 2 Al atoms in a unit cell with a Cu²⁺ cation. No additional H atom is added in the structures of Cu(II)–Y zeolite model systems. Therefore, a direct nomenclature from Cu(I) model complexes cannot be used for Cu(II) cases. Here, structures are defined in following manner:

1. when 2 Al atoms are in *meta* positions – Meta complexes (cf. Fig. D.1 Meta1, Meta2)

2. when 2 Al atoms are in *para* positions – Para complexes (cf. Fig. D.1 Para).

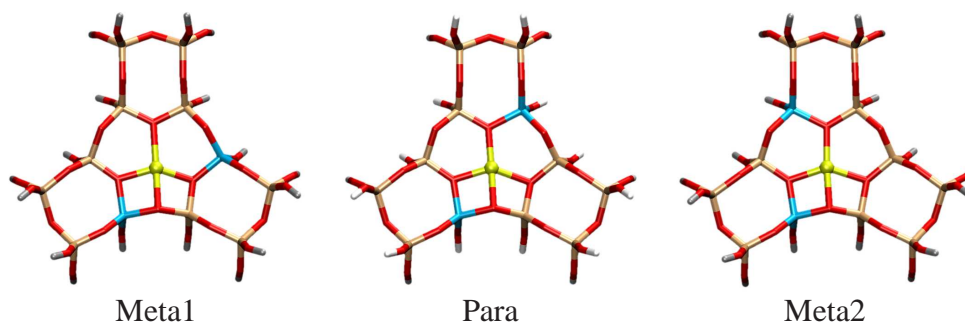


FIGURE D.1: Cu(II) at site II of CuY zeolite: QM part contains 12 Si/Al atoms – Meta1, Para, Meta2 complexes.

TABLE D.1: Site II of Cu(II)–Y zeolite: Cu–O bond distances to the next-nearest-neighbor framework O atoms, Cu–O' bond distances of O₂, Cu–C1(C2) bond lengths. C1, C2 carbons of C₆H₆ are directly attached to the Cu center.

	R_{Cu-O}	$R_{Cu-O'}$	$R_{O'-O''}$	Cu–C1	Cu–C1
<u>Bare-Cu-complex</u>					
Meta1	O2(1.948, 2.282, 1.943); O4(2.111)				
Para	O2(2.096, 2.039, 1.961); O4(2.074)				
Meta2	O2(2.076, 2.042, 1.962); O4(2.091)				
<u>O₂-Cu-complex</u>					
Meta1	O2(1.951, 2.299, 1.947); O4(2.119)	2.714	1.224		
Para	O2(2.115, 2.044, 1.968); O4(2.078)	2.655	1.225		
Meta2	O2(2.083, 2.045, 1.968); O4(2.093)	2.869	1.224		
<u>C₆H₆-Cu-complex</u>					
Meta1	O2(2.040, 2.163); O4(2.102)			2.293	2.163
Para	O2(2.395, 2.096, 2.035); O4(2.142)			2.476	2.355
Meta2	O2(2.336, 2.114, 2.046); O4(2.163)			2.450	2.368

Geometry optimizations, and harmonic frequency calculations have been performed using DFT-BP86 functional and TZVP basis sets within the QM/MM framework, similarly as it is done in case of Cu(I) complexes. The same MM parameters are used for these calculations except for the interaction parameters for Cu(II): $A_{Cu(II)O} = 712.8$ eV and $\rho_{Cu(II)O} = 0.32698 \text{ \AA}$ [163]. The doublet electronic state is chosen for all the calculations.

Table D.1 shows that Cu(II) to framework oxygen coordination is four-fold, which is larger than Cu(I). Cu(I) has 3-fold coordination with the zeolitic O atoms. Higher Cu(II) coordination was already reported by computational study of Berthomieu and Delahay [149], and experimental work of Palomino et al. [74].



FIGURE D.2: O_2 adsorbed to Cu(II) at site II of CuY zeolite: QM part contains 12 Si/Al atoms – Meta1, Para, Meta2 complexes.

TABLE D.2: Site II of Cu(II)–Y zeolite: relative stabilities (E_{rel}) of different complexes (with/without adsorbate) and binding energies (E_b) of O_2 and C_6H_6 .

	E_{rel}^a	O_2		C_6H_6	
		E_{rel}	E_b	E_{rel}	E_b
Meta1	4.4	2.5	-0.3	4.3	-5.6
Para	0.0	7.3	8.9	0.0	-5.5
Meta2	1.8	0.0	-0.2	2.0	-5.4

^a relative stabilities of bare-Cu-complexes

O_2 is almost unbound to Cu(II), and that is what is reflected in the negligible binding energy values of O_2 (see Table D.2 and Fig. D.2); whereas, C_6H_6 is η^2 -coordinated to Cu (see Table D.1 and Fig. D.3). Table D.2 shows the relative stabilities of different Cu(II)–Y zeolite model complexes before and after the adsorption process.

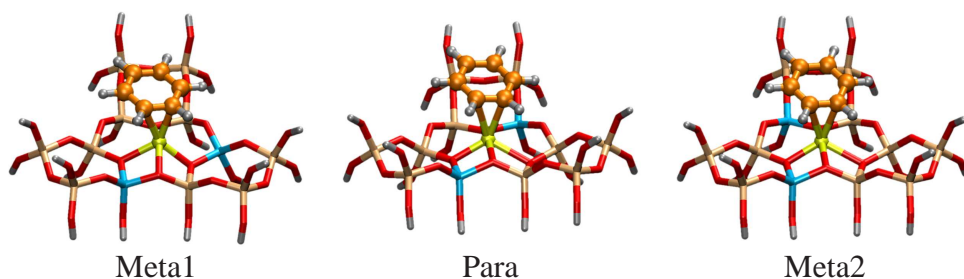


FIGURE D.3: C_6H_6 adsorbed to Cu(II) at site II of CuY zeolite: QM part contains 12 Si/Al atoms – Meta1, Para, Meta2 complexes.

Table D.3 shows calculated harmonic frequencies of O_2 stretching vibration and C–C ring stretching (ν_{13}) in adsorption complexes. O_2 behaves more or less like a free gas-phase entity. Therefore the frequency shift of the O_2 stretching mode in Cu(II)–Y zeolite is negligible as compared to the case of O_2 in Cu(I)–Y zeolite adsorption complexes. Benzene adsorption to Cu(II)–Y zeolite lowers the frequency shift value of the

TABLE D.3: Site II of Cu(II)–Y zeolite: calculated harmonic frequencies ν/cm^{-1} and frequency shifts $\Delta\nu/cm^{-1}$ of benzene and O₂ in gas-phase and adsorbed state. Scaling factors are 1.012 and 1.02 for C₆H₆ and O₂ respectively.

	C ₆ H ₆		O ₂	
	ν_{13} (C-C ring stretch)	$-\Delta\nu_{13}^a$	ν_{O-O} (O-O stretch)	$\Delta\nu_{O-O}^c$
Exp/Free	1484 ^b		1556	
Calc/Free	1489		1556	
Meta1	1469/1477	20/12	1546	10
Para	1476/1478	13/11	1581	-25
Meta2	1478/1478	11/11	1551	5

^a $\Delta\nu$ is the frequency shift of benzene from gas-phase to adsorbed state.

^b Taken from Ref. [137]

^c $\Delta\nu_{o-o}$ is the frequency shift of O₂ from gas-phase to adsorbed state.

C–C ring stretching in comparison with benzene adsorption to Cu(I)–Y, and the splitting of this mode is decreasing as well. In the Meta2 complex, no splitting is obtained.

Bibliography

- [1] T. Archipov, S. Santra, A. B. Ene, H. Stoll, G. Rauhut, and E. Roduner. Adsorption of benzene to copper in CuHY zeolite. *J. Phys. Chem. C*, 113:4107–4116, 2009.
- [2] S. Santra, T. Archipov, A. B. Ene, H. Komnik, H. Stoll, E. Roduner, and G. Rauhut. Adsorption of dioxygen to copper in CuHY zeolite. *Phys. Chem. Chem. Phys.*, 11:8855–8866, 2009.
- [3] F. Jensen. *Introduction to Computational Chemistry*. John Wiley & Sons, England, 2003.
- [4] C. S. John and H. F. Leach. Determination of the active site and mechanism for alkene isomerization in Cu^{II} exchanged Y-type zeolite. *J. Chem. Soc., Faraday Trans. 1*, 73:1595–1604, 1977.
- [5] H. Matsumoto and S. Tanabe. Catalytic behavior and structure of active species on Cu–Y zeolite in oxidation of carbon monoxide. *J. Phys. Chem.*, 94:4207–4212, 1990.
- [6] S. T. King. Reaction mechanism of oxidative carbonylation of methanol to dimethyl carbonate in Cu–Y zeolite. *J. Catal.*, 161:530–538, 1996.
- [7] Y. Zhang and A. T. Bell. The mechanism of dimethyl carbonate synthesis on Cu–exchanged zeolite Y. *J. Catal.*, 255:153–161, 2008.
- [8] X. Zheng and A. T. Bell. A theoretical investigation of dimethyl carbonate synthesis on Cu–Y zeolite. *J. Phys. Chem. C*, 112:5043–5047, 2008.
- [9] K. Tsutsumi, S. Fuji, and H. Takahashi. Cumene cracking activity of zeolite catalysts : III. Effect of copper(II) ion exchange on the faujasite-type synthetic zeolites. *J. Catal.*, 24:146–152, 1972.

- [10] M. Iwamoto, J. Hirata, K. Matsukami, and S. Kagawa. Catalytic oxidation by oxide radical ions. 1. One-step hydroxylation of benzene to phenol over group 5 and 6 oxides supported on silica gel. *J. Phys. Chem.*, 87:903–905, 1983.
- [11] A. Thangaraj, R. Kumar, and P. Ratnasamy. Catalytic properties of crystalline titanium silicalites II. Hydroxylation of phenol with hydrogen peroxide over TS-1 zeolites. *J. Catal.*, 131:294–297, 1991.
- [12] G.I. Panov. Advances in oxidation catalysis; oxidation of benzene to phenol by nitrous oxide. *CATTECH*, 4:18–31, 2000.
- [13] G. I. Panov, V. I. Sobolev, and A. S. Kharitonov. The role of iron in N_2O decomposition on ZSM-5 zeolite and reactivity of the surface oxygen formed. *J. Mol. Catal*, 61:85–97, 1990.
- [14] K. A. Dubkov, N. S. Ovanesyan, A. A. Shteinman, E. V. Starokon, and G. I. Pannov. Evolution of iron states and formation of α -sites upon activation of FeZSM-5 zeolites. *J. Catal*, 207:341–352, 2002.
- [15] E. J. M. Hensen, Q. Zhu, R. A. J. Janssen, P. C. M. M. Magusin, P. J. Kooyman, and R. A. van Santen. Selective oxidation of benzene to phenol with nitrous oxide over MFI zeolites: 1. On the role of iron and aluminum. *J. Catal*, 233:123–135, 2005.
- [16] K. Yoshizawa, Y. Shiota, T. Yumura, and T. Yamabe. Direct methane–methanol and benzene–phenol conversions on Fe–ZSM-5 zeolite: Theoretical predictions on the reaction pathways and energetics. *J. Phys. Chem. B*, 104:734–740, 2000.
- [17] Y. Shiota, K. Suzuki, and K. Yoshizawa. QM/MM study on the catalytic mechanism of benzene hydroxylation over Fe–ZSM-5. *Organometallics*, 25:3118–3123, 2006.
- [18] R. Hamada and Y. Shibata, S. Nishiyama, and S. Tsuruya. One-step gas-phase catalytic oxidation of benzene to phenol with molecular oxygen over Cu-supported ZSM-5 zeolites. *Phys. Chem. Chem. Phys.*, 5:956–965, 2003.
- [19] Y. Shibata, R. Hamada, T. Ueda, Y. Ichihashi, S. Nishiyama, and S. Tsuruya. Gas-phase catalytic oxidation of benzene to phenol over Cu-impregnated HZSM-5 catalysts. *Ind. Eng. Chem. Res.*, 44:8765–8772, 2005.

- [20] H. Yamanaka, R. Hamada, H. Nibuta, S. Nishiyama, and S. Tsuruya. Gas-phase catalytic oxidation of benzene over Cu-supported ZSM-5 catalysts: an attempt of one-step production of phenol. *J. Mol. Catal. A: Chemical*, 178:89–95, 2002.
- [21] T. Kitamura, H. Kanzaki, R. Hamada, S. Nishiyama, and S. Tsuruya. Liquid-phase oxidation of benzene to phenol by copper catalysts in aqueous solvent with a high acetic acid concentration. *Can. J. Chem.*, 82:1597–1605, 2004.
- [22] N. B. Castagnola, A. J. Kropf, and C. L. Marshall. Studies of Cu-ZSM-5 by X-ray absorption spectroscopy and its application for the oxidation of benzene to phenol by air. *Appl. Catal. A: General*, 290:110–122, 2005.
- [23] H. C. Longuet-Higgins. *Advances in Spectroscopy*. Interscience, New York, 1962.
- [24] R. G. Parr. *Quantum Theory of Molecular Electronic Structure*. Benjamin, New York, 1963.
- [25] A. Szabo and N. S. Ostlund. *Modern Quantum Chemistry*. Dover, New York, 1996.
- [26] S. Saebø and P. Pulay. Fourth-order Møller-Plesset perturbation theory in the local correlation treatment. I. Method. *J. Chem. Phys.*, 86:914–922, 1987.
- [27] J. Pipek and P. G. Mezey. A fast intrinsic localization procedure applicable for ab initio and semiempirical linear combination of atomic orbital wave functions. *J. Chem. Phys.*, 90:4916–4926, 1989.
- [28] P. A. M. Dirac. Quantum mechanics of many-electron systems. *Proc. R. Soc. Lond. A*, 123:714–733, 1929.
- [29] J. C. Slater. A simplification of the Hartree-Fock method. *Phys. Rev.*, 81:385–390, 1951.
- [30] A. D. Becke. Density-functional exchange-energy approximation with correct asymptotic behavior. *Phys. Rev. A*, 38:3098–3100, 1988.
- [31] S. Vosko, L. Wilk, and M. Nusair. Accurate spin-dependent electron liquid correlation energies for local spin density calculations: a critical analysis. *Can. J. Phys.*, 58:1200–1211, 1980.
- [32] J. P. Perdew. Density-functional approximation for the correlation energy of the inhomogeneous electron gas. *Phys. Rev. B*, 33:8822–8824, 1986.

- [33] A. R. Leach. *Molecular Modelling Principles and Applications*. Pearson Education Limited, England, 2001.
- [34] J. D. Gale. Empirical potential derivation for ionic materials. *Phil. Mag. B*, 73: 3–19, 1996.
- [35] J. D. Gale. GULP: A computer program for the symmetry-adapted simulation of solids. *J. Chem. Soc., Faraday Trans.*, 93:629–637, 1997.
- [36] B. G. Dick and A. W. Overhauser. Theory of the dielectric constants of alkali halide crystals. *Phys. Rev.*, 112:90–103, 1958.
- [37] R. A. Jackson and C. R. A. Catlow. Computer simulation studies of zeolite structure. *Mol. Simul.*, 1:207–224, 1997.
- [38] K-P. Schröder and J. Sauer. Potential functions for silica and zeolite catalysts based on ab initio calculations. 3. A shell model ion pair potential for silica and aluminosilicates. *J. Phys. Chem.*, 100:11043–11049, 1996.
- [39] A. Warshel and M. Levitt. Theoretical studies of enzymic reactions: Dielectric, electrostatic and steric stabilization of the carbonium ion in the reaction of lysozyme. *J. Mol. Biol.*, 103:227–249, 1976.
- [40] U. Eichler, C. M. Kölmel, and J. Sauer. Combining ab initio techniques with analytical potential functions for structure predictions of large systems: Method and application to crystalline silica polymorphs. *J. Comput. Chem.*, 18:463–477, 1996.
- [41] M. Brändle and J. Sauer. Combining ab initio techniques with analytical potential functions. A study of zeolite-adsorbate interactions for NH₃ on H-faujasite. *J. Mol. Catal. A: Chemical*, 119:19–33, 1997.
- [42] U. Eichler, M. Brändle, and J. Sauer. Predicting absolute and site specific acidities for zeolite catalysts by a combined quantum mechanics/interatomic potential function approach. *J. Phys. Chem. B*, 101:10035–10050, 1997.
- [43] M. Sierka and J. Sauer. Structure and reactivity of silica and zeolite catalysts by a combined quantum mechanics-shell-model potential approach based on DFT. *Faraday Discuss.*, 106:41–62, 1997.
- [44] M. E. Davis. Ordered porous materials for emerging applications. *Nature*, 417: 813–821, 2002.

- [45] E. M. Flanigen. Zeolites and molecular sieves an historical perspective. *Stud. Surf. Sci. Catal.*, 58:13–34, 1991.
- [46] L. A. Pine, P. J. Maher, and W. A. Wachter. Prediction of cracking catalyst behavior by a zeolite unit cell size model. *J. Catal.*, 85:466–476, 1984.
- [47] J. Scherzer. Correlation between catalyst formulation and catalytic properties. *Stud. Surf. Sci. Catal.*, 76:145–182, 1993.
- [48] T. Maesen. The zeolite scene - an overview. *Stud. Surf. Sci. Catal.*, 168:1–12, 2007.
- [49] L. Moscou. The zeolite scene. *Stud. Surf. Sci. Catal.*, 58:1–12, 1991.
- [50] T. Maesen and B. Marcus. The zeolite scene - an overview. *Stud. Surf. Sci. Catal.*, 137:1–9, 2001.
- [51] L.B. McCusker Ch. Baerlocher and D.H. Olson. *Atlas of Zeolite Framework Types*. Elsevier, London, 6th edition edition, 2007.
- [52] E. M. Flanigen and J. A. Rabo. A tribute to Robert Mitchell Milton, zeolite pioneer (1920-2000). *Micropor. Mesopor. Mater.*, 47:119–126, 2001.
- [53] C. S. Cundy and P. A. Cox. The hydrothermal synthesis of zeolites: history and development from the earliest days to the present time. *Chem. Rev.*, 103:663–702, 2003.
- [54] R. Szostak. Secondary synthesis methods. *Stud. Surf. Sci. Catal.*, 137:261–297, 2001.
- [55] A. Nicula, D. Stamires, and J. Turkevich. Paramagnetic resonance absorption of copper ions in porous crystals. *J. Chem. Phys.*, 42:3684–3691, 1965.
- [56] J. T. Richardson. Crystal field effects in ion-exchanged faujasites. *J. Catal.*, 9:178–181, 1967.
- [57] J. T. Richardson. ESR studies of cationic oxidation sites in faujasite. *J. Catal.*, 9:172–177, 1967.
- [58] H. B. Slot and J. L. Verbeek. The migration of metal ions in zeolite-Y as revealed by ESR of Cu^{2+} . *J. Catal.*, 12:216–220, 1968.

- [59] I. Mochida, S. Hayata, A. Kato, and T. Seiyama. Catalytic oxidation of propylene over Cu(II)-Y molecular sieve. *J. Catal.*, 15:314–316, 1969.
- [60] C. M. Naccache and Y. Ben Taarit. Oxidizing and acidic properties of copper-exchange Y zeolite. *J. Catal.*, 22:171–181, 1971.
- [61] C. Naccache, M. Che, and Y. Ben Taarit. ESR and IR studies on the adsorption and disproportionation of nitric oxide on copper exchanged Y zeolites, and of reduction by carbon monoxide. *Chem. Phys. Lett.*, 13:109–114, 1972.
- [62] W. B. Williamson and J. H. Lunsford. Nitric oxide reduction with ammonia over copper(II) Y zeolites. *J. Phys. Chem.*, 80:2664–2671, 1976.
- [63] M. Mizumoto, N. Yamazoe, and T. Seiyama. Catalytic reduction of NO with ammonia over Cu(II) NaY. *J. Catal.*, 55:119–128, 1978.
- [64] S. Kagawa, S. Yokoo, and M. Iwamoto. Activity of copper(II)-exchanged Y-type zeolites in the catalytic decomposition of nitrogen monoxide. *J. Chem. Soc., Chem. Commun.*, pages 1058–1059, 1978.
- [65] M. C. Campa, V. Indovina, G. Minelli, G. Moretti, I. Pettiti, P. Porta, and A. Riccio. The catalytic activity of Cu-ZSM-5 and Cu-Y zeolites in NO decomposition: dependence on copper concentration. *Catal. Lett.*, 23:141–149, 1993.
- [66] P. Ciambelli, P. Corbo, M. Gambino, V. Indovina, G. Moretti, and M.C. Campa. Lean NO_x reduction on Cu-NaY and Cu-HZSM5 zeolites at the spark ignition engine exhaust. *Stud. Surf. Sci. Catal.*, 96:605–617, 1995.
- [67] M. Iwamoto, S. Yokoo, K. Sakai, and S. Kagawa. Catalytic decomposition of nitric oxide over copper(II)-exchanged, Y-type zeolites. *J. Chem. Soc., Faraday Trans. 1*, 77:1629–1638, 1981.
- [68] R. Rudham and A. Stockwell. Catalysis on faujasite zeolites. *Catalysis*, 1:87–135, 1977.
- [69] P. Gallezot, Y. Ben Taarit, and B. Imelik. X-ray diffraction study of cupric ion migrations in two Y-type zeolites containing adsorbed reagents. *J. Catal.*, 26: 295–302, 1972.
- [70] I. E. Maxwell and J. J. De Boer. Crystal structures and dehydrated divalent-copper-exchanged faujasite. *J. Phys. Chem.*, 79:1874–1879, 1975.

- [71] J. V. Smith. Faujasite-type structures. Aluminosilicate framework. Positions of cations and molecules. Nomenclature. *Adv. Chem. Ser.*, 101:171–220, 1971.
- [72] S. Bordiga, D. Scarano, G. Spoto, and A. Zecchina. Infrared study of carbon monoxide adsorption at 77 K on faujasites and ZSM-5 zeolites. *Vib. Spectrosc.*, 5:69–74, 1993.
- [73] S. Bordiga, E. Garrone, C. Lamberti, A. Zecchina, C. O. Areán, V. B. Kazansky, and L. M. Kustov. Comparative IR-spectroscopic study of low-temperature H₂ and CO adsorption on Na zeolites. *J. Chem. Soc., Faraday Trans.*, 90:3367–3372, 1994.
- [74] G. T. Palomino, S. Bordiga, A. Zecchina, G. L. Marra, and C. Lamberti. XRD, XAS, and IR characterization of copper-exchanged Y zeolite. *J. Phys. Chem. B*, 104:8641–8651, 2000.
- [75] A. Delabie, K. Pierloot, M. H. Groothaert, R. A. Schoonheydt, and L. G. Vanquickenborne. The coordination of Cu(II) in zeolites - structure and spectroscopic properties. *Eur. J. Inorg. Chem.*, pages 515–530, 2002.
- [76] K. Dyrek. EPR as a tool to investigate the transition metal chemistry on oxide surfaces. *Chem. Rev.*, 97:305–332, 1997.
- [77] C. Lamberti, G. Spoto, D. Scarano, C. Pazé, M. Salvalaggio, S. Bordiga, A. Zecchina, G. T. Palomino, and F. D’Acapito. Cu^I-Y and Cu^{II}-Y zeolites: a XANES, EXAFS and visible-NIR study. *Chem. Phys. Lett.*, 269:500–508, 1997.
- [78] K. Pierloot, A. Delabie, M. H. Groothaert, and R. A. Schoonheydt. A reinterpretation of the EPR spectra of Cu(II) in zeolites A, Y and ZK4, based on *ab initio* cluster model calculations. *Phys. Chem. Chem. Phys.*, 3:2174–2183, 2001.
- [79] H. Yahiro, Y. Ohmori, and M. Shiotani. Magnetic interaction between copper (II) ion and paramagnetic NO and O₂ molecules in Y-type zeolite at low temperature: An EPR study. *Micropor. Mesopor. Mater.*, 83:165–171, 2005.
- [80] S. Ramdas, J. M. Thomas, J. Klinowski, C. A. Fyfe, and J. S. Hartman. Ordering of aluminium and silicon in synthetic faujasites. *Nature*, 292:228–230, 1981.
- [81] M. Hunger, M. W. Anderson, and H. Pfeifer. Study of the geometry and location of the bridging oh groups in aluminosilicate and silicoaluminophosphate type zeolites using ¹H MAS NMR sideband analysis and CP/MAS NMR. *Micropor. Mater.*, 1:17–32, 1992.

- [82] E. M. Flanigen, H. Khatami, and H. A. Szymanski. Infrared structural studies of zeolite framework. *Adv. Chem. Ser.*, 101:201–229, 1971.
- [83] A. J. M. de Man and R. A. van Santen. The relation between zeolite framework structure and vibrational spectra. *Zeolites*, 12:269–279, 1992.
- [84] J. A. Lercher and A. Jentys. Infrared and raman spectroscopy for characterizing zeolites. *Stud. Surf. Sci. Catal.*, 168:435–476, 2007.
- [85] J. Sárkány and W. M. H. Sachtler. Redox chemistry of Cu/ZSM-5: effect of oxygen. an FTIR study. *Stud. Surf. Sci. Catal.*, 94:649–656, 1995.
- [86] J. Sárkány. FTIR study on the interaction of O₂ and CO with Cu⁺ ions in zeolite ZSM-5 formation and reactivity of superoxide. *J. Mol. Struct.*, 410:95–98, 1997.
- [87] V. B. Kazansky, V. Y. Borovkov, and H. G. Karge. Diffuse reflectance IR study of molecular hydrogen and deuterium adsorbed at 77 K on NaA zeolite part 1.- Fundamentals, combination and vibrational-rotational modes. *J. Chem. Soc., Faraday Trans.*, 93:1843–1848, 1997.
- [88] G. Busca. The surface acidity of solid oxides and its characterization by IR spectroscopic methods. an attempt at systematization. *Phys. Chem. Chem. Phys.*, 1:723–736, 1999.
- [89] H. Knözinger and S. Huber. IR spectroscopy of small and weakly interacting molecular probes for acidic and basic zeolites. *J. Chem. Soc., Faraday Trans.*, 94:2047–2059, 1998.
- [90] K. Eichkorn, O. Treutler, H. Öhm, M. Häser, and R. Ahlrichs. Auxiliary basis sets to approximate coulomb potentials. *Chem. Phys. Lett.*, 242:652–660, 1995.
- [91] K. Eichkorn, F. Weigend, O. Treutler, and R. Ahlrichs. Auxiliary basis sets for main row atoms and transition metals and their use to approximate coulomb potentials. *Theor. Chem. Acc.*, 97:119–124, 1997.
- [92] C. Lee, W. Yang, and R. G. Parr. Development of the Colle-Salvetti correlation-energy formula into a functional of the electron density. *Phys. Rev. B*, 37:785–789, 1988.
- [93] A. D. Becke. Density-functional thermochemistry. III. The role of exact exchange. *J. Chem. Phys.*, 98:5648–5652, 1993.

- [94] A. Schäfer, C. Huber, and R. Ahlrichs. Fully optimized contracted Gaussian basis sets of triple zeta valence quality for atoms Li to Kr. *J. Chem. Phys.*, 100: 5829–5835, 1994.
- [95] D. Figgen, G. Rauhut, M. Dolg, and H. Stoll. Energy-consistent pseudopotentials for group 11 and 12 atoms: adjustment to multi-configuration Dirac-Hartree-Fock data. *Chem. Phys.*, 311:227–244, 2005.
- [96] K. A. Peterson and C. Puzzarini. Systematically convergent basis sets for transition metals. II. Pseudopotential-based correlation consistent basis sets for the group 11 (Cu, Ag, Au) and 12 (Zn, Cd, Hg) elements. *Theor. Chem. Acc.*, 114: 283–296, 2005.
- [97] TURBOMOLE Version 5.10 2008, a development of University of Karlsruhe and Forschungszentrum Karlsruhe GmbH, 1989-2007, since 2007 TURBOMOLE GmbH, 2008. <http://www.turbomole.com>.
- [98] O. Treutler and R. Ahlrichs. Efficient molecular numerical integration schemes. *J. Chem. Phys.*, 102:346–354, 1995.
- [99] M. Sierka and J. Sauer. Finding transition structures in extended systems: A strategy based on a combined quantum mechanics–empirical valence bond approach. *J. Chem. Phys.*, 112:6983–6996, 2000.
- [100] D. Nachtigallová, P. Nachtigall, M. Sierka, and J. Sauer. Coordination and siting of Cu^+ ions in ZSM-5: A combined quantum mechanics/interatomic potential function study. *Phys. Chem. Chem. Phys.*, 1:2019–2026, 1999.
- [101] J. O. Hirschfelder, C. F. Curtiss, and R. B. Bird. *Molecular Theory of Gases and Liquids*. John Wiley & Sons Inc., New York, 1954.
- [102] W. Loewenstein. The distribution of aluminum in the tetrahedra of the silicates and aluminates. *Am. Mineral*, 39:92–96, 1954.
- [103] P. Rejmak, M. Sierka, and J. Sauer. Theoretical studies of Cu(I) sites in faujasite and their interaction with carbon monoxide. *Phys. Chem. Chem. Phys.*, 9:5446–5456, 2007.
- [104] N. Jardillier, D. Berthomieu, A. Goursot, J. U. Reveles, and A. M. Köster. Theoretical study of Cu^IY zeolite: Structure and electronic properties. *J. Phys. Chem. B*, 110:18440–18446, 2006.

- [105] D. Nachtigallová, O. Bludský, C.O. Areán, R. Bulánek, and P. Nachtigall. The vibrational dynamics of carbon monoxide in a confined space-CO in zeolites. *Phys. Chem. Chem. Phys.*, 8:4849–4852, 2006.
- [106] J. Hrušák, W. Koch, and H. Schwarz. An ab initio molecular orbital study of the structures and energetics of the neutral and cationic CuO_2 and CuNO molecules in the gas phase. *J. Chem. Phys.*, 101:3898–3905, 1994.
- [107] J. M. Ducéré, A. Goursot, and D. Berthomieu. Comparative density functional theory study of the binding of ligands to Cu^+ and Cu^{2+} : Influence of the coordination and oxidation state. *J. Phys. Chem. A*, 109:400–408, 2005.
- [108] C. J. Cramer, J. R. Gour, A. Kinal, M. Wloch, P. Piecuch and A. R. M. Shahi, and L. Gagliardi. Stereoelectronic effects on molecular geometries and state-energy splittings of ligated monocopper dioxygen complexes. *J. Phys. Chem. A*, 112:3754–3767, 2008.
- [109] C. Hampel, K. A. Peterson, and H.-J. Werner. A comparison of the efficiency and accuracy of the quadratic configuration interaction (QCISD), coupled cluster (CCSD), and Brueckner coupled cluster (BCCD) methods. *Chem. Phys. Lett.*, 190:1–12, 1992.
- [110] M. J. O. Deegan and P. J. Knowles. Perturbative corrections to account for triple excitations in closed and open shell coupled cluster theories. *Chem. Phys. Lett.*, 227:321–326, 1994.
- [111] H.-J. Werner and P. J. Knowles. An efficient internally contracted multiconfiguration reference configuration interaction method. *J. Chem. Phys.*, 89:5803–5814, 1988.
- [112] P. J. Knowles and H.-J. Werner. An efficient method for the evaluation of coupling coefficients in configuration interaction calculations. *Chem. Phys. Lett.*, 145:514–522, 1988.
- [113] T. H. Dunning, Jr. Gaussian basis sets for use in correlated molecular calculations. I. The atoms boron through neon and hydrogen. *J. Chem. Phys.*, 90:1007–1023, 1989.
- [114] T. Archipov, M. Bauer, A. B. Ene, T. Kittel, A. Kromer, H. Bertagnolli, and E. Roduner. to be submitted.

- [115] N. Jardillier, E. A. Villagomez, G. Delahay, B. Coq, and D. Berthomieu. Probing CuI-exchanged zeolite with CO: DFT modeling and experiment. *J. Phys. Chem. B*, 110:16413–16421, 2006.
- [116] A. E. Reed, L. A. Curtiss, and F. Weinhold. Intermolecular interactions from a natural bond orbital, donor-acceptor viewpoint. *Chem. Rev.*, 88:899–926, 1988.
- [117] E. R. Cohen de Lara. Experimental and theoretical determination of vibrational frequency shifts of diatomic molecules adsorbed in NaA zeolite
Interaction potential and its derivatives with respect to the internal coordinate of H₂, D₂, N₂, O₂. *Mol. Phys.*, 66:479–492, 1989.
- [118] E. N. Gribov, D. Cocina, G. R. G. Spoto, S. Bordiga, and A. Zecchina. Vibrational and thermodynamic properties of Ar, N₂, O₂, H₂ and CO adsorbed and condensed into (H,Na)-Y zeolite cages as studied by variable temperature ir spectroscopy. *Phys. Chem. Chem. Phys.*, 8:1186–1196, 2006.
- [119] T. K. Das, M. Couture, Y. Ouellet, M. Guertin, and D. L. Rousseau. Simultaneous observation of the O–O and FeO₂ stretching modes in oxyhemoglobins. *Proc. Natl. Acad. Sci.*, 98:479–484, 2001.
- [120] J. Neugebauer and B. A. Hess. Fundamental vibrational frequencies of small polyatomic molecules from density-functional calculations and vibrational perturbation theory. *J. Chem. Phys.*, 118:7215–7225, 2003.
- [121] V. B. Kazansky, V. Yu. Borovkov, and L. M. Kustov. in *Proc. 6th Int. Congr. on Catalysis*. Dachema Verlag Chemie, 1984.
- [122] V. B. Kazansky, V. Yu. Borovkov, and H. G. Karge. in *Proc. 12th Int. Zeo. Conf.* 1998. edited by M. M. J. Treacy, B. K. Marcus, M. E. Bisher, J. B. Higgins.
- [123] K. Nakamoto. *Infrared and Raman Spectra of Inorganic and Coordination Compounds Part B: Applications in Coordination, Organometallic, and Bioinorganic Chemistry*. John Wiley & Sons Inc., New Jersey, 2009.
- [124] J. Plíva, J. W. C. Johns, and L. Goodman. Infrared bands of isotopic benzenes: ν_{13} and ν_{14} of ¹³C₆D₆. *J. Mol. Spectr.*, 148:427–435, 1991.
- [125] R. Kumashiro, Y. Kuroda, and M. Nagao. New analysis of oxidation state and coordination environment of copper ion-exchanged in ZSM-5 zeolite. *J. Phys. Chem. B*, 103:89–96, 1999.

- [126] C. Lamberti, G. T. Palomino, S. Bordiga, G. Berlier, F. D'Acapito, and A. Zecchina. Structure of homoleptic $\text{Cu}^I(\text{CO})_3$ cations in Cu^I -exchanged ZSM-5 zeolite: An X-ray absorption study. *Angew. Chem. Int. Ed.*, 39:2138–2141, 2000.
- [127] O. Bludský, M. Silhan, P. Nachtigall, T. Bucko, L. Benco, and J. Hafner. Theoretical investigation of CO interaction with copper sites in zeolites: Periodic DFT and hybrid quantum mechanical/interatomic potential function study. *J. Phys. Chem. B*, 109:9631–9638, 2005.
- [128] E. Broclawik, P. Kozyra, and J. Datka. Ir studies and DFT quantum chemical calculations concerning interaction of some organic molecules with Cu^+ sites in zeolites. *C. R. Chimie*, 8:491–508, 2005.
- [129] G. Hübner, G. Rauhut, H. Stoll, and E. Roduner. FTIR measurements and quantum chemical calculations of ethylene adsorbed on CuNaY. *Phys. Chem. Chem. Phys.*, 4:3112–3121, 2002.
- [130] G. Hübner, G. Rauhut, H. Stoll, and E. Roduner. Ethyne adsorbed on CuNaY zeolite: FTIR spectra and quantum chemical calculations. *J. Phys. Chem. B*, 107:8568–8573, 2003.
- [131] M. S. J. Dewar. empty. *Bull. Soc. Chim. Fr.*, 1951:18, 0000.
- [132] J. Chatt and L. A. Duncanson. 586. Olefin co-ordination compounds. Part III. Infra-red spectra and structure: attempted preparation of acetylene complexes. *J. Chem. Soc.*, pages 2939–2947, 1953.
- [133] O. Bludský, M. Silhan, D. Nachtigallová, and P. Nachtigall. Calculations of site-specific CO stretching frequencies for copper carbonyls with the “Near Spectroscopic Accuracy”: CO interaction with Cu^+ /MFI. *J. Phys. Chem. A*, 107:10381–10388, 2003.
- [134] E. Kukulska-Zajac, P. Kozyra, and J. Datka. The interaction of benzene with Cu^+ sites in zeolites: IR studies and DFT quantum chemical calculations. *Appl. Catal. A: General*, 307:46–50, 2006.
- [135] A. Tamási, Z. Kónya, L. Guzzi, and I. Kiricsi. Infrared spectroscopic study of benzene and chlorobenzene adsorption on Pt,Cu- and Pt, CoZSM-5 bimetallic zeolite catalysts. *Appl. Catal. A: General*, 563:435–438, 2001.

- [136] T. D. Jaeger, D. van Heijnsbergen, S. J. Klippenstein, G. von Helden, G. Meijer, and M. A. Duncan. Vibrational spectroscopy and density functional theory of transition-metal ion-benzene and dibenzene complexes in the gas phase. *J. Am. Chem. Soc.*, 126:10981–10991, 2004.
- [137] E. Cané, A. Miani, and A. Trombetti. The ν_6 , ν_7 , ν_8 and ν_{19} gas phase fundamental frequencies of $^{12}\text{C}_6\text{H}_6$. *Chem. Phys. Lett.*, 272:83–85, 1997.
- [138] M. Davidová, D. Nachtigallová, P. Nachtigall, and J. Sauer. Nature of the Cu^+ -NO bond in the gas phase and at different types of Cu^+ sites in zeolite catalysts. *J. Phys. Chem. B*, 108:13674–13682, 2004.
- [139] K. Koszinowski, D. Schröder, H. Schwarz, M. C. Holthausen, J. Sauer, H. Koizumi, and P. B. Armentrout. Bond dissociation energies and structures of CuNO^+ and $\text{Cu}(\text{NO})_2^{2+}$. *Inorg. Chem.*, 41:5882–5890, 2002.
- [140] B. L. Su and D. Barthomeuf. Adsorption sites for benzene in KL zeolite: An infrared study of molecular recognition. *Zeolites*, 15:470–474, 1995.
- [141] A. de Mallmann and D. Barthomeuf. Change in benzene adsorption with acidobasicity of (Cs, Na)X zeolites studied by i.r. spectroscopy. *Zeolites*, 8:292–301, 1988.
- [142] A. de Mallmann and D. Barthomeuf. Changes with dealumination of the state of benzene adsorbed on faujasites. *J. Chem. Soc., Chem. Commun.*, pages 476–477, 1986.
- [143] D. Barthomeuf. Acidity and basicity in zeolites. *Stud. Surf. Sci. Catal.*, 65:157–169, 1991.
- [144] E. Pidko and V. Kazansky. σ Type ethane adsorption complexes with Cu^+ ions in Cu(I)-ZSM-5 zeolite. Combined DRIFTS and DFT study. *Phys. Chem. Chem. Phys.*, 7:1939–1944, 2005.
- [145] H. Klein, H. Fuess, and G. Schrimpf. Mobility of aromatic molecules in zeolite NaY by molecular dynamics simulation. *J. Phys. Chem.*, 100:11101–11112, 1996.
- [146] B. Geil, O. Isfort, B. Boddenberg, D. E. Favre, B. F. Chmelka, and F. Fujara. Reorientational and translational dynamics of benzene in zeolite NaY as studied by one- and two-dimensional exchange spectroscopy and static-field-gradient nuclear magnetic resonance. *J. Chem. Phys.*, 116:2184–2193, 2002.

- [147] O. Isfort, B. Boddenberg, F. Fujara, and R. Grosse. Molecular dynamics of benzene in zeolite NaY studied by 2D deuteron NMR. *Chem. Phys. Lett.*, 288:71–76, 1998.
- [148] M. D. Kadgaonkar, M. W. Kasture, V. B. Kartha, R. Kumar, and N. M. Gupta. Influence of pore structure and framework Al sites on the state of benzene (C_6H_6 and C_6D_6) molecules entrapped in the zeolites of BEA type: In situ IR spectroscopy study. *J. Phys. Chem. C*, 111:9927–9935, 2007.
- [149] D. Berthomieu and G. Delahay. Recent advances in $Cu^{I/II}Y$: Experiments and modeling. *Catal. Rev*, 48:269–313, 2006.
- [150] J. Datka, E. Kukulska-Zajac, and W. Kobyzewa. IR studies of coadsorption of organic molecules and CO on Cu^+ cations in zeolites. *Catal. Today*, 114:169–173, 2006.
- [151] P. Kozyra and J. Datka. Co-adsorption NO and organic molecules on Cu^+ sites in zeolites: Quantum chemical DFT calculations. *J. Mol. Struct.: THEOCHEM*, 778:35–40, 2006.
- [152] S. Grimme. Accurate description of van der waals complexes by density functional theory including empirical corrections. *J. Comput. Chem.*, 25:1463–1473, 2004.
- [153] S. Grimme. Semiempirical GGA-type density functional constructed with a long-range dispersion correction. *J. Comput. Chem.*, 27:1787–1799, 2006.
- [154] Y. Moro-oka and M. Akita. Bio-inorganic approach to hydrocarbon oxidation. *Catal. Today*, 41:327–338, 1998.
- [155] D. Schröder and H. Schwarz. C–C and C–H bond activation by bare transition-metal oxide cations in the gas phase. *Angew. Chem. Int. Ed. Engl.*, 34:1973–1995, 1995.
- [156] Y. Shiota, K. Suzuki, and K. Yoshizawa. Mechanism for the direct oxidation of benzene to phenol by FeO^+ . *Organometallics*, 24:3532–3538, 2005.
- [157] K. Kwapien and E. Broclawik. Interaction of FeO^+ cation with benzene, aniline, and 3-methylaniline: DFT study of oxygen insertion mechanism. *Int. J. Quantum Chem.*, 108:2016–2022, 2008.

- [158] S. P. de Visser and S. Shaik. A proton-shuttle mechanism mediated by the porphyrin in benzene hydroxylation by cytochrome P450 enzymes. *J. Am. Chem. Soc.*, 125:7413–7424, 2003.
- [159] R. L. Redington, W. B. Olson, and P. C. Cross. Studies of hydrogen peroxide: The infrared spectrum and the internal rotation problem. *J. Chem. Phys.*, 36: 1311–1326, 1962.
- [160] H.-J. Werner, P. J. Knowles, R. Lindh, F. R. Manby, M. Schütz, P. Celani, T. Korona, A. Mitrushenkov, G. Rauhut, T. B. Adler, R. D. Amos, A. Bernhardsson, A. Berning, D. L. Cooper, M. J. O. Deegan, A. J. Dobbyn, F. Eckert, E. Goll, C. Hampel, G. Hetzer, T. Hrenar, G. Knizia, C. Köppl, Y. Liu, A. W. Lloyd, R. A. Mata, A. J. May, S. J. McNicholas, W. Meyer, M. E. Mura, A. Nicklass, P. Palmieri, K. Pflüger, R. Pitzer, M. Reiher, U. Schumann, H. Stoll, A. J. Stone, R. Tarroni, T. Thorsteinsson, M. Wang, and A. Wolf. Molpro, version 2008.3, a package of ab initio programs, 2008. see <http://www.molpro.net>.
- [161] R. A. Mata and H.-J. Werner. Calculation of smooth potential energy surfaces using local electron correlation methods. *J. Chem. Phys.*, 125:184110–184118, 2006.
- [162] R. A. Mata and H.-J. Werner. Toward accurate barriers for enzymatic reactions: QM/MM case study on p-hydroxybenzoate hydroxylase. *J. Chem. Phys.*, 128: 025104–025111, 2008.
- [163] R. C. Baetzold. Atomistic study of polarons in $\text{YBa}_2\text{Cu}_3\text{O}_7$. *J. Am. Ceram. Soc.*, 73:3185–3188, 1990.